Digital Holographic Imaging of Aquatic Species

by

José Antonio Domínguez-Caballero

B.S., Instituto Tecnólogico de Morelia (2002)

Submitted to the Department of Mechanical Engineering
in partial fulfillment of the requirements for the degree of

Master of Science in Mechanical Engineering

at the

MASSACHUSETTS INSTITUTE OF TECHNOLOGY

February 2006

Signature of Author .....
Department of Mechanical Engineering
15 January 2006

Certified by .....
George Barbastathis
Associate Professor of Mechanical Engineering
Thesis Supervisor

Accepted by .....
Lallit Anand
Chairman, Department Committee on Graduate Students

Digital Holographic Imaging of Aquatic Species

by

José Antonio Domínguez-Caballero

Submitted to the Department of Mechanical Engineering
on 15 January 2006, in partial fulfillment of the
requirements for the degree of
Master of Science in Mechanical Engineering

Abstract

The aim of this thesis is to design, develop and implement a digital holographic imaging (DHI) system, capable of capturing three-dimensional (3D) images of aquatic species. The images produced by this system are used in a non-intrusive manner to characterize the abundance, morphology and 3D location of the aquatic species. The DHI system operates by recording the hologram produced by the interference between a reference wave and the wave scatter by a coherently illuminated object with a charge-couple-device (CCD). The recorded hologram contains information about the amplitude and phase of the optical field as modified by the object. This optical field is retrieved by numerical algorithms, which enable the reconstruction of the field at different distances relative to the detector from a single hologram. The recording of the holograms with the CCD allows the implementation of image post-processing techniques intended to enhance the reconstructed images. A description of the optimization of the reconstruction by means of an auto-scan algorithm and the reconstruction of large holograms are discussed. It is found that the in-line single-beam experimental set-up is the most suitable configuration for underwater imaging of aquatic species. This is experimentally verified by imaging brine shrimp and copepods under various conditions. Small, sub-10μm features of the objects were successfully resolved. It is also found that by using configurations with a spherical reference wave, resolutions comparable to those obtained by a conventional optical microscope can be achieved in a "lens-free" approach with larger working distances.

Thesis Supervisor: George Barbastathis
Title: Associate Professor of Mechanical Engineering

Acknowledgments

I would like to thank my advisor, Professor George Barbastathis, for his guidance and support as well as for giving me the fantastic opportunity to work in his group. I have learned a lot from him in the past couple of years and I look forward to the years to come. Thank you for being such a great advisor.

I am also very grateful for the support, advice and energy that my co-advisors, Professor Jerome H. Milgram and Professor Cabell Davis, have invested in this project.

I would like to thank all the members of the 3D Optical Systems Group not only for their help and advice, but also for their support and friendship. I have had a great time working with you guys.

Thanks to Anthony Nichol for helping me manufacture the high-pass Fourier filter that I used in some experiments.

I am very thankful to Nick Loomis for helping me with the set-up of some experiments. Welcome to the amazing world of underwater digital holography!

Many thanks to Rebecca Moon for proof-reading this thesis. Thank you also for all your love and unconditional support.

Finally, I would like to thank my parents, Jose Antonio and Elsa, and my sister and brothers, Susana, Carlos and Javier, for all their love and support. It is this love that feeds me with energy to become a better person.

Contents

List of Tables

List of Figures

Chapter 1

Introduction

1.1 Overview

In Chapter 1, the importance of studying aquatic ecosystems and the motivation to develop an instrument that facilitates the analysis and characterization of aquatic species is discussed. A brief overview of current technologies used to study plankton is also presented.

In Chapter 2, the concept of holographic imaging is described through the analysis of conventional optical holography. A more detailed examination of the foundation of digital holographic imaging (DHI) systems is explored through several recording set-ups and numerical reconstruction algorithms.

In Chapter 3, an analysis of the resolution of the DHI system and the sampling requirements is conducted.

In Chapter 4, design considerations required to develop the DHI system are addressed and experimental results from imaging brine shrimp and copepods are presented.

In Chapter 5, image post-processing algorithms designed to optimize, enhance and analyze the images obtained from the DHI system are described.

Chapter 6 provides a conclusion for the effectiveness of a DHI system to characterize aquatic species based on experiments conducted with plankton. This chapter also suggests areas to further improve on the design, development and implementation of this imaging system and outlines future directions for this research.

1.2 Imaging of Aquatic Species

The critical need to understand the dynamics of aquatic ecosystems has led to the development of tools to help scientists collect high-resolution spatio-temporal data on species-specific population structures. Such data are critical for accurate modeling of biological populations towards a potential predictive capability of ecosystem fluctuations. In the case of aquatic (marine and freshwater) ecology, the implications of such fluctuations are reflected in issues such as: shoreline over-development; sewage and toxic pollution; over-fishing; and global warming. An ability to predict these issues would help governments and non-governmental organizations assess the impact of humans on the quality of their environment.

A significant part of the research into aquatic ecology has been canalized to the analysis of planktonic populations. In the next subsections the importance of aquatic ecosystems and the roll of plankton will be briefly described in order to provide a basic understanding of the motivations in developing research in this field.

1.2.1 Importance of Aquatic Ecosystems

The earth is comprised of seventy-five percent water, of which ninety-eight percent is in oceans - where half of the earth's photosynthesis occurs. A body of water principally constituted by multiple species interacting with each other and their chemical and physical environment over multiple time-space scales is considered to be an aquatic ecosystem.

From phytoplankton to small fish and whales, the aquatic food chain constitutes a very complex system that still remains largely unexplored.

In aquatic ecosystems, plankton represents a fundamental link and constitutes the beginning of the food chain. Plankton is the aggregate community of swimming organisms that inhabit the water of oceans, seas, and bodies of freshwater. They are often used as indicators of environmental and aquatic health, due to their high sensitivity to changes in the environment, as well as for their short life span. Plankton can be divided into three broad functional groups:

- **Phytoplankton**. These are algae that live near the water surface where there is enough sunlight to produce the photosynthesis required to survive. Phytoplankton are also called "producers" as they produce their own food.
- **Zooplankton**. These are small protozoa, crustaceans and animals that feed on other plankton. Eggs and larvae of larger animals such as fish, crustaceans and annelids are also included in this category.
- **Bacterioplankton**. These are bacteria and archaea that are crucial to the absorption of nutrients dissolved in the water.

Phytoplankton are great indicators of high nutrient conditions, due to their propensity to multiply rapidly if they are in adequate conditions. They also alter the biogeochemical cycling nutrients and carbon in the ocean. Similarly, zooplankton are useful indicators for the health of future fisheries, as they are the food source for many organisms of higher trophic levels.

Copepods are small aquatic animals that belong to the zooplankton subclass and constitute the largest and most diversified group of crustaceans in the world. In addition, copepods include over 14,000 species, 2,300 genera and 210 families making them the dominant form of marine plankton and a fundamental part of the trophodynamics of the

ocean. From sponges to vertebrates, copepods can virtually parasitize or be the intermediate host of all animal groups, including mammalians and humans. In both marine and freshwater, copepods that parasitize fish and gill are a serious pest of commercial importance. On the other hand, copepods also have the potential to act as control mechanisms for malaria, by consuming mosquito larvae. Harmful Algal Blooms (HABs) can exert a dominant (and harmful) influence on pelagic ecosystems via the consumption of nutrients, the production of toxins, and the creation of anoxic conditions [1].

The need to study planktonic populations and other forms of aquatic organisms has prompted a generation of sampling tools and techniques that provide some of the information required to understand the mechanisms of aquatic ecosystems. In the following subsection some of these sampling systems are briefly described.

1.2.2 Sampling Systems of Aquatic Species

Several sampling methods have been developed in order to better understand aquatic ecosystems. These sampling techniques can be broadly categorized into: direct sampling, acoustic sensing and optical imaging. The developed systems range from commercially available instruments, which are mass-produced, to one-of-a-kind instruments, produced for particular circumstances. Despite recent developments, most systems are still inadequate for providing the high-resolution data on species abundances, morphology and life-stage needed to predict information including population sizes, species and habits. Acoustic techniques offer the possibility of longer range imaging, but they suffer from a lack of specificity and knowledge of the multidimensional features of the scattering functions. Optical methods offer a very high resolution and characterization of the acquired data, which is usually presented in a very convenient form for humans to analyze. However, optical techniques usually have a very limited sampling range, and if operated with high-powered light they disturb the animals being sampled, making it difficult to capture their natural behavior.

Many of the systems made to characterize aquatic species have been devoted to the study of micronekton, nekton, and in particular the study of plankton. Efforts to study the relationship of HABs to plankton were initially reported in [2] and [3]. These studies have also helped to understand the relationship between phytoplankton and zooplankton.

One of the techniques used often to analyze plankton is to capture small samples from the ocean with the help of "plankton nets" for a later characterization in the laboratory. Plankton nets are made of a very fine nylon mesh supported by rings forming a truncated cone (similar to a wind sock) with a bottle attached to the narrower side. The net is towed through the ocean letting the water pass through the mesh but trapping small particles that are concentrated inside the bottle. An example of a commercial plankton net is shown in Figure 1-1 [4].

Figure 1-1: Plankton net.

This direct sampling technique produces the best morphological characterization of the species by imaging them in a controlled environment with high-magnification microscopes. However, plankton towing is highly intrusive and does not allow the behavior of the sampled organisms to be monitored. Information about the abundance as function

of location cannot be retrieved. An example of an image taken with a microscope from copepods collected using plankton nets is shown in Figure 1-2 [5].

Figure 1-2: Copepod Eurytemora affinis. Female of 1mm in length, commonly found in estuarine waters throughout the northern hemisphere.

Acoustics techniques have proliferated considerably in recent years due to the ease of creating, recording and processing sound waves. Several reviews relating to contemporary instruments and sound scatter by organisms in the sea involving zooplankton have been written [6], [7]. Books describing the use of acoustics for fisheries assessments [8] and zooplankton acoustics [9] are also available.

The general set-up for acoustical sensing is shown in Figure 1-3. Acoustic sensors consist of a set of electronics for both transmitting and receiving the sonar signal. The transmitting electronics are connected to transducers that transform the electrical signal into a sound wave. The receiving electronics are connected to transducers that transform the pressure wave into an electrical signal that is then recorded and analyzed. For a more detailed explanation of the principles of sonar systems refer to [10] and [11].

There are two common methods used for sampling aquatic species: echo integration and echo counting. With echo integration the biomass is estimated by recording the backscattering of a sampled volume using either single frequency or multiple frequency

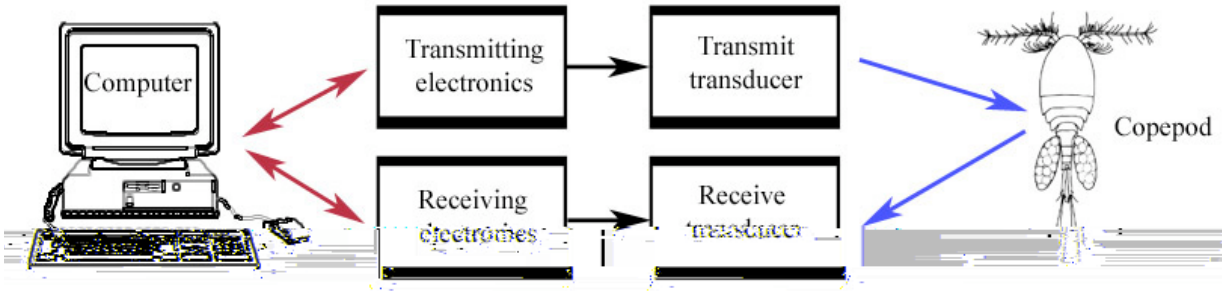

Figure 1-3: Acoustical sensing set-up for recording zooplankton.

inversions. With echo counting the number of organisms can be inferred from the multiplicity of traces after recording the reflection of a single animal. When densities become high, echo counting presents problems due to multiple reflections that saturate the system and make individual traces indiscernible. More precise identification of species may be accompanied with net tows or optical imaging methods.

One way to characterize acoustic sensing systems is to consider the number of beams and number of frequencies in which they operate. Table 1.1 contains a list of sensors categorized in this form [1]. Although many acoustical systems to monitor fish are available today, the number of systems designed to monitor zooplankton are very limited.

Table 1.1: Categorization of acoustic systems.

	Split Beam	**Dual Beam**	**Single Beam**	**Multi Beam**
Single Frequency	Commercial	Commercial	Commercial	Commercial FTV: Jaffe [19]
Multiple Frequency	Wiebe[12], [13] and Demer [14]	Wiebe [15]	Maps/Taps: Holliday [16] and Griffiths [17]	Not known
Wide band System	Not known	Not known	Commercial (SciFish) Foote [18]	Not known

The most basic type of acoustic sensor systems is the single frequency single beam

type. Many economical consumer oriented sensors for detecting fish are available. Unfortunately the lack of proper calibration procedures makes them unsuitable for scientific use as no quantitative biomass information can be retrieved. For this reason, the Acoustic Doppler Current Profiler (ADCP) is a very popular system in the oceanographic community. This system works by sending four beams of sound into the water for a later measure of the Doppler shift and hence, some estimate of the vector-valued current (appealing to estimate biomass) can be found. Studies of zooplankton biomass using this device were reported in [20]. Difficulties in achieving quantitative information made the ADCP a more suitable system for qualitative estimations of animal abundance. Figure 1-4 shows a photo of an ADCP [21].

Figure 1-4: Photo of an Acoustic Doppler Current Profiler.

Both dual beam and split beam systems have similar goals where the position of the animal must be known in order to estimate the incident sound intensity to discern the wave. These systems produce good quantitative measurements but they have to be calibrated routinely. In the dual beam system, the received and transmitted beam patterns are cylindrically symmetric and the ratio between the intensity of the received wave per object is used to locate the target and thus the target strength. In the split beam system, the disk is split into four quadrants sensitive to sound and the time delay between quadrants is used to distinguish the direction of the sound source. A comparison of the

performance of both systems can be found at [22], where split beam systems were found to be more robust in estimating animal positions. Current companies that manufacture bioacustic systems include Simrad, Reson A/S, Biosonics and Hydroacoustic Technology Inc.

Due to the low acoustic reflectivity of zooplankton, multi-beam systems provide higher power and larger field of view. The FishTV system [19] is one multi-beam system used to map the behavior of euphausiids and copepods.

The multi-frequency system is another type of acoustic sensor. A series of instruments in one frequency regime (400 kHz – 3Mhz) by Holliday [23] have been used in the past several decades to estimate the size and type of animals ranging from 200μm–1cm in size. The deployment of the latest version of the system, TAPS^{TM} is described in [16] where according to the authors, the best results were obtained at ranges up to 20 or 30m. Another example of a multi-frequency system is the Biomapper [12]. BIOMAPPER II is a newer version of this system fabricated by the Woods Hole group [24]. Figure 1-5 shows a sketch of the BIOMAPPER II [25]. Other examples of multi-frequency systems are found in [18] and [17].

The broadband system is the final type of acoustical sensors. An example of this sensor used in a laboratory can be found in [26]. A commercial broadband system is currently available from Scientific Fishery Systems Inc. [27].

The third type of sampling systems of aquatic species is the optical imaging systems. These systems have performed reasonably well for observing zooplankton and, in some situations; information regarding animal identification and abundance can be retrieved. One disadvantage of these systems is that they tend to sample smaller volumes than acoustic systems. This is sometimes compensated by the use of fast frame rates and rapid surveys.

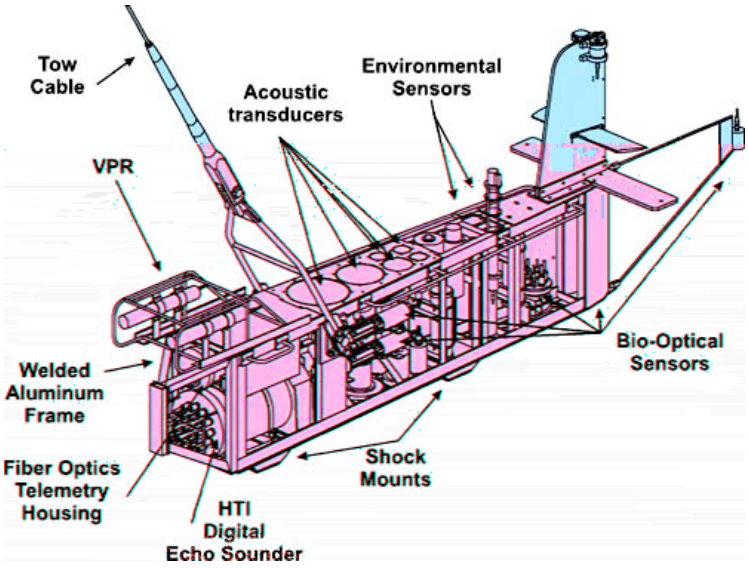

Figure 1-5: Multi-frequency acoustic system. BIOMAPPER II.

In the realm of optical imaging systems the Video Plankton Recorder (VPR) plays an important role, [28], [29]. The VPR is a video-microscope system that uses forward scattering light to image organisms that are nearly transparent ranging from 0.2 – 20mm in size. Multiple cameras synchronized at 60 fields per second (fps) to a red-filtered 80Watts xenon strobe (pulse duration = 1μ sec) image the same volume of water in order to provide information on different scales. The sampled volume ranges from about 1 ml to 1 l, depending on the settings of the magnification optics in each video camera. An automatic image classification system was developed, based on neural network approaches, to help reduce the vast quantity of data to a description of the patterns of concentration [30]. An example of a deployment of this device in the George's Bank region can be found in [31]. Figure 1-6 shows the schema and photo of the VPR system. Images acquired using this device are shown in Figure 1-7.

The Underwater Video Profiler System is an alternative imaging device capable of sampling organisms down to 100μm in size [32]. It consists of a Hi-8 video camera, a

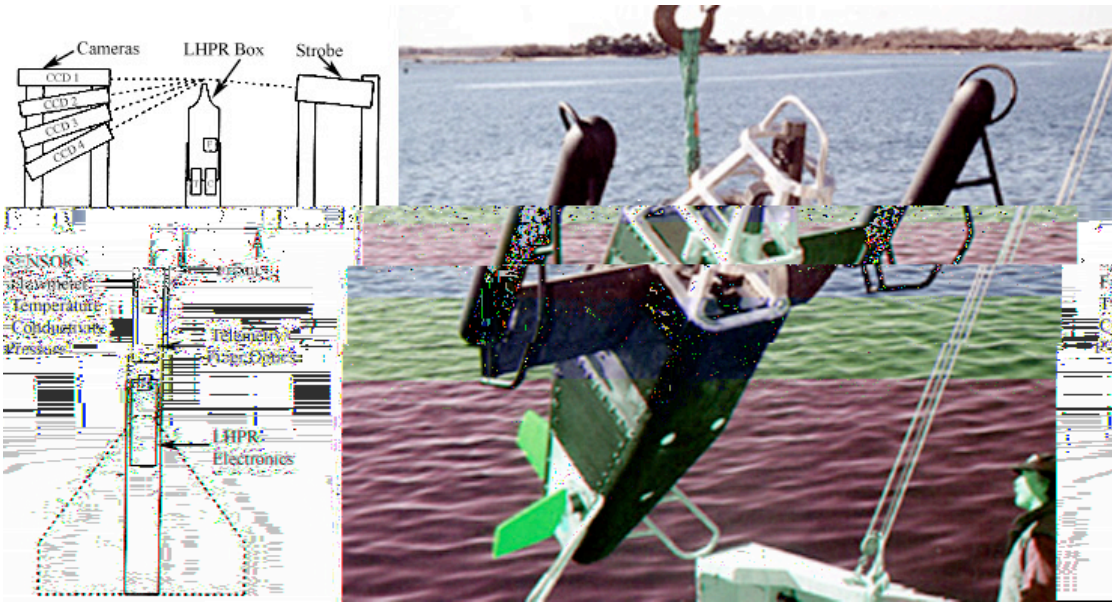

Figure 1-6: Video Plankton Recorder. To the left: the schema of the VPR showing the layout of mayor components. To the right: the VPR tested at the Woods Hole Oceanographic Institute. (Photo by Woods Hole Oceanographic Institute)

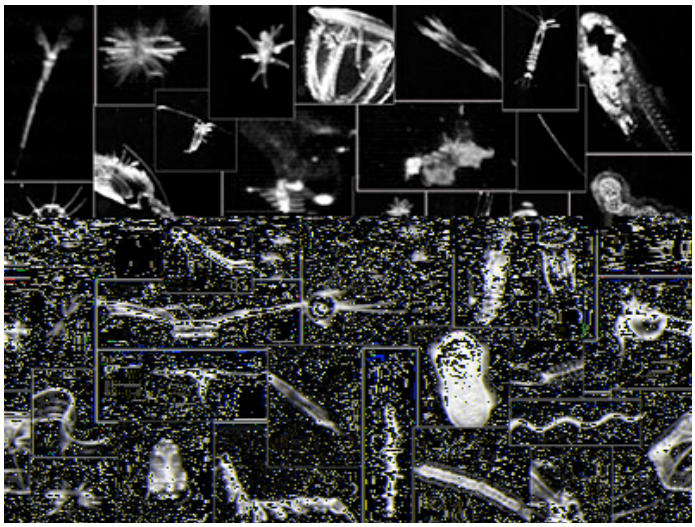

Figure 1-7: Images of plankton taken by the VPR during transatlantic survey in August 2003. (Photo by Woods Hole Oceanographic Institute)

controlling and logging unit, batteries and several light systems. The lighting system can either consist of four spotlights to illuminate a volume of 70 l of water, or be a collimated light field in front of the camera that produces an illumination sheet used for particle distributions. Results of some deployments of this system can be found in [33], [34] and [35]. Figure 1-8 shows a photo of an Underwater Video Profiler System [36].

Figure 1-8: Underwater Video Profiler System.

The ZooVis System is an alternative optical imaging system design to collect quantitative images of zooplankton to depths of 250m [37]. The system is based on a high-resolution camera pointing down into a sheet of light produced by a strobe. The strobe and the camera are synchronized to take images with sufficient quality to differentiate between species. The ZooVis System is shown in Figure 1-9 [38].

The 3D Zooplankton Observatory is a system designed to obtain information about three-dimensional trajectories of zooplankton using Schlieren imaging in conjunction with multiple cameras to obtain orthogonal projections of the target [39]. The system images 1 l of water and permits viewing aquatic organisms ranging from phytoplankton to fish.

An alternative device to image organisms under water is the Flow Cam system by

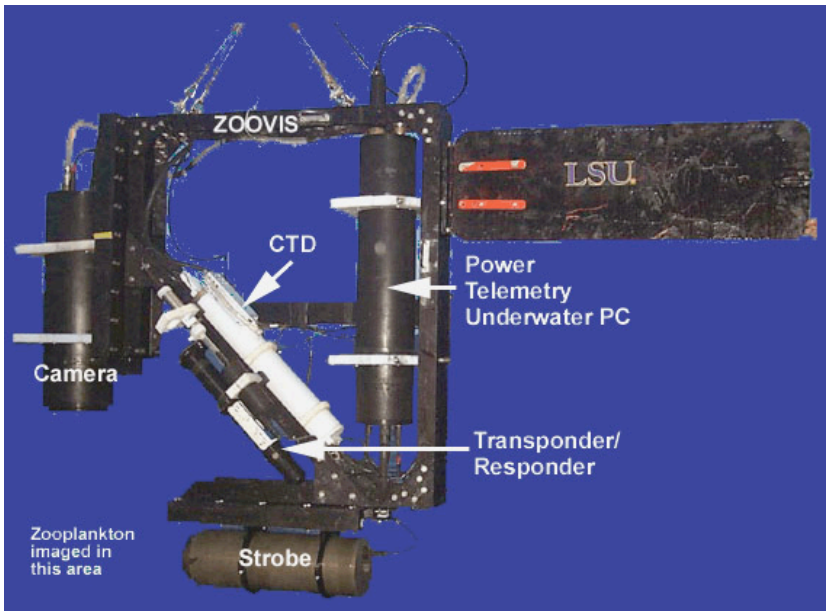

Figure 1-9: The ZooVis System.

Fluid Imaging Technologies, (Boothbay, ME). The Flow Cam system works by pumping samples through a small illuminated volume that has high-resolution optics incident upon it. The system is optimized due to the small size of the volume of interrogation. However, this limits the system to be used in situ.

FIDO-Φ is an imaging system design to map the location and biomass of phytoplankton by recording the scattered or fluorescent light from a volume of approximately half a liter. In a typical application, the volume of water is illuminated with a sheet of light allowing imaging of an area of 25cm x 25cm at a range of 80cm [40], [41].

An optical imaging system of specific interest to this thesis is underwater holography. In the standard form, holographic imaging uses a photosensitive film to capture the interference pattern between a reference wave and the wave scattered by an illuminated object. In-line and off-axis are the two main configurations that can be encountered. In in-line configuration, both the object and reference wave are collinear and parallel to the optical axis of the recording medium. In the off-axis configuration, the two beams are

separated by a small angle producing a different effect during the reconstruction of the target. Information about the amplitude and phase of the object field can be retrieved by illuminating the recorded film with a beam similar to the reference beam used in the recording step. The details of this method will be explained in the next chapter.

Holographic imaging of underwater organisms is a particularly effective technique as it provides a good characterization of the morphology of the animals and recovers their three-dimensional location. By capturing several consecutive holograms, data regarding biomass and flow type can be retrieved. A good review of the principles and practice of holographic recording of plankton can be found in [42].

It is important to note that there are other systems available to count plankton including the optical plankton counter (OPC) and the laser optical plankton counter (LOPC). As these systems are not considered "imaging systems" per se, they have not been discussed in this section. The main reason they are not considered imaging systems is that they do not produce representations (or images) of physical objects. These systems are design to count the number of objects of interest per unit volume.

Hybrid systems (combining acoustics and optics) have been developed in order to compensate the limitations that occur with the individual systems. The lower frequency acoustical techniques for sensing zooplankton are advantageous in mapping moderate distances (10's-100's of meters) and the optical systems are more effective for animal identification. Examples of in situ hybrid systems are documented in [43] and [44].

1.3 Motivation for Digital Holographic Imaging of Aquatic Species

In the previous section, the importance of studying aquatic ecosystems and a survey of the current sampling methods for plankton were discussed. None of these techniques rep-

resents an optimum solution to the problem of underwater species characterization. In order to develop a predictive capability in environmental science, it is imperative to acquire data relating to biomass, behavior, morphology, and the life stage of the organisms that inhabit a certain aquatic ecosystem. Although acoustic sampling methods generally provide high-resolution backscatter data for estimating abundance concentrations, they do not provide detailed information regarding size and taxonomical composition of plankton. Optical techniques have been shown to produce better results in the level of species identification, but tend to sample smaller volumes of water and therefore require faster surveys to compensate. In addition, most devices are very bulky and, due to their short sampling range, disturb the animals that are sensitive to hydrodynamic disturbances. This invasiveness affects mapping the true behavior of the organism under study. Optical imaging systems that work with high-powered light, such as the Video Plankton Recorder (VPR), produce an additional disturbance to the natural dynamics of plankton.

Digital Holographic Imaging (DHI) is a technology promising to solve the majority of the problems identified. With DHI, the morphology of the sampled objects can be retrieved with sufficient quality to estimate the size, life stage and correspondent species. In addition, the three-dimensional position relative to the imaging sensor can be computed from a single captured image (single hologram). In the basic configuration, DHI is a lens-free technique that is capable of sampling large volumes from a single hologram by means of post-processing digital scans, allowing estimates of the biomass concentrations. The highly sampled range provided by this method, assuming that the water is sufficiently clear, allows a non-intrusive system to map the natural behavior of the animals being studied. By capturing consecutive holograms along the path of an underwater vehicle it is possible to estimate trajectories and swimming velocities of plankton.

DHI records the hologram in a CCD that usually requires low levels of coherent illumination. No film is used; therefore, no chemical post-processing is required to retrieve

the recorded optical field. As the image is already available in digital form, several image post-processing algorithms can be applied to reconstruct and enhance the quality of the image. Automatic plankton categorization algorithms can be implemented to help reduce the amount of computation. DHI systems for aquatic species can be built in a very compact form allowing flexibility of manipulation and a reduction of the hydrodynamic disturbances that affect plankton. In the past few years, technologies such as CCD imaging sensors, computers and pulsed diode lasers have been showing technological progress that are further favorable for practical underwater DHI.

The goal of this thesis is to describe the characterization, design and implementation of a digital holographic imaging system for aquatic species. This imaging system is part of a larger project, with the ultimate goal of developing a system capable of sampling all aquatic regions on earth, including the full depth of the ocean (11,000m). An Autonomous Underwater Vehicle (AUV) will carry the DHI system. In order to obtain a better characterization of the aquatic ecosystem, the AUV will also be equipped with additional sensors. Multiple AUVs working simultaneously in a given region would provide the high-resolution species-specific abundance data needed for accurate environmental modeling, assessment, and prediction.

In the next chapter, the basic principles and formulations of digital holographic imaging will be discussed.

Chapter 2

Digital Holographic Imaging

2.1 Conventional Optical Holography

In 1948 Dennis Gabor invented optical holography. This invention, for which he won the Nobel Prize for Physics in 1971, was a result of an "exercise in serendipity", as Gabor explains in his autobiography. Optical holography was initially presented in the context of electron microscopy as a method to resolve the problem introduced by the spherical aberrations of electron lenses that set the limit in the resolving power [45]. Two detailed papers, [46], [47], followed his pioneering work, which explored presenting holography as a method for recording and reconstructing the amplitude and phase of a wave field. He invented the world "holography" from the Greek words "holos" meaning "whole" and "graphein" meaning "to write". Holography only attracted mild interest until the 1960s, when the concept became popular, improved predominantly by the invention of the laser.

A hologram is a recorded interference pattern formed by combining a field scattered by a coherently illuminated object, with a field from background illumination (termed a reference wave,) which must be mutually coherent with the object-scattered field. In the conventional form, the interference pattern is recorded on a photosensitive film that is chemically developed later. The information about the 3D wave field scattered by the

object is encoded into a set of fringe

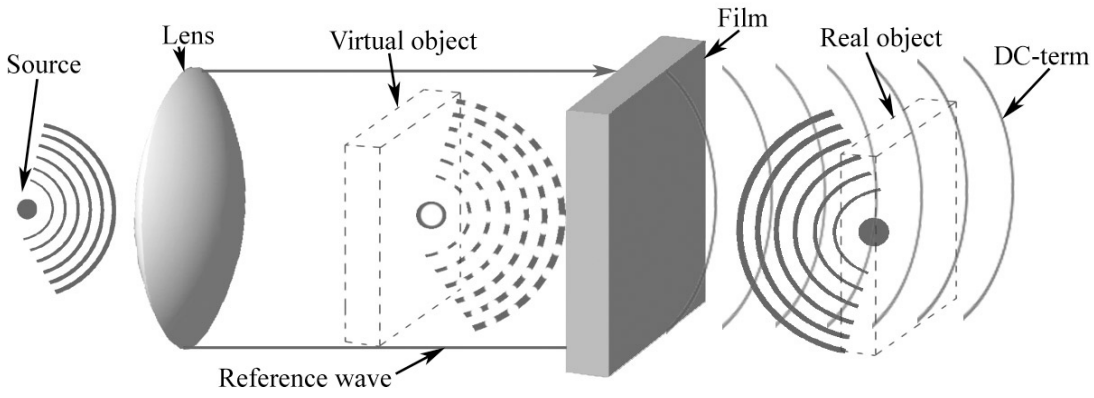

Figure 2-2: In-line reconstruction setup for conventional optical holography.

methods have been developed to overcome these limitations including the earlier work by Gabor [48] and the more recent phase-shifting techniques [49].

Leith and Upatnieks made significant advancements on Gabor's technique by inventing off-axis holography [50], [51]. Whilst conducting research at the University of Michigan's Radar Laboratory, they observed the similarity between Gabor's lens-less imaging system and the synthetic-aperture-radar problem. In off-axis holography, the interference pattern is recorded with a reference wave tilted by a small angle respective to the optical axis as shown in Figure 2-3. The small angular difference is equivalent to the use of heterodyning in radar, which was Leith and Upatnieks' inspiration. The main advantage of off-axis holography is that the DC term and the real and virtual images are spatially separated during the reconstruction. However, the high-frequency content of the hologram sets a limit in the type of recording film required in the experiment. Figure 2-4 shows the off-axis reconstruction setup.

As noted earlier, most recordings performed in optical holography are made on a photographic film or plate. The film used to record the interference pattern is assumed to provide a linear mapping of intensity incident during the detection process into amplitude

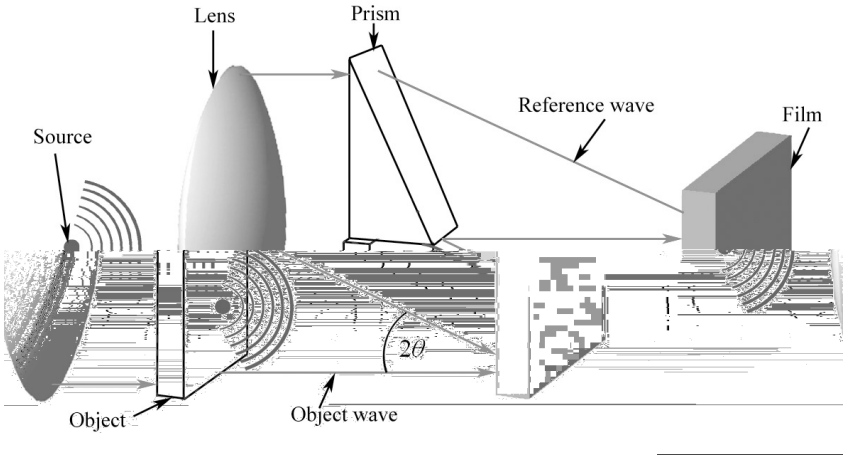

Figure 2-3: Off-axis recording configuration for conventional optical holography.

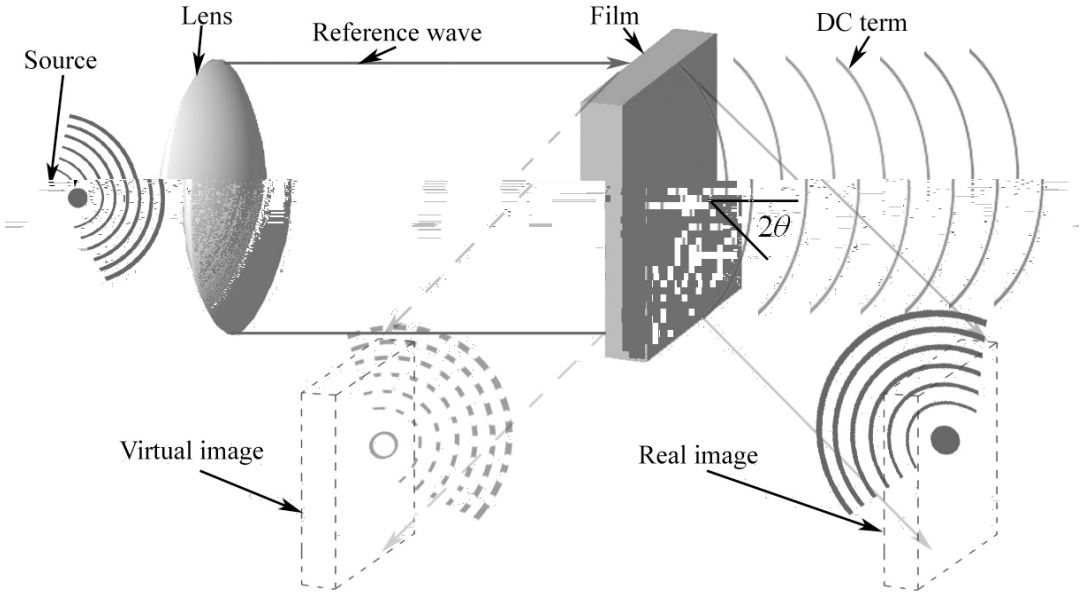

Figure 2-4: Off-axis reconstruction configuration for conventional optical holography.

transmitted by or reflected from the film during the reconstruction process [52]. Several other materials suitable for holography also exist, including photorefractive materials, dichromated gelatin and photopolymers.

During the same period that Leith and Upatnieks were developing off-axis holography, Y.N. Denisyuk, a scientist from what was then the Soviet Union, invented the thick reflection hologram. This hologram was greatly influenced by the work of Gabor and G. Lippmann [53], a French physicist. With reflection holograms, there is only one illumination beam working as a reference and illuminates the object through the holographic plate.

Holograms are sometimes also classified by the diffraction or imaging conditions that exist between the object and the recording medium. The first classification is the Fresnel type. A hologram is considered to be of this type if the recording plane lies within the region of Fresnel diffraction of the illuminated object. As expected, the second class is the Fraunhofer type. With this type of hologram, the transformation from the object to the recording plane is better described by the Fraunhofer diffraction equation. A hologram is referred to as an image hologram if the film is located in the image plane of the optical system. In the case of Fourier holograms, the recording plane resides in the Fourier plane of the object amplitude transmittance. Finally, with the lens-less Fourier transform hologram, the reference wave comes to focus in the object plane and then diverges to the recording plane. Similarly, the object wave propagates, without crossing any optical elements, to the recording plane.

Powell, Stetson et al developed Holographic Interferometry (HI) in the 1960s [54], [55]. HI is an important branch of holography capable of mapping displacements from rough surfaces with an accuracy of a fraction of a micrometer. With HI, it is also possible to compare interferograms produced by wave fronts recorded at different times.

Computer Generated Holography (CGH) was made possible with the development of computers, where artificial holograms were synthesized by numerical methods [56], [57],

[58]. The computer-generated holograms were later replayed using conventional optical techniques.

Similar to CGH, computers have been applied in the numerical reconstruction of holograms [59], [60]. With this technique, the field is optically enlarged and then sampled from Fourier and in-line holograms recorded in the conventional form used in optical hologrammetry. In the 1980s, Onural and Scott improved the reconstruction algorithm and applied this technique for particle measurements [61], [62], [63], [64]. Their improved algorithm is equivalent to a high order approximation that suppresses the effect of the twin-image in the reconstructed field. The development of the numerical reconstruction techniques lead the way to what it was later termed "Digital Holography".

Although not discussed in this thesis, other branches of holography include: holographic stereograms [65], [66]; rainbow holograms [67]; multiplex holograms [68], [69]; embossed holograms; thick holograms; and volume holograms [70].

A noteworthy limitation of optical holography is its reliance on the coherence length of the illuminating source. This is sometimes compensated by using high-quality lasers and by trying to match the propagation distance of the reference and object waves. In addition, clean and sharp fringes are required; therefore high stability is needed during exposure. If the power used to record the hologram increases, the required exposure time decreases, alleviating part of the stability constraint. High-resolution film is also required in order to capture the high-frequency content of the interference pattern, especially in off-axis holography. For example, a common photographic plate used in optical holography is the Kodak Spectroscopic Plate Type 649F, which has 2000 lines-pairs (cycles)/mm. In addition, the film has to be used in the linear region of the transmittance versus exposure curve [52], which is not always practically possible. The low dynamic range of the recording medium is another parameter that affects the quality of the reconstructions.

2.2 Digital Holographic Imaging: Basics

As discussed in the previous chapter, conventional holography provides a convenient way to store the 3D optical field of a sampled object. However, recording a hologram in a photographic medium requires developing the film prior to reconstruction. A single hologram contains an extremely large amount of information and typically takes several days to reconstruct an object scene from one hologram using optical replay and high resolution digitizing systems. This makes the process time-consuming, unstable and inflexible [71]. In addition, aberrations produced by the optical elements used to replay the hologram may disturb the quality of the reconstructions. Digital holographic imaging (DHI) offers a possibility to overcome these limitations.

In DHI, the hologram is recorded in a charge-coupled device (CCD) and the object is reconstructed using numerical methods. Direct recording of the hologram with the CCD avoids the intermediate steps of developing and digitizing the photographic film and no scratched or faded negatives are produced. In addition, CCDs have a higher dynamic range than standard films. The dynamic range is defined as the ratio between the maximum and minimum levels of brightness detected by the recording medium. This is usually defined over the region of linear response. The typical dynamic range of a photographic film is less than 1,000 (brightness range of less than 7.5^m) [72]. The typical dynamic range of a CCD is approximately 100,000 to 500,000 with the usable range in accurate brightness determination of up to 14.5^m. The CCD's quantum efficiency (sensitivity of detection) is approximately 35 times better than that of a conventional untreated film. CCDs do not suffer from reciprocity failure, which is the gradual loss of sensitivity as the exposure time increases. In addition, CCDs below saturation have a linear response to light and a spectral range (approximately 400nm to 1,100nm) much wider than that of ordinary film.

2.2.1 Wavefront Recording

Similar to conventional optical holography, DHI records the interference pattern produced by the superposition of a reference wave and the wave scattered by a mutually coherently illuminated object. The recorded intensity distribution (interference pattern) is called a "hologram" and has the property of encoding the information about the phase and amplitude of a 3D optical field as a set of interference fringes. The fringe contrast is function of the amplitudes of the object and reference waves and the coherence length of the illuminating source.

The intensity recorded at the hologram plane is given by

$$\begin{aligned} I(x_h, y_h) &= |r(x_h, y_h) + o(x_h, y_h)|^2 \\ &= |r(x_h, y_h)|^2 + |o(x_h, y_h)|^2 \\ &\quad + r(x_h, y_h)o^*(x_h, y_h) + r^*(x_h, y_h)o(x_h, y_h), \end{aligned} \tag{2.1}$$

where * denotes the complex conjugate.

From the four terms of the right hand side of equation 2.1, the first term is a constant when the reference beam is uniform across the hologram (plane reference wave) [73]. The second term is the intensity distribution of the free-space propagated object field. This is also referred to as the halo. The third term is the out-of-focus optical field of the real image multiplied by the reference field. Similarly, the fourth term is the out-of-focus optical field of the virtual image multiplied by the complex conjugate of the reference field. The reference field is a constant for in-line holograms and a spatial sinusoid for off-axis holograms. The third and fourth terms are interesting because they are proportional to the 3D optical field of the object to recover.

In a general form, the complex amplitude of the object wave is given by

$$o(x_h, y_h) = A_o(x_h, y_h) \exp[-i\Phi_o(x_h, y_h)], \tag{2.2}$$

where A_o is the real amplitude and Φ_o is the phase.

Similarly, the complex amplitude of the reference wave is given by

$$r(x_h, y_h) = A_r(x_h, y_h) \exp[-i\Phi_r(x_h, y_h)], \tag{2.3}$$

where A_r is the real amplitude and Φ_r is the phase.

If we substitute equations 2.2 and 2.3 into equation 2.1, the recorded intensity becomes

$$I = I_o[1 + m\cos(\Delta\Phi)], \tag{2.4}$$

where I_o is the mean intensity

$$I_o = |A_r(x_h, y_h)|^2 + |A_o(x_h, y_h)|^2;$$

m is the contrast

$$m = \frac{2\,|A_r(x_h, y_h)|\,|A_o(x_h, y_h)|}{|A_r(x_h, y_h)|^2 + |A_o(x_h, y_h)|^2};$$

and $\Delta\Phi$ is the phase difference

$$\Delta\Phi = \Phi_r - \Phi_o.$$

It is clear from equation 2.4 that the mean intensity and contrast only depend on the amplitudes of the optical fields, whereas the cosine is function of their relative phases. Thus, information about both amplitude and phase of the object field has been recorded in the third and fourth terms of the interferogram 2.1.

2.2.2 Wavefront Reconstruction

Analogous to conventional optical holography, the first step in the digital reconstruction process is to multiply the recorded hologram by the computer generated complex conju-

gate of the reference wave used in the recording step. The modified intensity distribution becomes:

$$\begin{aligned}\hat{I}(x_h, y_h) &= r_d^*(x_h, y_h) \cdot I(x_h, y_h) \\ &= r_d^*(x_h, y_h) \cdot [|r(x_h, y_h)|^2 + |o(x_h, y_h)|^2] \\ &\quad + |r(x_h, y_h)|^2 \, o^*(x_h, y_h) + r^*(x_h, y_h)^2 o_h(x_h, y_h).\end{aligned} \tag{2.5}$$

The combination of the first two terms of equation 2.5 is the so-called DC term or Zero order term. It represents the undiffracted field that propagates parallel to the optical axis. For in-line holography, it is usually correct to assume that the magnitude of the object wave is much smaller than the amplitude of the reference wave ($|o(x_h, y_h)| << A_r(x_h, y_h)$). If this condition is fulfilled, the effect of the DC term on the reconstructions is very small and can therefore be neglected [74]. In cases where this assumption is no longer valid, several algorithms may be implemented to suppress the DC term. These will be discussed in Chapter 5.

The third term of equation 2.5 contains the desired optical field multiplied by a constant factor. This field is located at the hologram plane, where a free-space propagation is needed to recover the 3D field of the sampled object (the real image). The fourth term corresponds to a wavefront similar to the object field incident on the recording plane but with opposite curvature (the virtual image). This term is out-of-focus and represents the most significant limitation because it introduces artifacts in the reconstruction. In off-axis holography, the DC term and the twin images (real and virtual images) are spatially separated and the real image (with no artifacts) can be retrieved.

The second step in the wavefront reconstruction process is to compute the field at an image plane separated by a distance d from the hologram plane as shown in Figure 2-5. In DHI, this free-space propagation is done by means of diffraction and Fresnel transformations, as opposed to conventional holography, which is done optically.

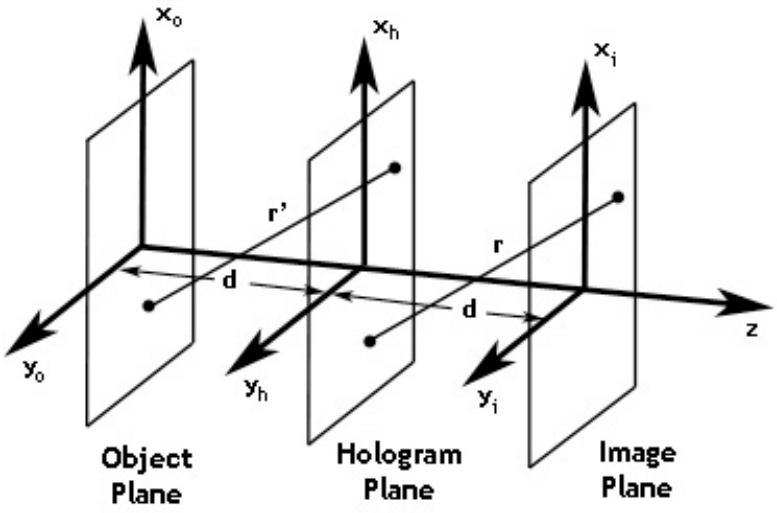

Figure 2-5: Coordinate system for holographic imaging system.

Using the Huygens-Fresnel theory of diffraction as predicted by the first Rayleigh-Sommerfeld solution [52], the optical field at the image plane is given by

$$E(x_i, y_i) = \frac{1}{i\lambda} \int_{-\infty}^{\infty} \int_{-\infty}^{\infty} \hat{I}(x_h, y_h) \frac{\exp(ikr)}{r} \cos\theta dx_h dy_h, \tag{2.6}$$

where λ is the laser wavelength and k is the wavenumber given by $k = 2\pi/\lambda$.

The variable r is the distance between a point in the hologram plane and a point in the image plane, given by

$$r = \sqrt{(x_i - x_h)^2 + (y_i - y_h)^2 + d^2}, \tag{2.7}$$

and the obliquity factor $\cos\theta$ is given by

$$\cos\theta = \frac{d}{r}. \tag{2.8}$$

If we substitute equations 2.7 and 2.8 into equation 2.6 we get:

$$E(x_i, y_i) = \frac{d}{i\lambda} \int_{-\infty}^{\infty} \int_{-\infty}^{\infty} \hat{I}(x_h, y_h) \frac{\exp\left(\frac{i2\pi}{\lambda}\sqrt{(x_i - x_h)^2 + (y_i - y_h)^2 + d^2}\right)}{(x_i - x_h)^2 + (y_i - y_h)^2 + d^2} dx_h dy_h. \quad (2.9)$$

Equation 2.9 has the form of a two-dimensional (2D) linear convolution and may be written as

$$\begin{aligned} E(x_i, y_i) &= \int_{-\infty}^{\infty} \int_{-\infty}^{\infty} \hat{I}(x_h, y_h) h_e(x_i - x_h, y_i - y_h; d) dx_h dy_h \quad (2.10) \\ &= \{\hat{I}(x, y) * * h_e(x, y; d)\}|_{x=x_i, y=y_i}, \end{aligned}$$

where ** indicates a 2D linear convolution, and

$$h_e(x, y; d) = \frac{d}{i\lambda} \frac{\exp\left(\frac{i2\pi}{\lambda}\sqrt{x^2 + y^2 + d^2}\right)}{x^2 + y^2 + d^2}, \quad (2.11)$$

is the exact diffraction kernel for a fixed reconstruction distance d. This kernel is also known as the Point Spread Function (PSF) or the impulse response of the optical system.

The exact diffraction kernel of equation 2.11 can be simplified using the paraxial or Fresnel approximation. This approximation is valid if the lateral quantities $(x_o - x_h)$ and $(y_o - y_h)$ p22]mtt8Δˆ]nt8m;2Δ]m;ˆ8)n4t]2Δ;mˆIm]ˆa,)8=22]mtt2Δ22]mtt2J]m>.]o>a,)t2Eu>

M A k k A G H A < k hl.J0θE∂>>Ak0E>i>/LHMH0/g>EkHk/θvvE/∂πJgJA
<θθE∂>>hkπEu>h∂kkθθE∂>>∂∂Eu>>/θθHHEuπ/JokAJgJlJ0θE∂>>kkθθE∂>>θkhE∂>>uθHHE

R

or

$$d >> \sqrt[3]{\frac{1}{8}\frac{[(x_i - x_h)^2 + (y_i - y_h)^2]^2}{\lambda}}. \tag{2.14}$$

Then equation 2.7 becomes:

$$r = d + \frac{(x_i - x_h)^2}{2d} + \frac{(y_i - y_h)^2}{2d}. \tag{2.15}$$

If we substitute equation 2.15 into equation 2.6, we find the paraxial-approximated diffraction integral as

$$\hat{E}(x_i, y_i) = \frac{\exp(i\frac{2\pi d}{\lambda})}{i\lambda d} \int_{-\infty}^{\infty}\int_{-\infty}^{\infty} \hat{I}(x_h, y_h) \exp\left(\frac{i\pi}{\lambda d}[(x_i - x_h)^2 + (y_i - y_h)^2]\right) dx_h dy_h, \tag{2.16}$$

or, expressed as a 2D linear convolution,

$$\begin{aligned} \hat{E}(x_i, y_i) &= \int_{-\infty}^{\infty}\int_{-\infty}^{\infty} \hat{I}(x_h, y_h) h_f(x_i - x_h, y_i - y_h; d) dx_h dy_h \\ &= \{\hat{I}(x, y) * * h_f(x, y; d)\}|_{x=x_i, y=y_i}, \end{aligned} \tag{2.17}$$

where

$$h_f(x, y; d) = \frac{1}{i\lambda d} \exp\left[\frac{i\pi}{\lambda d}(x^2 + y^2)\right]. \tag{2.18}$$

The Fresnel kernel of equation 2.18 is a 2D linear chirp function (i.e. it has a quadratic phase structure.) The multiplicative constant phase factor $\exp(i\frac{2\pi d}{\lambda})$ has been dropped, as it does not significantly affect the reconstruction. The Fourier transform of this kernel is analytically available and is also a 2D linear chirp function in the frequency domain:

$$\begin{aligned} H_f(u, v; d) &= \Im\{h_f(x, y; d)\} \\ &= \exp\left[-i\pi\lambda d(u^2 + v^2)\right]. \end{aligned} \tag{2.19}$$

The Fourier transform of the kernel in equation 2.19 is also referred to as the transfer

function (TF) of the system. The local spatial frequency of the TF is defined as the derivative of the phase:

$$\begin{aligned} u(x) &= \frac{1}{2\pi}\frac{\partial\left(\frac{\pi}{\lambda d}(x^2+y^2)\right)}{\partial x} = \frac{x}{\lambda d}, \\ v(y) &= \frac{1}{2\pi}\frac{\partial\left(\frac{\pi}{\lambda d}(x^2+y^2)\right)}{\partial y} = \frac{y}{\lambda d}. \end{aligned} \tag{2.20}$$

As the approximated Fresnel kernel has an analytic Fourier transform, we find ourselves at liberty to implement a computationally efficient reconstruction algorithm called the "convolution approach". In the convolution approach, the numerical reconstruction is done in the frequency domain with the help of the fast Fourier transform (FFT) algorithm.

Regardless of the algorithm implemented in the reconstruction step, the retrieved field has a complex form enabling information about the phase and intensity distribution to be computed [81]. The intensity of the field at a given reconstruction distance d is:

$$I(x_i, y_i) = |E(x_i, y_i)|^2 . \tag{2.21}$$

The phase is calculated by

$$\tan[\Phi(x_i, y_i)] = \frac{\mathrm{Im}[E(x_i, y_i)]}{\mathrm{Re}[E(x_i, y_i)]}, \tag{2.22}$$

where Re and Im denote the real and imaginary parts respectively.

Phase-shifting algorithms have been suggested in order to remove the artifacts introduced by the DC term and the virtual image in the reconstruction [75], [76]. The key focus in phase-shifting holography is to record several holograms (a minimum of three) with each having the reference wave phase-shifted by a certain amount. Several devices can be applied to produce the desired phase-shift in the reference wave including: piezoelectric transducer mirrors, liquid-crystal retarders and waveplates. These devices

are usually sensitive to vibrations and require a very precise control. Phase-shifting algorithms require a more complicated optical set-up and numerical algorithms. In some cases, phase-shifting holography cannot be applied, as the object is moving or it changes over time. Recent work in single-exposure phase-shifting hologrammetry may reduce or solve some of these limitations [77], [78].

2.2.3 Recording Set-ups

Selecting the appropriate recording set-up in a holographic experiment is a very important step, which usually depends on the characteristics of the object to be imaged. Typically, objects are classified according to their ability to transmit light, namely: transparent, semi-transparent, or opaque. They are also categorized according to their reflectivity properties as: pure absorptive, weakly reflective or strong reflective.

In addition to in-line and off-axis configurations, experimental set-ups are classified according to their recording set-ups. Recording set-ups may be arranged either with transmission or reflective geometry. With transmission geometry, the forward scattered light from the object interferes with a uniform reference wave at the detector plane to form a hologram. With reflection geometry, the backward scattered light from the object contributes to the hologram formation. Figure 2-6 shows a simple scattering model from a single object illuminated with a coherent plane-wave.

The simplest recording set-up is the in-line single-beam configuration. In this configuration the laser source is low-pass filtered to remove impurities in the wavefront. This is usually achieved with a combination of a microscope objective and a pinhole. The microscope objective focuses the incoming light to its focal point. At the same focal plane, a pinhole is placed to block the high-frequency content of the optical field. This activity is a simple spatial filtering operation. A second lens is placed one focal length apart from

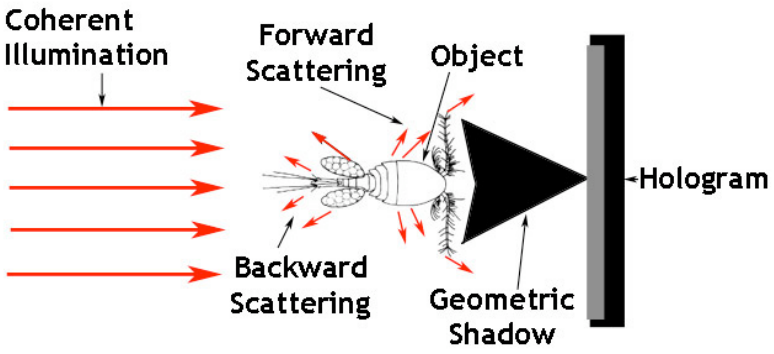

Figure 2-6: Scattering model for single object.

the pinhole to collimate and expand the light beam. The expanded plane wave is used to illuminate the small object (or several cleaned small objects) contained in a transparent medium. The undiffracted portion of the plane wave serves as a reference wave and the light scattered from the objects forms the object wave. These two waves interfere at the detector plane forming a hologram, which is then digitally recorded. Figure 2-7 shows the main components used in this set-up.

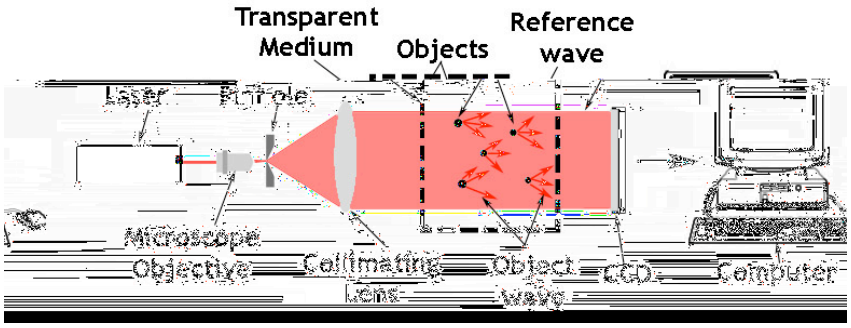

Figure 2-7: In-line single-beam recording set-up.

In the previous set-up, the reference wave is corrupted while propagating through the transparent medium. As explained in the following chapter, the quality of the holograms

may be degraded if the number of imaged particles increases. Other effects have been neglected including: multi-scattering (scattering produced by particles that are close together); change of polarization of the incoming light; and extinction of the illumination source as it propagates through the medium. If a clean reference beam is desired, the expanded beam may be split into two different paths (the reference beam and the object beam) and later recombined to record the hologram. This is usually accomplished with a Mach-Zehnder interferometer, such as the one shown in Figure 2-8.

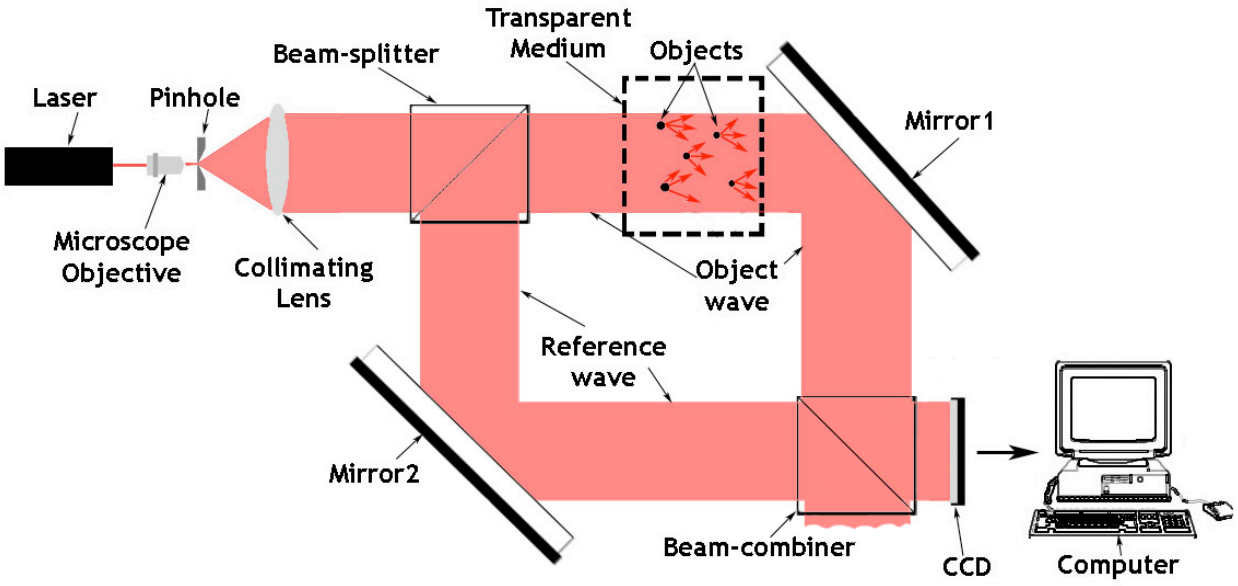

Figure 2-8: In-line Mach-Zehnder set-up: clean reference beam.

In the in-line Mach-Zehnder set-up shown in Figure 2-8, the object wave is composed of both the corrupted undiffracted field and the light scattered by the objects. An alternative configuration to remove the undiffracted field is the modified in-line Mach-Zehnder with a high-pass Fourier filter (equivalent to dark illumination used in standard microscopy). In this set-up, a 4f system (i.e. an astronomical telescope) is introduced to the object's path before recombining again with the reference wave at the hologram plane.

The 4f system consists of a pair of lenses (with the same focal length) separated two focal lengths from each other. In the center of the 4f system (the Fourier plane) a high-pass filter is inserted. The high-pass filter blocks the low-frequency DC term and enables the higher-frequency information of the optical field to pass. The Fourier transform of the undiffracted plane wave or DC term is a delta function (or more precisely a Jinc function [52]) manifested as a "bright dot" located at the center of the Fourier plane. By blocking this "bright dot," we are effectively removing the DC term and only the remaining light is scattered by the objects. The modified in-line Mach-Zehnder set-up with high-pass Fourier filter is shown in Figure 2-9.

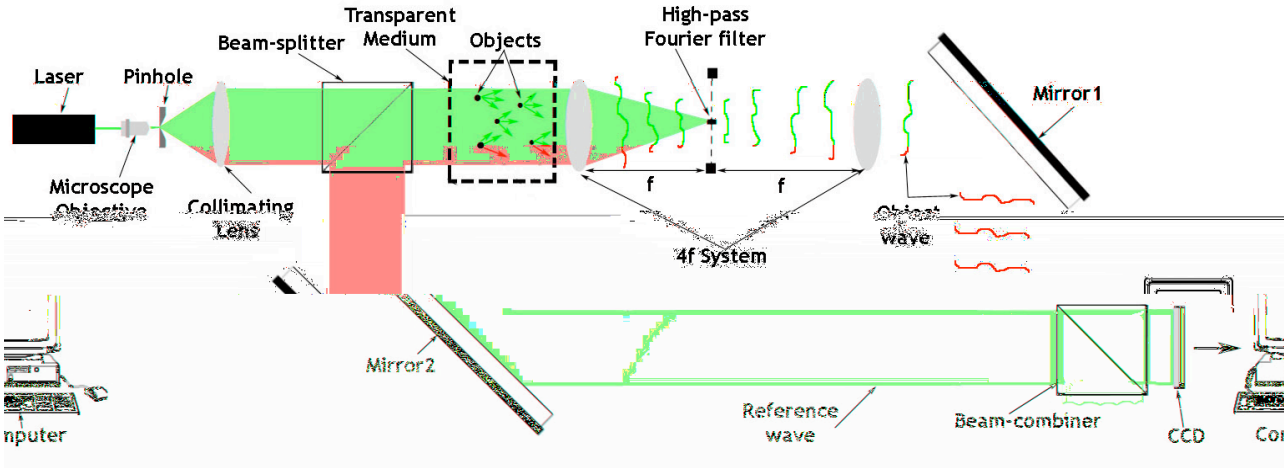

Figure 2-9: Modified in-line Mach-Zehnder set-up with high-pass Fourier filter.

Another modification of the in-line Mach-Zehnder configuration may be implemented if the relative intensities of the object and reference waves need to be tuned to maximize fringe contrast. Variable attenuation can be achieved by inserting a neutral density filter or a pair of polarizers in the reference path. An alternative method is to exchange the first beam-splitter of the Mach-Zehnder configuration to a polarized beam-splitter and to insert two half-waveplates as shown in Figure 2-10. The rotation of the first half-waveplate will cause one beam to decrease in intensity while the other beam becomes

brighter. In order to tune the global power of the system, these variable attenuation techniques can also be applied before the spatial filter.

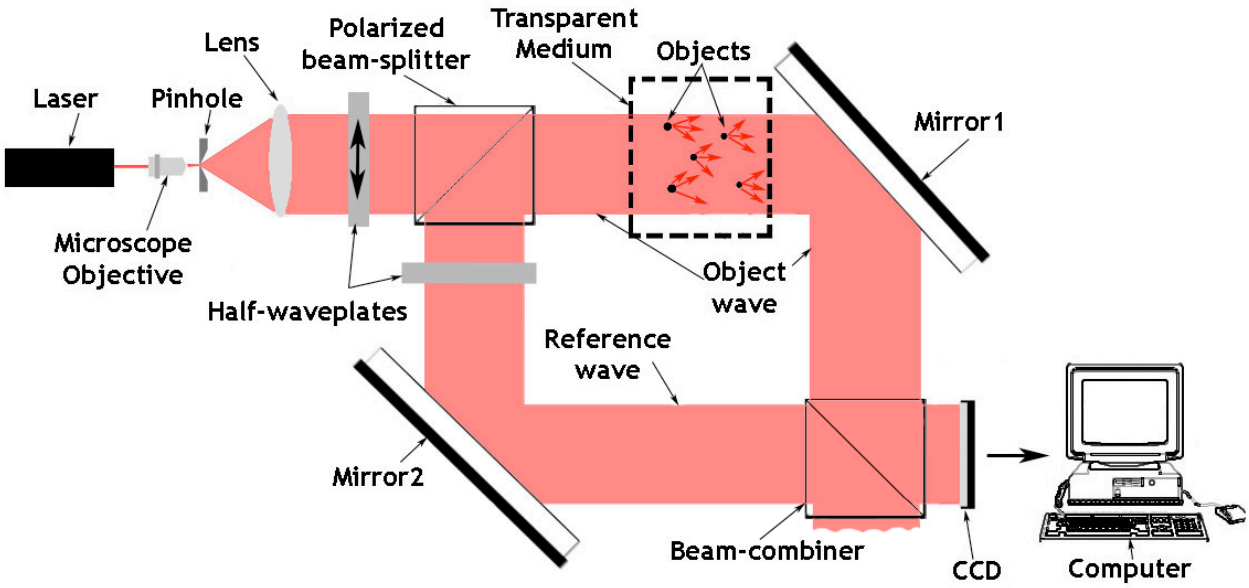

Figure 2-10: Modified in-line Mach-Zehnder set-up with variable attenuator.

Recording set-ups can also be designed to use a spherical reference wave as the carrier in the hologram formation. An example of a simple set-up using a spherical reference wave is shown in Figure 2-11. In this configuration, the recorded fringes contain additional chirp and therefore a corrective quadratic phase term has to be included in the numerical reconstruction. The interference fringes are magnified allowing the reconstruction of smaller features of the object. However, the conical shape of the illuminating beam reduces the sampled area.

In applications that require additional magnification, such as in digital holographic microscopy [82], [83], [84], [85], an optical magnification module can be inserted before

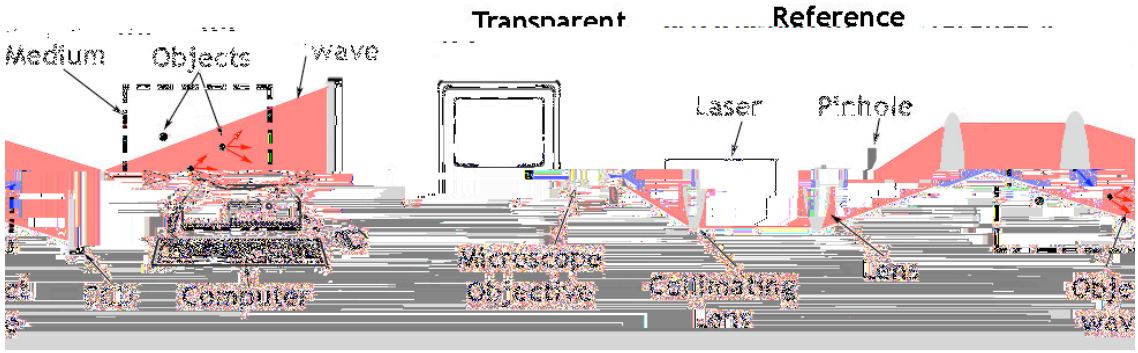

Figure 2-11: In-line set-up with a spherical reference wave.

the CCD. Optical magnification modules may be designed in different configurations including: microscope, telescope and telephoto systems.

As mentioned previously, an alternative configuration for recording in-line holograms is the reflection geometry, where the system is arranged as a Michelson interferometer. With this configuration, the input beam is also spatially filtered and collimated. A single beam-splitter divides the beam in two paths forming the reference and object waves. A mirror is placed normal to the reference wave to reflect the incident beam back into the system. The object beam illuminates the sample and the reflected light (backward scatter light) is recombined again with the same beam-splitter. Both beams interfere at the detector plane forming the hologram. The main components used in this set-up are shown in Figure 2-12.

In addition to in-line set-ups, off-axis configurations are easily made from the geometries discussed by tilting a mirror and causing the reference wave to be incident at a small angle respective to the object wave.

Further analysis and experimental results obtained using the recording set-ups presented in this subsection will be further examined in Chapter 4. Additional configurations

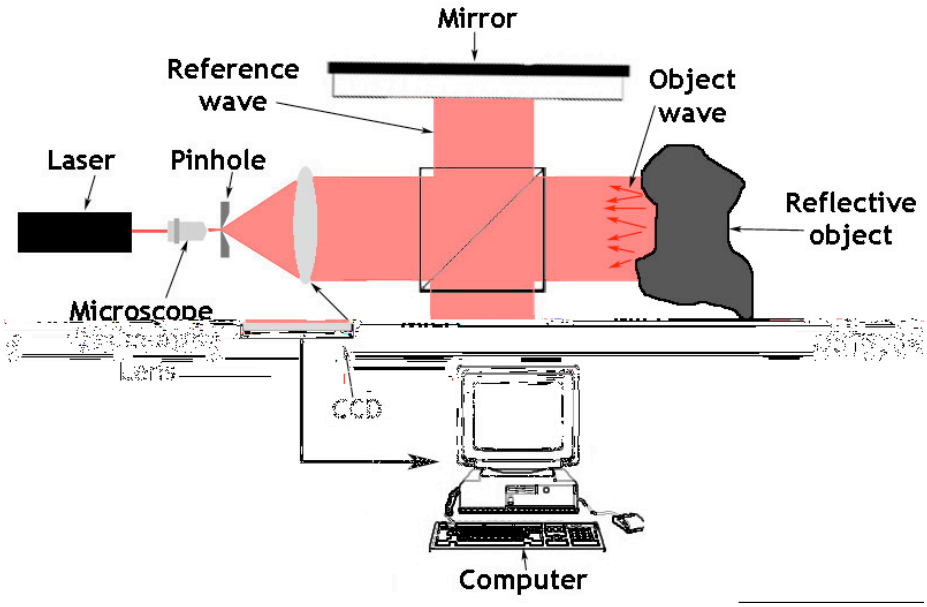

Figure 2-12: In-line set-up with reflection geometry.

such as Fourier and lens-free Fourier digital holographic set-ups will not be discussed, as they are not applicable for underwater imaging.

2.3 Numerical Reconstruction

The analytical derivations for the recording and reconstruction processes were carried out for the case of continuous functions. In reality, the numerical reconstruction in DHI is done by computers and therefore a discrete form of the reconstruction algorithms have to be implemented. For this reason two reconstruction algorithms, the Fresnel approximation and the convolution approach, are discussed in their discrete forms.

2.3.1 Reconstruction by the Fresnel Approximation

The reconstruction by the Fresnel approximation was presented in the continuous form in equation 2.16 of section 2.2.2. An equivalent form of this equation is given by

$$\begin{aligned}\hat{E}(x_i, y_i) &= \frac{\exp(i\frac{2\pi d}{\lambda})}{i\lambda d}\exp\left[i\pi\lambda d(\xi^2+\eta^2)\right]\int_{-\infty}^{\infty}\int_{-\infty}^{\infty}\hat{I}(x_h, y_h) \\ &\quad\times\exp\left[-i2\pi\left(x_h\xi + y_h\eta\right)\right]\exp\left[\frac{i\pi}{\lambda d}\left({x_h}^2+{y_h}^2\right)\right]dx_h dy_h,\end{aligned} \tag{2.23}$$

where:

$$\begin{aligned}\xi &= \frac{x_i}{\lambda d}, \\ \eta &= \frac{y_i}{\lambda d}.\end{aligned} \tag{2.24}$$

Equation 2.23 is termed Fresnel transformation. This equation reconstructs the real image at a distance d from the CCD. In order to reconstruct the virtual image, a virtual lens needs to be included in the reconstruction [86]. Similar to conventional optical holography, where the virtual image is composed of a bundle of rays diverging from the hologram plane, the virtual lens focuses the light to form the image of the original object. The complex factor introduced by the virtual lens with focal length f is given by

$$L(x_h, y_h) = \exp[i\frac{\pi}{\lambda f}(x_n^2 + y_h^2)]. \tag{2.25}$$

For a magnification of 1 a focal length of $f = d/2$ has to be implemented [80]. An extra quadratic phase factor has to be included in the reconstruction in order to compensate for the defocus introduced by the virtual lens of equation 2.25. The correction phase factor is given by

$$P(x_i, y_i) = \exp[i\frac{\pi}{\lambda f}(x_i^2 + y_i^2)] \tag{2.26}$$

Therefore, the reconstruction of the virtual image using the Fresnel approximation is given by

$$\begin{aligned}\hat{E}(x_i, y_i) &= \frac{\exp(i\frac{2\pi d}{\lambda})}{i\lambda d} P(x_i, y_i) \int_{-\infty}^{\infty}\int_{-\infty}^{\infty} \hat{I}(x_h, y_h) L(x_h, y_h) \\ &\quad \times \exp\left(\frac{i\pi}{\lambda d}[(x_i - x_h)^2 + (y_i - y_h)^2]\right) dx_h dy_h.\end{aligned} \tag{2.27}$$

The coordinates used in the equations above are the same as shown in Figure 2-5 of section 2.2.2.

In the recording step, the CCD samples the hologram in a regular lattice. CCDs are composed of $M \times N$ pixels distributed in a grid. Each pixel has a lateral extend of Δx and Δy in the x and y directions respectively. It is assumed that the requirements imposed by the sampling theorem have been met in the recording step. These conditions will be studied in more detail in Chapter 3. The discrete form of the Fresnel transformation (equation 2.23) is given by

$$\begin{aligned}\hat{E}(m, n) &= \frac{\exp(i\frac{2\pi d}{\lambda})}{i\lambda d} \exp\left[i\pi\lambda d(m^2\Delta\xi^2 + n^2\Delta\eta^2)\right] \sum_{k=0}^{M-1}\sum_{l=0}^{N-1} \hat{I}(k, l) \\ &\quad \times \exp\left[-i2\pi\left(k\Delta x_h m\Delta\xi + l\Delta y_h n\Delta\eta\right)\right] \exp\left[\frac{i\pi}{\lambda d}\left(k^2{\Delta x_h}^2 + l^2{\Delta y_h}^2\right)\right],\end{aligned} \tag{2.28}$$

for

$$m = 0, 1, 2..., M-1; n = 0, 1, 2, ..., N-1.$$

Given the Fourier transform relationships:

$$\begin{aligned}\Delta\xi &= \frac{1}{M\Delta x_h}, \qquad \Delta\eta = \frac{1}{N\Delta y_h}; \\ \Delta x_i &= \frac{\lambda d}{M\Delta x_h}, \qquad \Delta y_i = \frac{\lambda d}{N\Delta y_h};\end{aligned} \tag{2.29}$$

after substitution of equations 2.29 into equation 2.28 we get:

$$\begin{aligned}\hat{E}(m,n) &= \frac{\exp(i\frac{2\pi d}{\lambda})}{i\lambda d}\exp\left[i\pi\lambda d(\frac{m^2}{M^2\Delta x^2}+\frac{n^2}{N^2\Delta y^2})\right]\sum_{k=0}^{M-1}\sum_{l=0}^{N-1}\hat{I}(k,l) \\ &\quad\times\exp\left[-i2\pi\left(\frac{km}{M}+\frac{ln}{N}\right)\right]\exp\left[\frac{i\pi}{\lambda d}\left(k^2{\Delta x_h}^2+l^2{\Delta y_h}^2\right)\right].\end{aligned} \tag{2.30}$$

The discrete Fresnel transform can also be computed using the fast Fourier transform (FFT) algorithms. First the matrices $\hat{I}(k,l)$ and $\exp\left[(i\pi/\lambda d)\left(k^2{\Delta x_h}^2+l^2{\Delta y_h}^2\right)\right]$ are computed and the Fourier transform is applied. The result is then multiplied by the phase factor in front of the discrete sums of equation 2.30 in order to reconstruct the final image.

The sample distances in the reconstructed image, Δx_i and Δy_i, as given by equation 2.29, are functions of the imaging distance, the recording wavelength and the size of the hologram. This produces reconstructions sampled in projective rather than Cartesian coordinates, making it unsuitable for some applications including particle imaging velocimetry (PIV). In equation 2.29, the sampling rate equals the diffraction-limited resolution of the optical system. The hologram is the aperture of the optical system and equation 2.29 is the radius of the airy pattern formed in the image plane as predicted by the theory of diffraction.

2.3.2 Reconstruction by the Convolution Approach

Demetrakopoulos and Mittra were the first to implement the convolution approach for the reconstruction of holograms [88]. In 1997 Kreis applied this reconstruction technique to optical holography [89].

Making reconstructions using the convolution approach was introduced in the continuous form in equations 2.10 and 2.17 of section 2.2.2. Similarly, the exact and approximated diffraction kernels were presented in equations 2.11 and 2.18. The paraxial

approximated diffraction kernel of equation 2.18 has an analytical available Fourier transform given by equation 2.19. This property allows the reconstruction of the hologram in frequency domain by substituting the 2D convolution by a simple pointwise multiplication. The convolution approach is usually optimized by means of the FFT algorithms.

In order to discretize the diffraction kernels of equations 2.11 and 2.18 the sample rate used has to be the same as that of the hologram. Also, the kernel size has to be determined in order to avoid aliasing. Aliasing is avoided by setting the largest local frequency equal to half the inverse window size. The sample frequencies are given by

$$u_s = \frac{1}{\Delta x_h}, \quad v_s = \frac{1}{\Delta y_h}. \tag{2.31}$$

Letting L_{kx} and L_{ky} be the diffraction kernel sizes in x and y respectively, the highest spatial frequency (according to equation 2.20) is given by

$$u\left(\frac{L_{kx}}{2}\right) = \frac{L_{kx}}{2\lambda d}, \quad v\left(\frac{L_{ky}}{2}\right) = \frac{L_{ky}}{2\lambda d}. \tag{2.32}$$

To find the kernel size, the highest spatial frequency is set to be equal to half the sample frequency:

$$L_{kx} = \frac{\lambda d}{\Delta x_h}, \quad L_{ky} = \frac{\lambda d}{\Delta y_h}, \tag{2.33}$$

and the number of samples in each direction is given by

$$M_{kx} = \frac{L_{kx}}{\Delta x_h} = \frac{\lambda d}{\Delta x_h^2}, \quad N_{ky} = \frac{L_{ky}}{\Delta y_h} = \frac{\lambda d}{\Delta y_h^2}. \tag{2.34}$$

From the equations above, the discrete version of the exact and paraxial approximated

kernels are given by

$$\begin{aligned} h_e[m,n;d] &= h_e(m\Delta x_h, n\Delta y_h; d) = \frac{d}{i\lambda}\frac{\exp\left(\frac{i2\pi}{\lambda}\sqrt{(m\Delta x_h)^2+(n\Delta y_h)^2+d^2}\right)}{(m\Delta x_h)^2+(n\Delta y_h)^2+d^2} \quad (2.35) \\ h_f[m,n;d] &= hf(m\Delta x_h, n\Delta y_h; d) = \frac{1}{i\lambda d}\exp\left[\frac{i\pi}{\lambda d}((m\Delta x_h)^2+(n\Delta y_h)^2)\right], \end{aligned}$$

for

$$m = -\frac{M_{kx}}{2}, ..., \frac{M_{kx}}{2}-1 \quad and \quad n = -\frac{N_{ky}}{2}, ..., \frac{N_{ky}}{2}-1.$$

Figure 2-13 shows the exact diffraction kernel generated for an imaging distance d =89mm and a pixel size of $\Delta x_h = \Delta y_h = 9\mu$m. The diffraction kernel was formed using a wavelength of: λ =632.8nm. The diffraction kernel is made of a group of concentric circles forming the so-called "Airy pattern". The replicas and other distortions observed in Figure 2-13 are due to moiré effects and not to aliasing in the system.

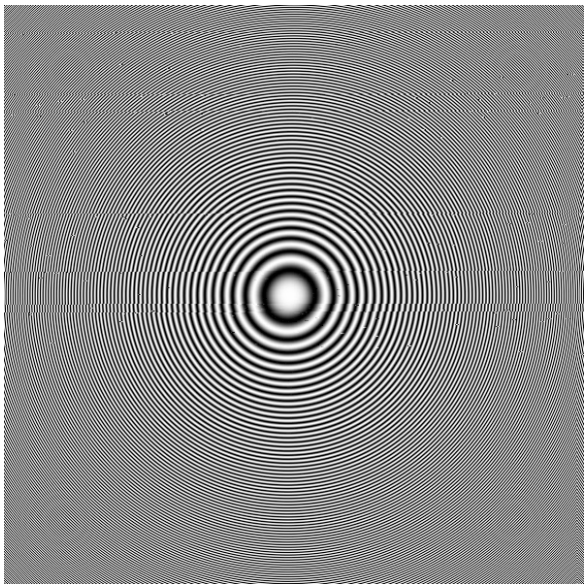

Figure 2-13: Example of an exact diffraction kernel.

Similarly, Figure 2-14 shows the paraxial approximated diffraction kernel generated

for the same parameters as that of Fig 2-13.

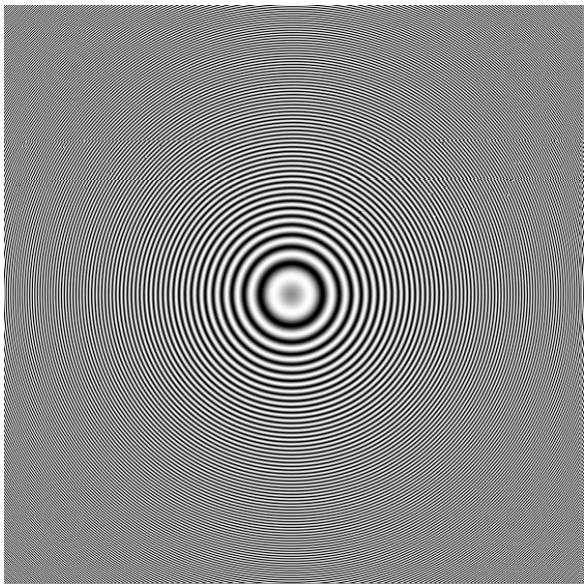

Figure 2-14: Example of a paraxial approximated diffraction kernel.

As mentioned before, the diffraction kernel is also known as the point spread function (PSF) or the impulse response of the system. Figure 2-15 shows a PSF obtained experimentally to be compared with the computer generated diffraction kernels of Figures 2-13 and 2-14. The PSF was generated from a point source located 89.3mm apart from the CCD. The point source was interfered with a plane reference wave incident normal to the CCD. The optical field was recorded with the CCD KAF-16801E from Kodak. This sensor has 4096×4096 pixels with a pixel size of: $\Delta x_h = \Delta y_h = 9\mu$m.

The experimental set-up used to record the hologram of Figure 2-15 is shown in Figure 2-16.

In order to compute the discrete form of the transfer function of equation 2.19, derived from the paraxial-approximated kernel, the sample frequency and matrix size needs to

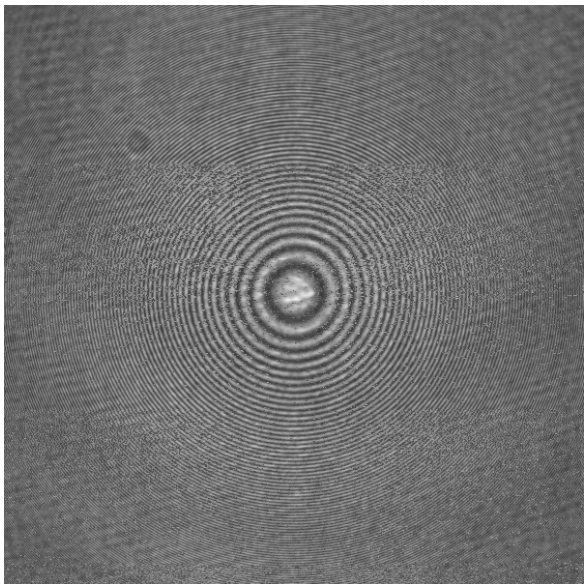

Figure 2-15: PSF obtained experimentally.

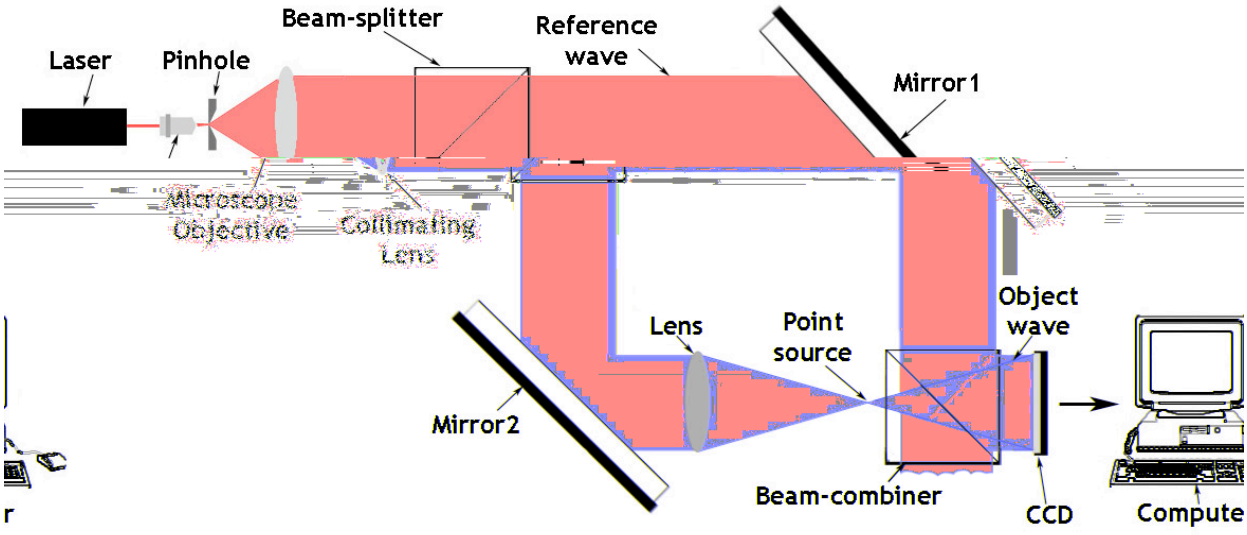

Figure 2-16: Experimental set-up used to record the PSF of the system.

be determined. The sample frequency and the matrix size of the transfer function can be the same as those of the Fourier transform of the modified hologram, equation 2.5, as both are multiplied during the reconstruction algorithm. These parameters are given by the space-bandwidth product analysis:

$$\begin{aligned} u_{\max} &= \frac{1}{2\Delta x_h}, \quad v_{\max} = \frac{1}{2\Delta y_h}; \\ du &= \frac{u_{\max}}{M} = \frac{1}{2L_{hx}}, \\ dv &= \frac{v_{\max}}{N} = \frac{1}{2L_{hy}}; \\ M_{kx} &= M, \qquad N_{ky} = N; \end{aligned} \tag{2.36}$$

where $u_{\max}$ and $v_{\max}$ are the maximum spatial frequencies in x and y respectively. These spatial frequencies are selected in order to satisfy the sampling theorem as explained in Chapter 3. Δx_h and Δy_h are the pixel sizes and du and dv are the sampling steps in both directions. L_{hx} and L_{hy} are the dimensions of the CCD and M and N are the number of pixels in both directions. Finally, M_{kx} and M_{ky} are the number of samples in x and y. From the equations above, the discrete form of the transfer function of equation 2.19 is given by

$$H_f[l,k;d] = \exp\left\{-i\pi\lambda d[(l\Delta u)^2 + (k\Delta v)^2]\right\}, \tag{2.37}$$

for

$$l = -\frac{M_{kx}}{2}, ..., \frac{M_{kx}}{2} - 1 \quad \text{and} \quad k = -\frac{N_{ky}}{2}, ..., \frac{N_{ky}}{2} - 1.$$

A transfer function generated with the same parameters as the examples of Figures 2-13 and 2-14 is shown in Figure 2-17. The replicas of the chirp function shown in Figure 2-17 are again due to moiré effect.

The first step in the reconstruction algorithm is to compute the modified hologram as indicated by equation 2.5. However, this step is skipped for a hologram recorded with a plane reference wave in an in-line configuration, as the reference wave is a real number.

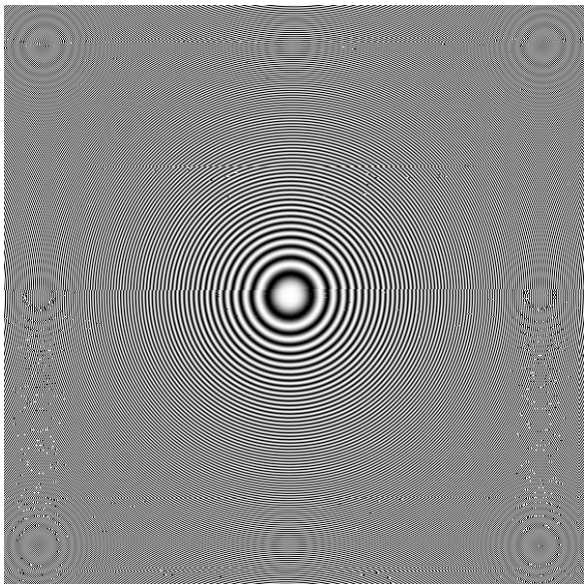

Figure 2-17: Example of a transfer function obtained from the paraxial approximated diffraction kernel.

The second step is to compute the two-dimensional Fourier transform of the modified hologram using the FFT algorithms. The third step is to generate the transfer function matrix. This matrix is computed for a given reconstruction distance, d. In the fourth step, the Fourier transform of the modified hologram and the transfer function matrix are multiplied to generate the frequency spectrum of the reconstructed optical field. The last step in this algorithm is to compute the two-dimensional inverse-Fourier transform of the matrix, obtained in the last step, to find the reconstructed optical field. Figure 2-18 shows the block diagram of the reconstruction algorithm summarizing the five required steps.

The reconstruction of the hologram shown in Figure 2-15 was performed using the algorithm shown in Figure 2-18. The point source was reconstructed at a distance of d=89.3mm from the CCD as shown in Figure 2-19. The artifacts introduced by the out-of-focus virtual image are not very severe due to the relatively large reconstruction distance, making the virtual image extremely blurry.

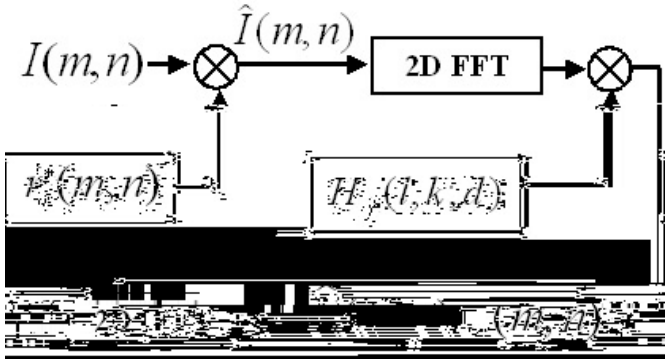

Figure 2-18: Block diagram of the reconstruction algorithm by the convolution approach.

In the convolution approach, the pixel distances of the reconstructed image are given by

$$\Delta x_i = \Delta x_h \quad \text{and} \quad \Delta y_i = \Delta y_h. \tag{2.38}$$

As opposed to the Fresnel transform, reconstruction using a convolution approach produces images of the same size for different reconstruction distances. As images of different planes have to be compared, this algorithm is more suitable for applications such as underwater imaging and PIV. When initially examining equation 2.38, it would seem that the convolution approach achieves a higher resolution than the Fresnel transform, provided that the pixel size decreases. However after a closer examination, the physical image resolution of the system is still determined by equation 2.29. This image resolution is the diffraction-limited resolution of the optical system.

In the next chapter the sampling requirements and the system resolution are discussed.

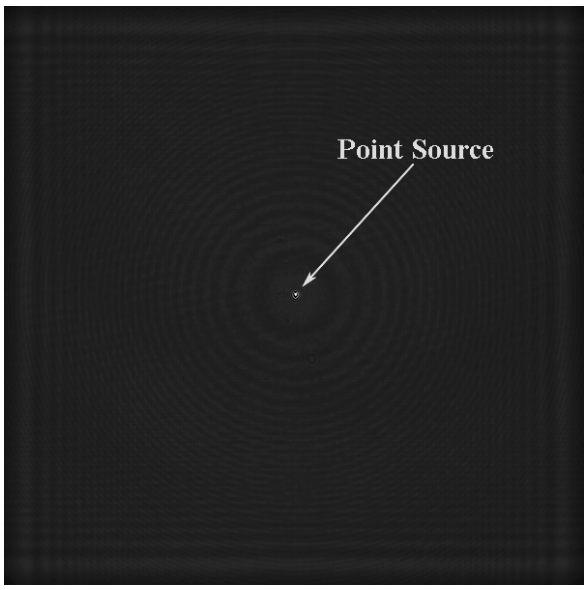

Figure 2-19: Reconstruction of the point source experiment.

Chapter 3

Sampling and Resolution

3.1 The Whittaker-Shannon Sampling Theorem

In DHI, a CCD is used to record the interference patterned formed by the sum of the reference and object waves. This step is crucial as the CCD is effectively sampling the optical field in a regular grid. Sampling schemes are directly related to the quality and efficiency of the reconstructions where quality refers to the image resolution and intelligibility and efficiency refers to computational size and speed of the reconstruction process. As mentioned in the previous chapter, the resolution of the system (equation 2.29) depends on the lateral extend of the CCD, the wavelength, and the imaging distance used in the recording step. In general, a CCD is capable of recording a hologram provided that the sampling theorem is fulfilled.

According to the Whittaker-Shannon sampling theorem, sampling a function is usually carried out in a rectangular lattice, such as the one imposed by the CCDs [52]. For a continuous bandlimited function $g(x, y)$ that represents the optical field at the (x, y) plane, the discrete function recorded by the CCD is given by

$$g_s(x, y) = \text{comb}\left(\frac{x}{\Delta x}\right) \text{comb}\left(\frac{y}{\Delta y}\right) g(x, y), \tag{3.1}$$

where Δx and Δy are the pixel sizes in x and y, respectively. The comb function is defined as:

$$\mathrm{comb}(x) = \sum_{n=-\infty}^{\infty} \delta(x-n), \tag{3.2}$$

where δ represents a delta function.

In frequency domain, equation 3.1 may be written as:

$$\begin{aligned} G_s &= \mathcal{F}\{g_x\} = \Delta x \Delta y \ \mathrm{comb}(\Delta x \cdot u)\ \mathrm{comb}(\Delta y \cdot v) * *G(x,y) \\ &= \sum_{n=-\infty}^{\infty} \sum_{m=-\infty}^{\infty} G\left(u - \frac{n}{\Delta x}, v - \frac{m}{\Delta y}\right), \end{aligned} \tag{3.3}$$

where again $**$ indicates a 2D convolution operation and u and v represent the spatial frequency in x and y respectively.

When samples are taken very close to each other, a good representation of the optical field can be expected. In the frequency domain, this means the replicas of the spectrum of the original function, which are spaced by $(1/\Delta x,\ 1/\Delta y)$, are pushed further apart. If the replicas are not overlapping an interpolation filter can be used to recover the original function exactly. The maximum spacing allowable in the sampling lattice is given by

$$\Delta x \leq \frac{1}{2B_x}, \quad \Delta y \leq \frac{1}{2B_y}, \tag{3.4}$$

where B_x and B_y are the bandwidths in the u and v directions.

To determine the bandwidth in DHI, we have to consider both the bandwidth of the object wave and the finite size of the CCD. In a more strict form, the function sampled by the CCD may be written as [90]:

$$\begin{aligned} g_s(x,y) &= \left[\mathrm{rect}\left(\frac{x}{\alpha\Delta x}\right)\mathrm{rect}\left(\frac{y}{\beta\Delta y}\right) * *\mathrm{comb}\left(\frac{x}{\Delta x}\right)\mathrm{comb}\left(\frac{y}{\Delta y}\right)\right] \\ &\quad \times \mathrm{rect}\left(\frac{x}{N\Delta x}\right)\mathrm{rect}\left(\frac{y}{M\Delta y}\right) g(x,y), \end{aligned} \tag{3.5}$$

where α and β are the fill factors in each direction ranging from 0 to 1. Also, N and M are the number of pixels in x and y. In this representation, both the size of the rectangular pixel and the size of the CCD have been considered. The rect function of equation 3.5 is defined as:

$$\text{rect}(x) = \begin{cases} 1 & |x| < \frac{1}{2} \\ \frac{1}{2} & |x| = \frac{1}{2} \\ 0 & \text{otherwise} \end{cases} . \tag{3.6}$$

A one dimensional model to estimate the required bandwidth is shown in Figure 3-1. As shown in this model, the object and the CCD are centered on the optical axis and the object has been illuminated by a coherent monochromatic plane wave. It is assumed the span of the reference wave is larger than the size of the CCD and therefore the entire photosensitive area is covered.

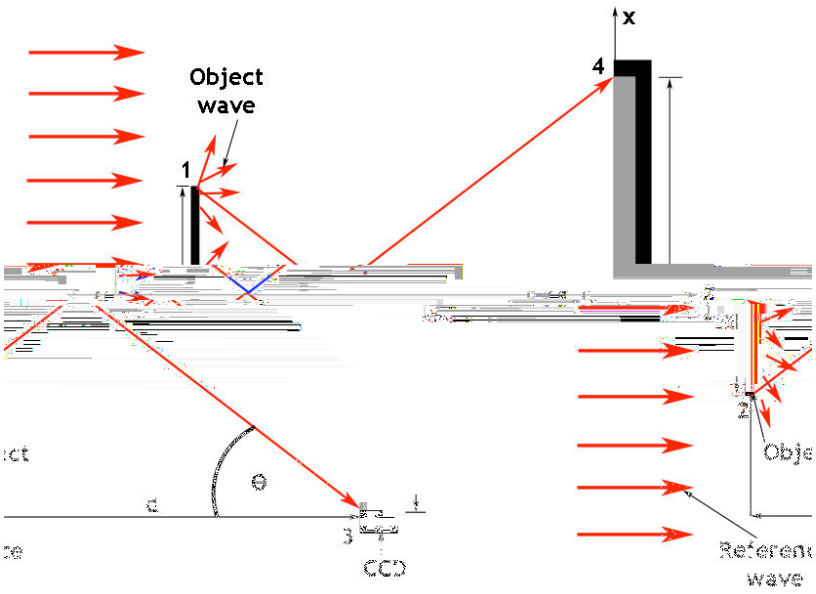

Figure 3-1: 1D model of the bandwidth for a hologram formation in a CCD.

As the reference wave is propagating parallel to the optical axis, the bandwidth of

the interference field equals the bandwidth of the object wave. Although the object field can be modeled as a collection of plane waves emanating from the object at different directions, only waves that intersect the CCD are of interest. The angular spectrum of the object is given by the largest spatial frequency that corresponds to a plane wave propagating from point 1 (or 2) to 3 (or 4):

$$u_{x\max} = \frac{\sin\theta}{\lambda} = \frac{\frac{L_{hx}+L_{ox}}{2}}{\lambda\sqrt{\left(\frac{L_{hx}+L_{ox}}{2}\right)^2 + d^2}}. \tag{3.7}$$

The paraxial approximation is used to simplify equation 3.7 such that

$$L_{hx} + L_{ox} << d,$$

$$\sqrt{\left(\frac{L_{hx}+L_{ox}}{2}\right)^2 + d^2} \approx d;$$

therefore,

$$u_{\max} = \frac{L_{hx}+L_{ox}}{2\lambda d}; \tag{3.8}$$

$$v_{\max} = \frac{L_{hy}+L_{oy}}{2\lambda d}. \tag{3.9}$$

From the results obtained in equation 3.9 we can now determine the hologram bandwidth:

$$\begin{aligned} 2B_x &= 2u_{\max} = \frac{L_{hx}+L_{ox}}{\lambda d}, \\ 2B_y &= 2v_{\max} = \frac{L_{hy}+L_{oy}}{\lambda d}. \end{aligned} \tag{3.10}$$

The optimal pixel size is found by substituting equation 3.10 in equation 3.4:

$$\begin{aligned} \Delta x &= \frac{\lambda d}{L_{hx}+L_{ox}}, \\ \Delta y &= \frac{\lambda d}{L_{hy}+L_{oy}}. \end{aligned} \tag{3.11}$$

Similarly, the number of pixels in each dimension is given by

$$\begin{aligned} N &= \frac{L_{hx}(L_{hx}+L_{ox})}{\lambda d}, \\ M &= \frac{L_{hy}(L_{hy}+L_{oy})}{\lambda d}. \end{aligned} \tag{3.12}$$

The results presented in equations 3.11 and 3.12 were derived for the least desired conditions. When practically implemented, the resolution requirements can be reduced assuming the imaged sample is composed of small sparse objects.

Another sampling requirement can be obtained if the size of the interference fringes at the hologram plane is considered. The resultant fringe spacing is given by

$$\Delta x = \frac{\lambda}{2\sin\left(\frac{\theta}{2}\right)}, \tag{3.13}$$

where θ is the angle between the reference and the object wave in hologram plane.

For a fixed CCD, the sampling theorem requires at least 2 pixels record one fringe period. Assuming small angles, $\sin\theta \approx \tan\theta \approx \theta$, the maximum allowable angle between the reference and the object wave is given by

$$\theta_{\max} = \frac{\lambda}{2\Delta x} \quad \text{or} \quad \theta_{\max} = \frac{\lambda}{2\Delta y}. \tag{3.14}$$

This is shown in the experiments presented in section 3.2, which were conducted using the CCD Kodak KAF-16801E. This CCD has 4096×4096 pixels arranged in a full-frame configuration. The pixel size is 9μm in both directions. Assuming that the hologram is recorded with a Helium-Neon laser (λ =632.8nm), the maximum allowable angle given by equation 3.14 is $\theta_{\max} = 0.035$rad$= 2.014\,^{\circ}$.

The restrictions of equation 3.14 set the minimum allowable imaging distance in order to satisfy the sampling theorem. For the in-line model, such as the one shown in Figure 3-1, the minimum allowable imaging distance as a function of object lateral extend is

given by

$$d_{\min} = \frac{N\Delta x + L_{ox}}{2\theta_{\max}} \quad \text{or} \quad d_{\min} = \frac{M\Delta y + L_{oy}}{2\theta_{\max}}. \tag{3.15}$$

For the CCD and laser described in the example above, the minimum allowable imaging distance for an in-line holographic experiment given by equation 3.15 is plotted in Figure 3-2.

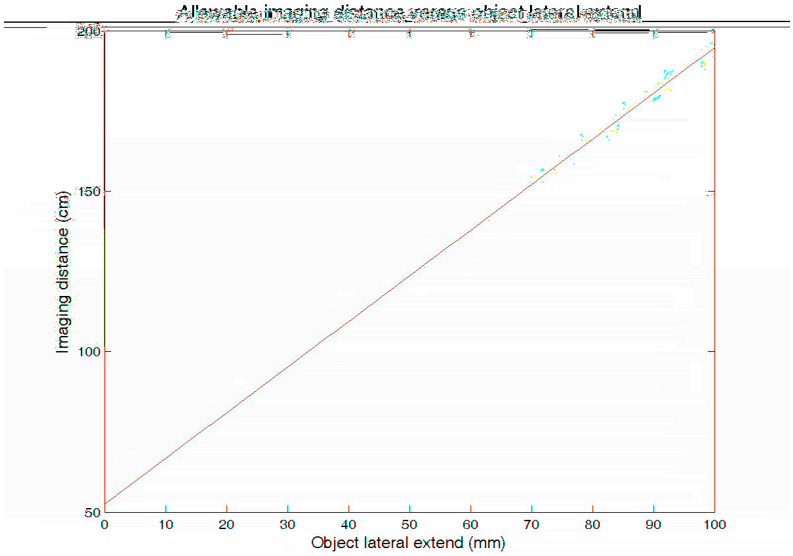

Figure 3-2: Minimum allowable imaging distance for in-line holography.

For off-axis holography, a simple model is shown in Figure 3-3. In this model, the object is located asymmetrically to the optical axis, and the reference wave is incident normal to the CCD.

In order to separate the twin-images and the DC term, the angle between the reference wave and the object wave has to be greater than the minimum angle [52]:

$$\theta_{\min} = \sin^{-1}(3\lambda u_{\max}) \quad \text{or} \quad \theta_{\min} = \sin^{-1}(3\lambda v_{\max}). \tag{3.16}$$

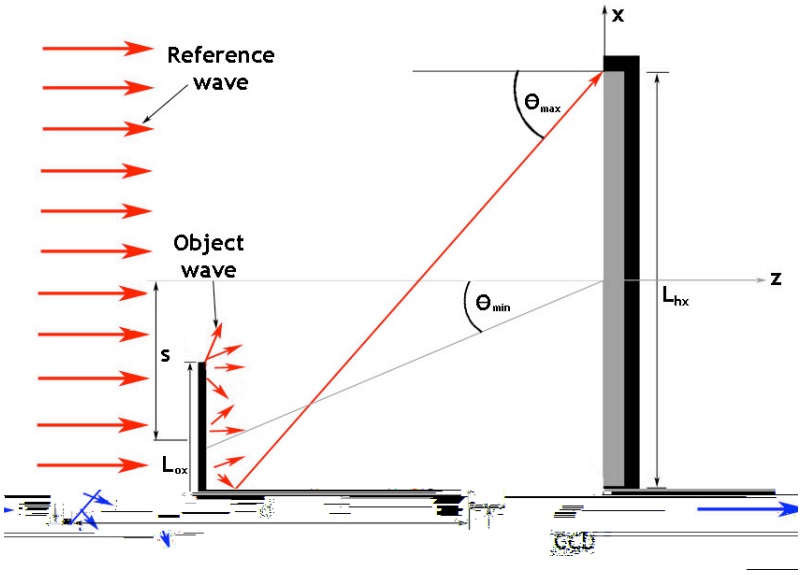

Figure 3-3: Off-axis bandwidth model.

For the highest spatial frequencies, $u_{\max}$ and $v_{\max}$, as defined in equation 3.7, the minimum allowable angle is given by

$$\theta_{\min} \approx \frac{3L_{ox}}{2d}. \tag{3.17}$$

The minimum required imaging distance is given by [91]:

$$\begin{aligned} d_{\min} &= \frac{N\Delta x + L_{ox} + 2s}{2\theta_{\max}} \\ &= \frac{N\Delta x + 4L_{ox}}{2\theta_{\max}}, \end{aligned} \tag{3.18}$$

where $s = \theta_{\min} d_{\min}$.

As shown in Figure 3-4, the requirements for off-axis holography are more extreme making it less suitable for an underwater imaging application. The curve plotted in Figure 3-4 was generated for the same parameters as the example of in-line holography.

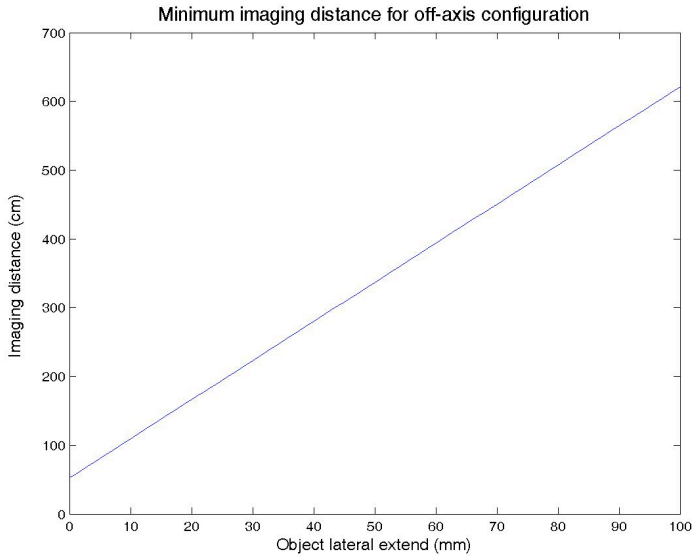

Figure 3-4: Minimum allowable imaging distance for the example of off-axis holography.

3.2 Experimental Measurement of the System's Resolution

The quality of an optical system is typically determined by the resolution criterion. The two-point resolution criterion consists on the ability of the optical system to resolve two closely spaced point sources [52]. This criterion is commonly used in astronomy to establish whether the system can resolve two stars that are close together. The resolvability of two point sources is described by the Rayleigh criterion. According to this criterion, the minimum resolvable separation between adjacent points is given by

$$\delta = 0.61\frac{\lambda}{NA} \tag{3.19}$$

where NA is the numerical aperture of the optical system, which is assumed to be aberration-free (i.e. diffraction limited.)

In DHI, the diffracted-limited resolution is given by equation 2.29 of section 2.3. In this equation it is clear that the resolution of the system also depends on the numerical aperture and wavelength used to record the hologram. This equation constitutes the radius of the Airy pattern formed in the image plane by a point source, as predicted by the Rayleigh criterion. Since most set-ups in digital holography are lens-free, aberrations produced by lenses are usually avoided. However, in in-line holography, the resolvability of two point sources is affected by the superposition of the twin images and DC term in the reconstruction.

Figure 3-5 shows the experimental set-up used to measure the resolution in an in-line digital holographic configuration. Similar to the in-line set-up of Figure 2-7 in section 2.2.3, the laser beam is spatially filtered, collimated and expanded to the required diameter. The expanded beam illuminates a positive 1951 USAF resolution target, which consists of a matrix of lines and numbers of different sizes coated on a glass plate. The field diffracted by the resolution target interferes with the undiffracted field at the CCD plane. To determine the resolution of the system, the captured hologram is reconstructed and the resulting image is analyzed.

In the experiment, a Helium-Neon laser was spatially filtered using a combination of a $60X$ microscope objective and a pinhole of 5μm. The collimating lens had a diameter of 75mm and a focal length of 150mm. The hologram was recorded on the CCD KAF-16801E from Kodak. A Frame Grabber was used for the communication between the CCD and the computer. The holograms were numerically reconstructed using the convolution approach. Figures 3-6, 3-7 and 3-8 show images of the resolution target reconstructed at different imaging distances.

As expected, the best resolution is achieved when the resolution target is located near the CCD. In Figure 3-6 (reconstruction done for $d = 12.5$mm), lines of $44 \times 8.8\mu$m

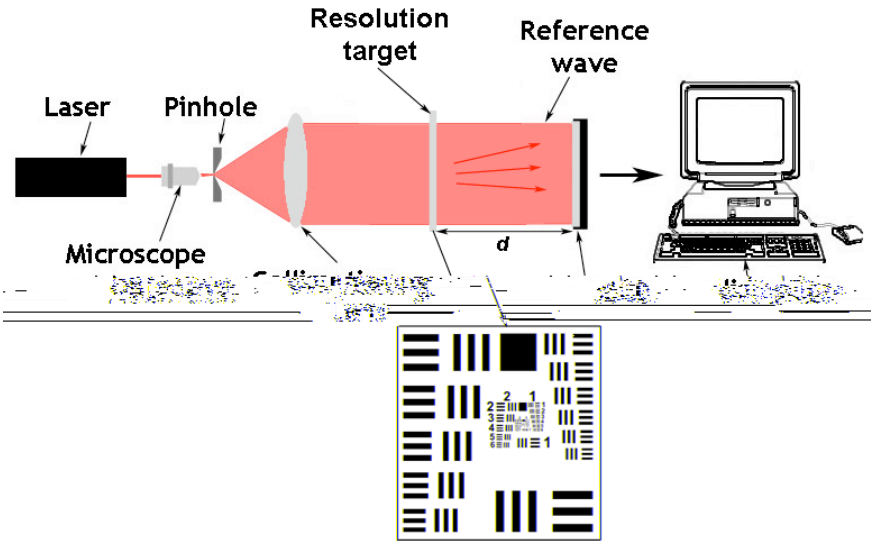

Figure 3-5: In-line set-up to measure the resolution limit in DHI.

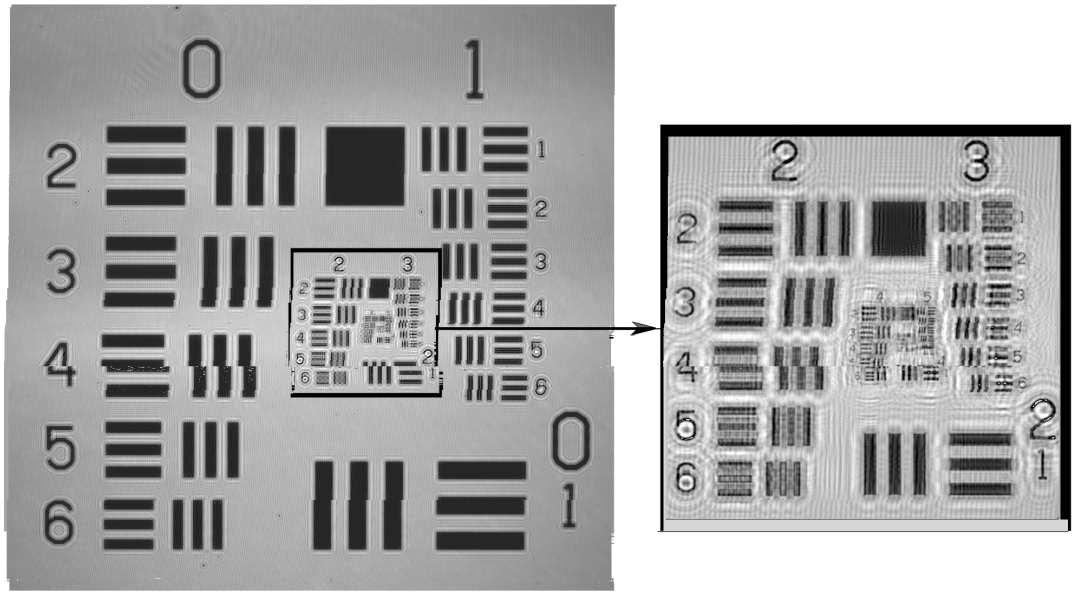

Figure 3-6: Image of a 1951 USAF resolution target reconstructed for d=12.5mm. To the left: entire resolution target. To the right: zoomed image of the second group.

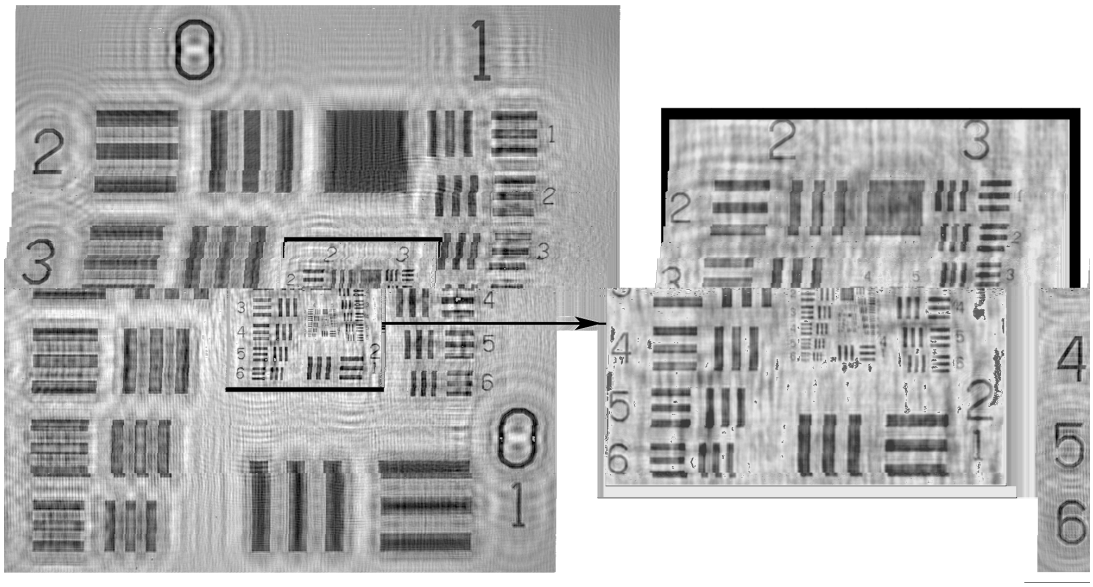

Figure 3-7: Image of a 1951 USAF resolution target reconstructed for d=286mm. To the left: entire resolution target. To the right: zoomed image of the second group.

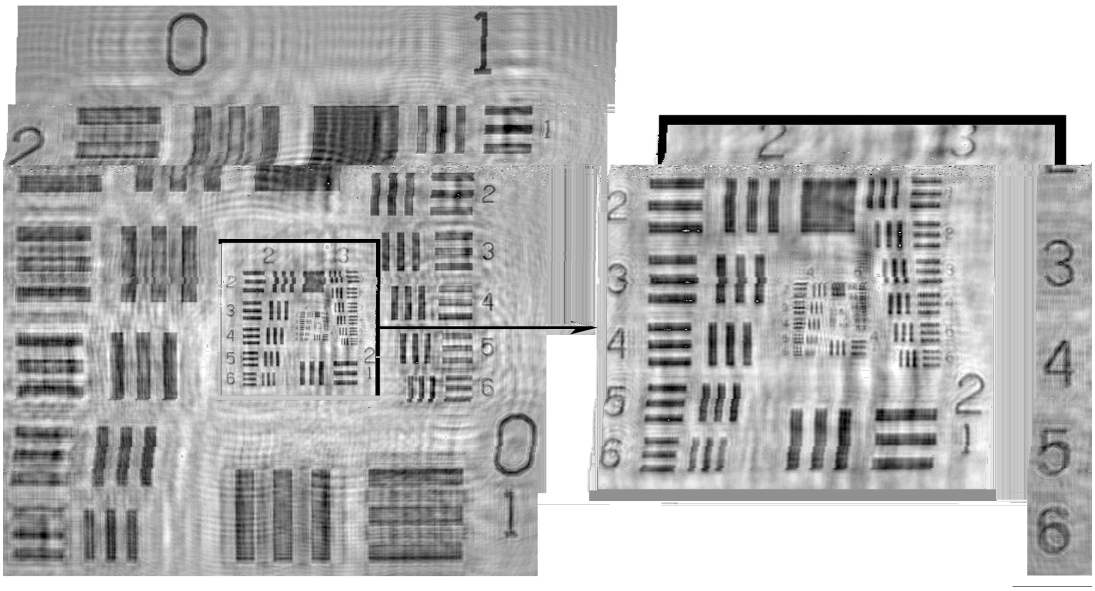

Figure 3-8: Image of a 1951 USAF resolution target reconstructed for d=600mm. To the left: entire resolution target. To the right: zoomed image of the second group.

spaced every 8.8μm can be easily resolved. The theoretical resolution limit at that imaging distance given by equation 2.29 is $0.2\mu m$. However, the resolution present in holograms reconstructed using the convolution approach is limited by the pixel size. The loss of resolution in the experimental result is mainly due to the superposition of the twin images and DC term and the phase distortion introduced by the glass plate. Also, possible vibration of the optical table may have distorted the recorded hologram.

The reconstruction shown in Figure 3-7 for $d = 286$mm presents a higher distortion than that of Figure 3-6, introduced mainly by the virtual (out-of-focus) image, which is super imposed to the real image. Again, the DC term and the glass plate limit the resolution. From the reconstructed image, lines of $60 \times 11\mu$m spaced every 11μm can be resolved. The theoretical resolution limit for this case is 5μm. Smaller features of the resolution target are blurred and barely visible due to the low-pass filtering effect produced by the finite size of the CCD.

Figure 3-8 shows the image of the resolution target reconstructed at $d = 600$mm. At this distance, lines of $88 \times 18\mu$m spaced every 18μm can be resolved. The theoretical resolution limit for this imaging distance is 10.3μm. For the smaller features, the distortion introduced by the virtual image is less severe than the one shown in Figure 3-7 since the virtual image is highly out-of-focus and produces a uniform blur. In Figure 3-8, additional distortions are introduced by the reconstruction algorithm. For computational reasons, the reconstruction algorithm truncates the kernel matrix to 4096×4096 entries. The required kernel size given by equation 2.33 is 4690×4690; therefore, the reconstructed images are additionally corrupted.

A typical hologram of the resolution target is shown in Figure 3-9.

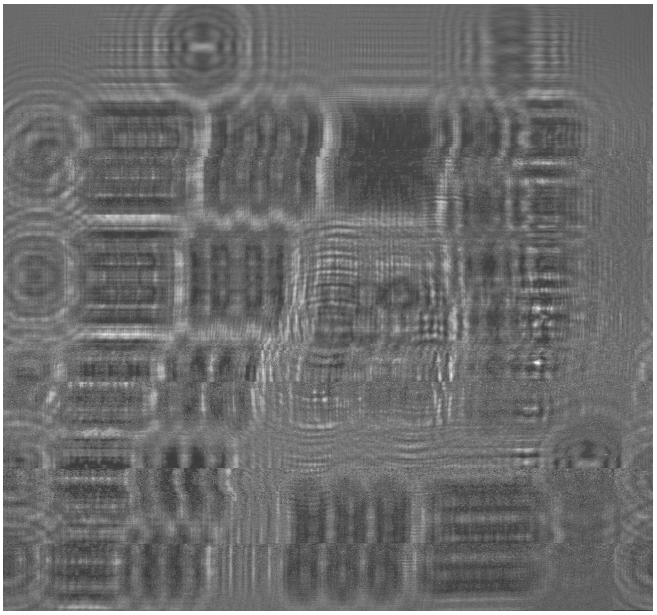

Figure 3-9: Hologram of the 1951 USAF resolution target.

Chapter 4

Digital Holographic Imaging of Aquatic Species: System Design and Experiments

In the 1960s conventional holographic imaging of aquatic species began with laboratory experiments [92], [93], [94], [95], [96]. Carder's studies in 1982 of ocean particle dynamics were fundamental to the development of in situ holographic research [97]. In 1984, Katz and O'Hern developed the first submersible holographic system based on a pulsed-laser to measure micro-particulates [98], [99]. A later version of this system, based on a ruby laser to image plankton, was published in [100] and [101]. The in-line holograms were recorded on rolls of film where they were later developed and replayed in laboratories. The immense amount of information contained in a single holographic film resulted in the development of an automated scanning and measurement technique [102]. Another submersible imaging system, the Holomar, was designed to image plankton and other marine particulates using simultaneous in-line and off-axis holography [103], [104], [105]. Studies of 3D flow fields using particle-imaging velocimetry (PIV) were conducted using double exposed holograms [106], [107], [108] (for a complete description of particle field

holography refer to [109]). A more recent version of this technique using digital holography to measure the flow field generated by a feeding copepod in the laboratory was published in [110]. In 2000, Owen and Zozula developed an in situ digital recording system to image marine particles [111]. However, this system had the limitation of sampling small volumes due to the reduced area of the CCD.

In this chapter, the design, development and evaluation of a digital holographic imaging system for aquat

In most in-line digital holographic experiments, a plane wave is used as a reference to record the hologram. The electrical field of the plane reference wave perpendicular to the y_h axis is given by

$$r(x_h, y_h) = A \exp\left[\frac{i2\pi}{\lambda}(x_h \sin\theta)\right], \tag{4.1}$$

where the time function of the form $\exp(-i\omega t)$ is implied.

As shown in Figure 2-7 of section 2.2.3, the plane wave propagates parallel to the optical axis. Therefore, $\sin\theta = 0$ and equation 4.1 reduces to the constant amplitude, typically assumed to be equal to one ($A = 1$). Thus, the recorded interference pattern is given by (from equation 2.1)

$$\begin{aligned} I(x_h, y_h) &= |1 + o(x_h, y_h)|^2 \\ &= 1 + |o(x_h, y_h)|^2 + 2\,\mathrm{Re}\{o(x_h, y_h)\}. \end{aligned} \tag{4.2}$$

Several algorithms, such as phase shifting holography, can be implemented to suppress the effect of the DC term and the virtual image in the reconstruction. In the following chapter, examples of image post-processing algorithms designed to suppress the DC term from the original hologram are discussed. From equation 4.2 it is clear that one way to eliminate the DC term from the hologram is to record two additional images. The first image consists of the intensity distribution produced by the reference wave after blocking the object wave. The second image is the intensity distribution of the object wave after blocking the reference wave. The next step is to subtract these images from the original hologram. However, this method requires additional experimental work and is only possible in set-ups such as shown in Figure 2-9.

The use of a plane reference wave in the in-line set-up simplifies the numerical reconstruction as it avoids the multiplication of the hologram by the computer generated reference wave as indicated in equation 2.5. The transfer function used during the reconstruction with the convolution approach, as indicated by equation 2.19, is simplified

to

$$\begin{aligned} H_f(u,v;d) &= \mathrm{Re}\{\exp\left[-i\pi\lambda d(u^2+v^2)\right])\} \\ &= \cos(\pi\lambda d(u^2+v^2)), \end{aligned} \tag{4.3}$$

or in discrete form:

$$H_f[l,k;d] = \cos\{\pi\lambda d[(l\Delta u)^2 + (k\Delta v)^2]\} \tag{4.4}$$

for

$$l = -\frac{M_{kx}}{2}, ..., \frac{M_{kx}}{2} - 1 \quad \text{and} \quad k = -\frac{N_{ky}}{2}, ..., \frac{N_{ky}}{2} - 1.$$

In comparison to equation 2.37, equation 4.4 is faster to compute and occupies less memory space as it is only composed of real numbers. For example, two transfer function matrices (formed according to equations 2.37 and 4.4) were computed in Matlab. The code was run on a Personal Computer with a Pentium IV processor running at 3.8GHz. The matrices had 4096×4096 entries and were generated for λ =632.8nm, $\Delta x = \Delta y = 9\mu$m and $d = 200$m. The matrix formed with equation 2.37 took 8 seconds to complete and used 268.4Mbytes of memory. In contrast, the matrix formed using equation 4.4 took 3.67 seconds and only used 134.2Mbytes of memory.

4.2 Error Analysis

As with any optical system, DHI may be affected by optical aberrations resulting in a reduction of resolution and overall quality of the reconstructed image. As opposed to most imaging systems, such as the microscope, DHI typically presents a lesser degree of monochromatic aberrations as most set-ups are lens-free. However with underwater applications additional sources of error, such as those introduced by glass windows and density variations in the sampled seawater, need to be considered. Some of these optical aberrations can be corrected digitally (by adding additional terms in the reconstruction

algorithm) or compensated in the physical set-up. The main sources of error present in an underwater DHI system are:

- **Refractive index changes.** This is produced by the effective change of medium during the recording and the reconstruction steps. When recording a hologram the object is immersed in seawater which has an approximate refractive index of $n = 1.33$ [112]. The algorithms presented in section 2.3 were derived assuming the reconstruction took place in air with a refractive index of approximate $n = 1$. The mismatch of refractive indices makes the reconstruction of the real image appear at a location different to the location of the original object respective to the CCD as depicted in Figure 4-1. In Figure 4-1 a single point object is located at a distance, d, from the CCD. The recorded hologram can be represented as a diffraction grating or a Fresnel zone plate. Due to the change of refractive indices, it will diffract the rays at a different angle producing aberrations in the reconstruction. In this model, by modifying the wavelength used in the reconstruction algorithm, the error can be compensated. The wavelength used in the reconstruction algorithm needs to be equivalent to the effective wavelength of light in water given by

$$\begin{aligned} n_w \lambda_r &= n_a \lambda, \\ \lambda_r &= \frac{n_a \lambda}{n_w}, \end{aligned} \tag{4.5}$$

  where λ is the wavelength used in recording the hologram; λ_r is the wavelength used in the reconstruction algorithm; n_a is the refractive index of air and n_w is the refractive index of water. For example, a hologram recorded using a He-Ne laser (λ =632.8nm) needs to be reconstructed using wavelength: λ_r =475.78nm. In conventional underwater holography, the aberration compensation suggested by equation 4.5 is more difficult to implement due to limited wavelengths available in commercial lasers.

  When practically implemented, the CCD cannot be in direct contact with the water

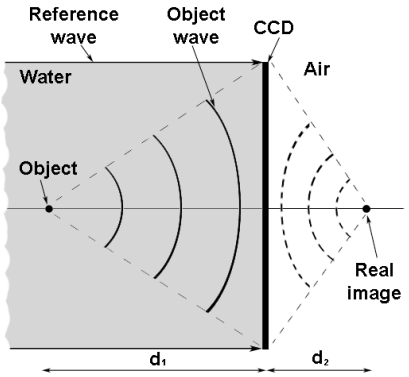

Figure 4-1: Aberration produced by refractive index change.

and therefore the model shown in Figure 4-1 is no longer valid. Typically, a glass window is used to separate the sampled volume from the imaging system, forming an air gap. As explained in [113], the interface water-glass-air introduces several additional aberrations. Figure 4-2 shows the ray trace done for a point object centered in the optical axis. The refraction produced at each interface changes the effective incidence angle of the ray at the hologram plane. The object wave recorded by the CCD appears to be emerging from an apparent object located in front of the original object.

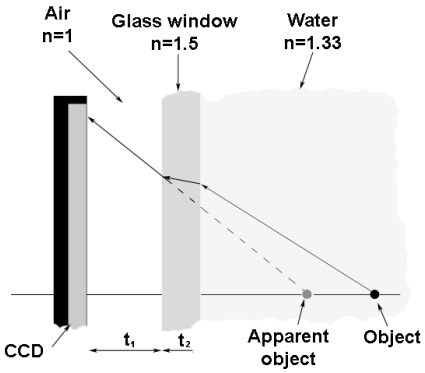

Figure 4-2: Refraction from a ray emerging from a point source in seawater.

For an on-axis point source, the compound interface (water-glass-air) produces a spherical aberration [114]. This aberration can be seen by retracing a number of the refracted rays to their apparent source as shown in Figure 4-3. For a point located off-axis, the reconstructed image exhibits additional aberrations such as astigmatism, coma and field curvature [113]. As explained by Kilpatrick, [115], the spherical aberrations for an on-axis object can be eliminated and the additional aberrations for an off-axis object, primarily astigmatism, are minimized if the thicknesses of the glass window and the air gap are selected properly.

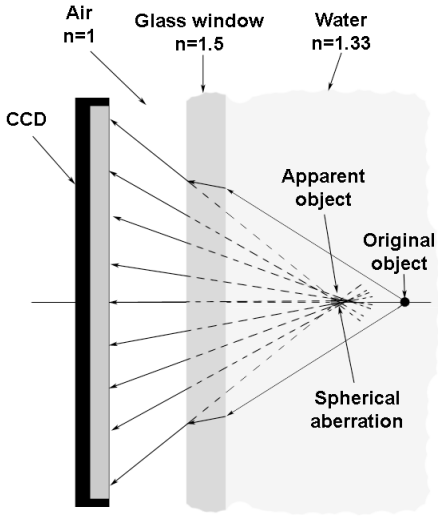

Figure 4-3: Spherical aberration produced by an on-axis point object.

- **CCD misalignment.** Misalignment of the CCD in the recording set-up is an important contributor to error in the reconstruction. In an in-line configuration, the reference wave is assumed to be incident perpendicular to the CCD. In the reconstruction algorithm, a plane wave parallel to the optical axis is used to illuminate the hologram in order to reconstruct the real image. A misalignment of the CCD causes a mismatch between the reference wave used in the recording and reconstruction steps and the field diffracted by the object appears distorted at the

hologram plane. The misalignment of the CCD degrades the quality of the reconstructed image. This can be seen when examining a hologram of a 1951 USAF resolution target located at $d = 315.9$mm from the CCD, recorded with the configuration shown in Figure 3-5 in section 3.2. In the first experiment, the CCD was correctly aligned respective to the incident reference wave. Figure 4-4 shows the reconstruction of the hologram conducted using the convolution approach. In the reconstruction of Figure 4-4, features as small as 44μm can be easily resolved. In the second experiment, the hologram was recorded with the CCD tilted approximately 11.3 degrees respective to the optical axis. The reconstruction of this hologram is shown in Figure 4-5. From this figure, it is evident that the misalignment resulted in a significant degradation of the quality of the reconstruction where no features smaller than 500μm can be resolved.

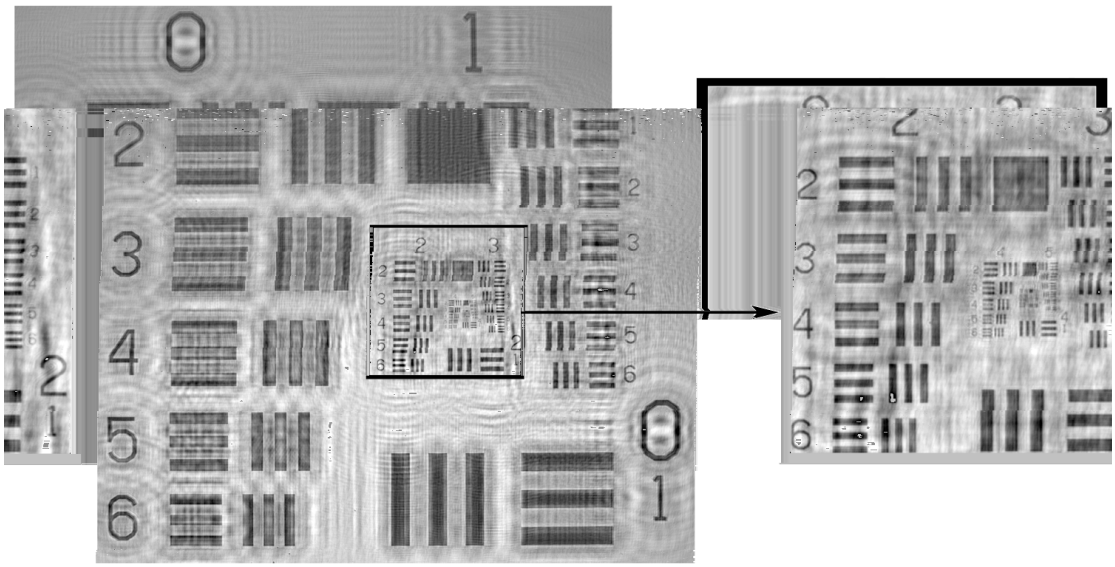

Figure 4-4: Reconstruction of a resolution target at $d = 315.9$mm with the CCD properly aligned.

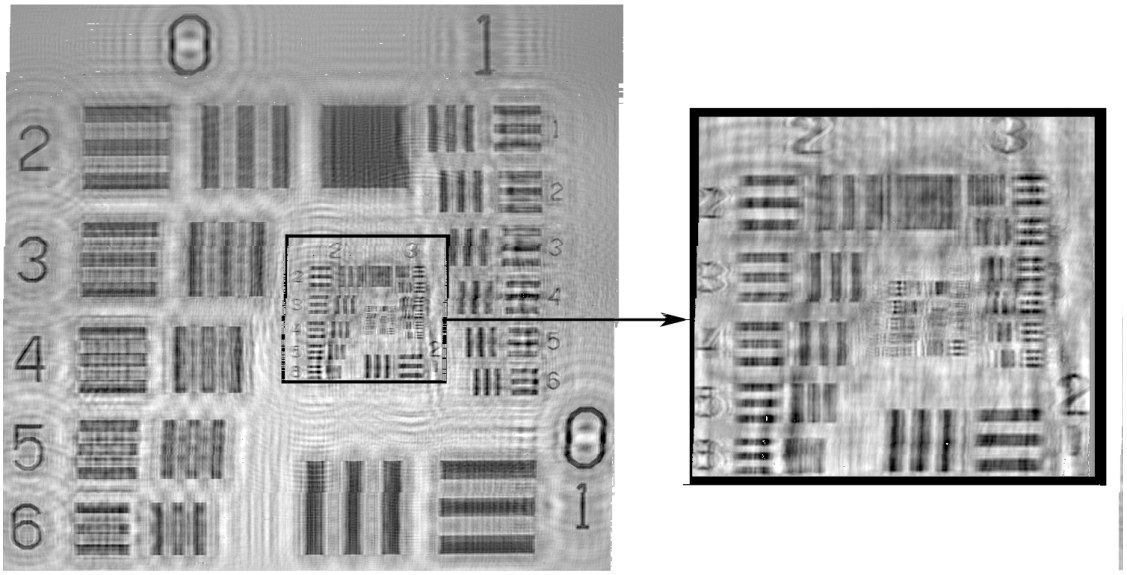

Figure 4-5: Reconstruction of a resolution target at $d = 315.9$mm with the CCD misaligned.

- **Speckle noise.** This is introduced by the nature of the coherent illumination used in DHI. The speckle phenomenon is aperture dependent. As the aperture of the imaging system increases, the speckle noise is reduced. For a detailed description of the effect of speckle noise in in-line and off-axis particle holography refer to [116] and [117].

- **Background noise.** This category includes errors in the measurement produced by intensity variations in the image, dirt in the reference beam, uneven illumination, and formation of interference patterns due to multiple reflections or stray light.

4.3 Power analysis

Adequate selection of the illuminating source is crucial when designing an underwater DHI system. Digital holography uses coherent illumination and therefore a laser source

needs to be used. Specifications of the laser have to be considered including: wavelength, coherence length, stability, beam diameter, laser size and power. With underwater applications, additional parameters also need to be taken into account, such as absorption of light in seawater, and scattering of the sampled object. In addition, the photosensitivity of the sampled aquatic animal has to be considered if its behavior is to be mapped.

The wavelength selection is guided by the characteristic response to light of the CCD used to record the hologram. Ideally, the full dynamic-range of the CCD should be utilized and thus, the laser power has to be properly scaled. The energy consumption of the laser needs to be considered, as it will be running on batteries. In the final implementation, the size of the laser is constrained by the space available in the autonomous underwater vehicle (AUV) carrying the imaging system. The laser needs to be capable of pulsing to avoid the blur produced by the motion of the object. The goal of this section is to conduct a power analysis in order to select the most suitable laser for the underwater DHI system.

4.3.1 Absorption of Light in Seawater

In order to select the wavelength used to record the hologram, the absorption of light in seawater has to be considered. Figure 4-6 shows the absorption coefficients for visible light in seawater. As reported in [118], the water samples were taken from the Gulf of Mexico and the integrated cavity absorption meter (ICAM) was used to measure the optical absorption in the visible range. The discrete absorption coefficients were interpolated using the spline function in Matlab. As shown in Figure 4-6, the peak transmission in seawater ranges from 400nm to 500nm. This suggests that using a blue laser increases the imaging distance. However, it has been found that plankton is disturbed when exposed to light in this range and therefore, its true behavior cannot be measured [119], [120], [121].

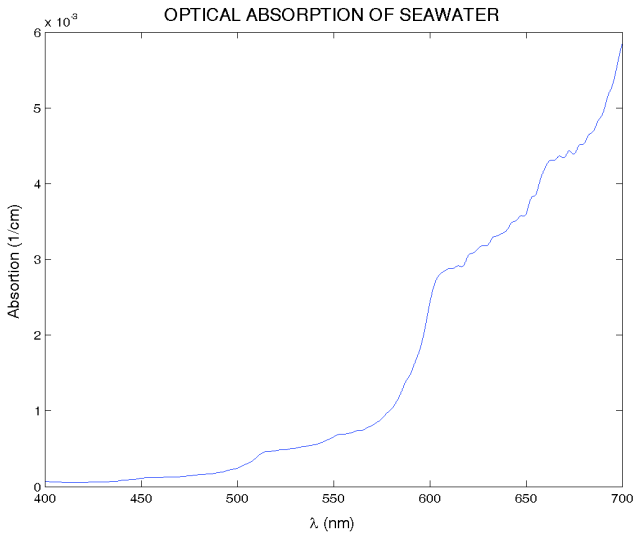

Figure 4-6: Optical absorption in seawater.

The optical power as light propagates through the volume of seawater decays exponentially as function of wavelength and propagation distance according to Beer's law:

$$P_{out} = P_{in} \cdot \exp[-\alpha d], \tag{4.6}$$

where α is the absorption coefficient; λ is the wavelength of the laser source; and d is the propagation distance. Figure 4-7 shows the output power as a function of distance propagated in a volume of seawater. The input power is set to 100mWatts and the output power is computed using equation 4.6 for wavelengths ranging from 400nm to 700nm with steps of 20nm. As seen in Figure 4-7, light at 700nm suffers the most significant absorption.

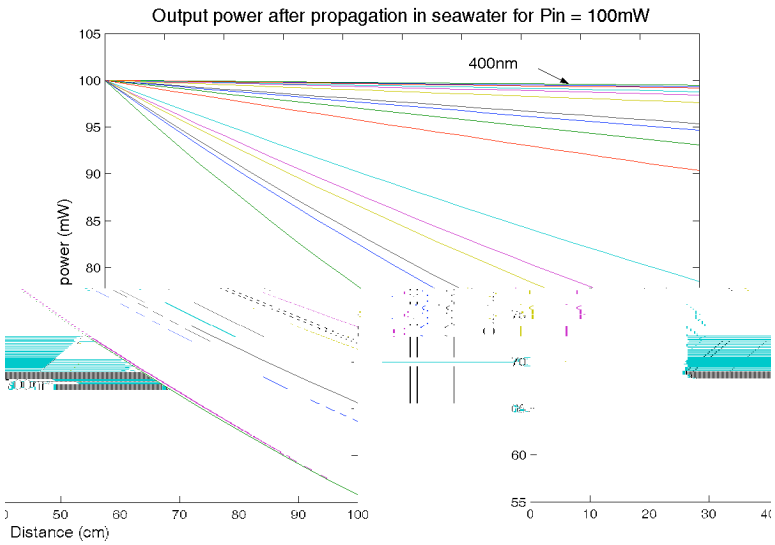

Figure 4-7: Output power after propagation in seawater: Pin=10mW.

4.3.2 Quantum Efficiency of the Detector

The quantum efficiency is defined as the percentage of photons incident on the CCD that will produce an electron hole-pair:

$$QE(\lambda) = \frac{\text{Electrons/pixel/ sec}}{\text{Photons/pixel/ sec}} * 100. \tag{4.7}$$

As with all experiments discussed in this thesis, a Kodak KAF-16801E CCD is used in the models. The quantum efficiency of this CCD is shown in Figure 4-8. As shown in this plot, the CCD performs more efficiently for wavelengths around 650nm.

4.3.3 Scattering Analysis

Figure 2-6 in section 2.2.3 shows a simple scattering model for a copepod. In a real-life application, the scattering model becomes more complex as several additional parameters

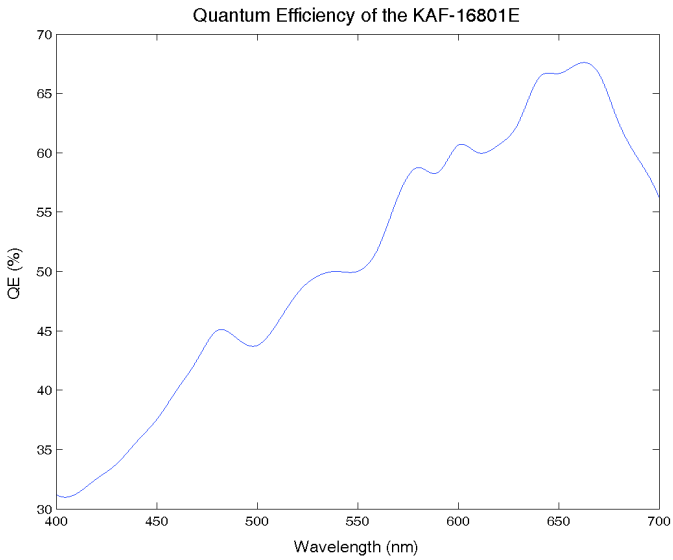

Figure 4-8: Quantum efficiency of the Kodak KAF-16801E CCD.

need to be considered. Such parameters include: orientation, size and absorbance of the copepod; multi-scattering produced by adjacent copepods; light source extinction when propagating through the medium; polarization and frequency change of the scattered light; and re-radiation of the absorbed light via fluorescence or Raman scattering. Several models have been developed to estimate the volume scattering function (VSF), ranging from Monte Carlo simulations [19], where each photon is monitored, to those that use semi-analytic formulations [122]. Despite the few experimental measurements of the VSF, several parameterizations still exist, [123], [124], [125], [126], [127], that when used in underwater models, [128], [129], have produced reasonable results. A global ocean optics database is now available through the Internet (http://wood.jhuapl.edu/) where many observations about absorption and scattering measured in different parts of the world can be used to predict the quality of underwater images.

An experiment was conducted to measure the power loss produced by the scattering of brine shrimp when illuminated with a Helium-Neon laser (λ=632.8nm). The laser beam

was spatially filtered, collimated and expanded to a diameter of 25mm. The expanded beam illuminated a tank with brine shrimp swimming in seawater with a specific gravity of 1.0205. The $15 \times 10 \times 10$cm tank was made from borosilicate glass with a broadband ARC-B antireflection coating. After propagating through the sample the laser beam was detected with a power meter. In all the experiments, the input power (power of the beam before entering the volume of water) was: $P_{in} = 1.95\mu$W. In the initial experiment a volume of 49ml was sampled. The output power (power of the beam after propagating through the volume of water) measured without brine shrimp wa

4.3.4 Required Power Estimation

In order to assure the full-usage of the dynamic range, the minimum required laser power is estimated relative to the saturation signal of the CCD. For the CCD KAF-16801E, the nominal saturation signal is 100,000electrons/pixel. The minimum required power is given by

$$P_{req} = \frac{E_{photon} \cdot N_{sat} \cdot N_{pix}}{QE \cdot F \cdot T_i} e^{\alpha d}, \tag{4.8}$$

where N_{sat} is the saturation signal of the CCD in $electrons/pixel$; N_{pix} is the total number of pixels in the CCD; T_i is the integration time of the CCD (typically controlled by a mechanical or digital shutter or by the strobe of a pulse laser); E_{photon} is energy of a photon given by

$$E_{photon} = \frac{h \cdot c}{\lambda}, \tag{4.9}$$

where h is the Planck's constant ($h = 6.62 \times 10^{-34} J\,\mathrm{sec}$) and c is the speed of light in vacuum ($c = 3 \times 10^8$m/sec).

Figure 4-9 shows the minimum required laser power computed as a function of distance for several wavelengths ranging from 400 to 700nm with steps of 20nm. In this Figure, the integration time was set to 10μsec and the safety factor to 0.7. The required power is computed for the CCD, which has 4096×4096 pixels. From Figure 4-9 it is evident that green light at $\sim$400nm requires the highest power. Although light at 400nm typically has good transmission in seawater, the quantum efficiency of the CCD at this wavelength is very poor.

The optimum wavelength is a function of the propagating distance in seawater. If the propagation distance is very small, the quantum efficiency of the CCD dominates the calculation, setting the optimum around 650nm. As shown in Figure 4-10, when the propagation distance increases, the absorption coefficient dominates, setting the optimum wavelength to approximately 500nm. Figure 4-10 is computed using the same parameters

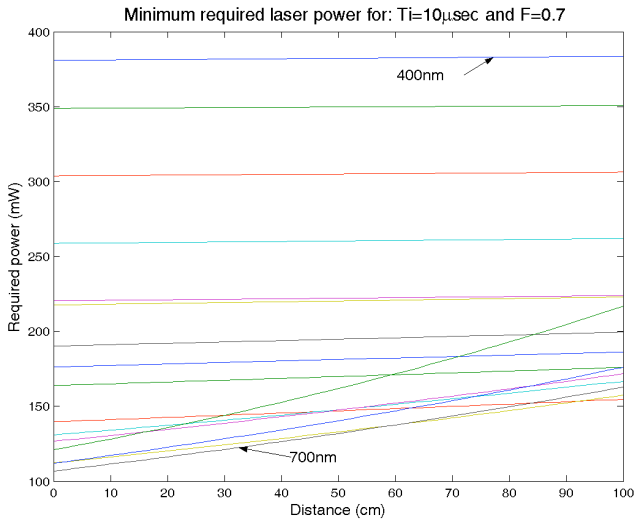

Figure 4-9: Minimum required laser power as a function of distance.

and with a propagation distance in the range of [0,100cm] with steps of 10cm.

The chosen integration time sets the maximum allowable object velocity. If the set integration time is very long, a low power laser is required tolerating low object velocity. In contrast, if the set integration time is very short, a high power laser is required and the object can move at high speeds without producing any motion blur. Two examples of the minimum required power as function of integration time are shown in Figures 4-11 and 4-12. These examples were carried out for $d = 20$cm, $F = 0.7$ and λ in the range of [400nm, 700nm] with steps of 20nm.

4.3.5 Number of Bits used in the Digitization Process

The CCD is connected to a circuit board where the detected signal is digitized. The digitization takes place in an analog/digital converter in which the signal is divided into

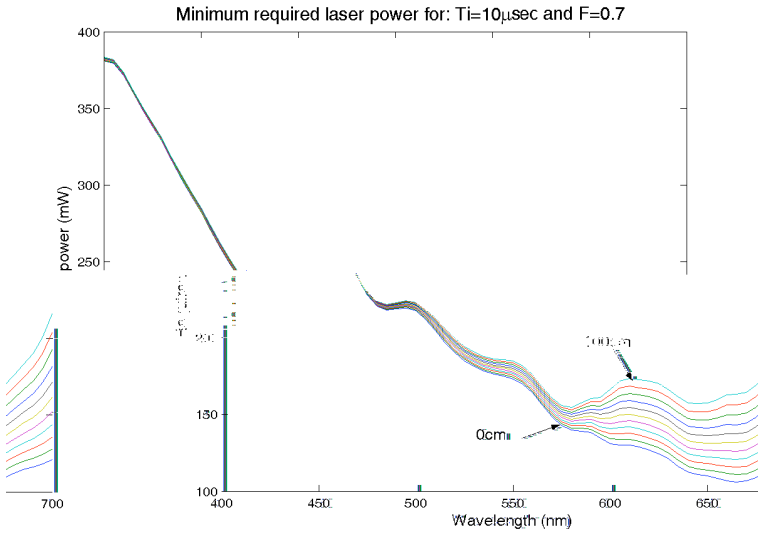

Figure 4-10: Minimum required laser power as a function of wavelength.

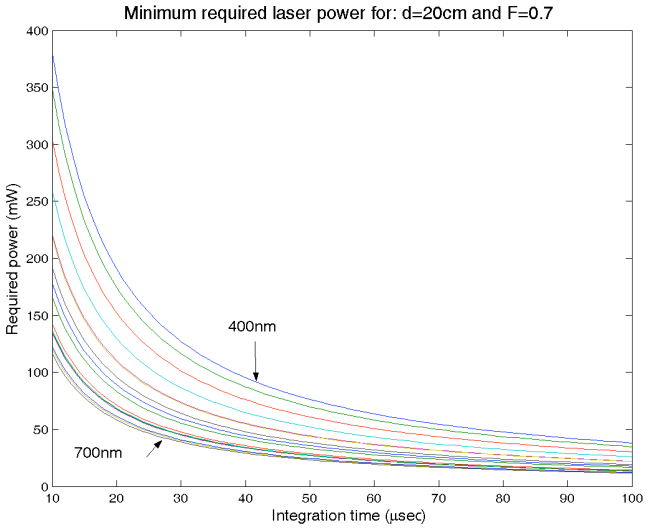

Figure 4-11: Minimum required laser power for T_i in the range [10μ sec,100μ sec].

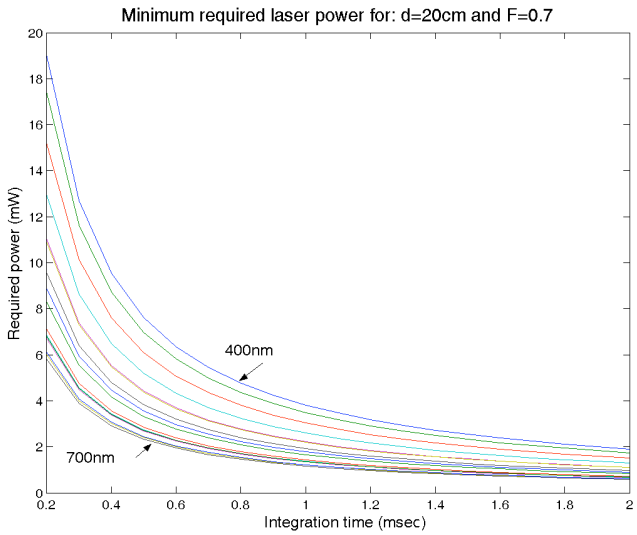

Figure 4-12: Minimum required laser power for T_i in the range [0.2msec,2msec].

several levels with certain accuracy. The CCD is connected to the Kodak S11 evaluation board that converts the electrical signal to a digital form with 12bits of precision. If the laser power is set to use the full dynamic range of the CCD, the 12bits (4096 gray levels) are used to characterize the incoming optical field. Figure 4-13 shows the computed number of bits as a function of the laser power for: $d = 20$cm, $T_i = 10\mu$sec and $F = 0.7$.

Figure 4-14 shows the computed number of bits as function of the distance propagated in seawater using an 80mW laser. Figure 4-15 shows the computed number of bits as a function of the integration time for an 80mW laser.

4.3.6 Laser Selection

From the power analysis derived above, the selected illumination source is a single-mode diode laser with specifications outlined in table 4.1.

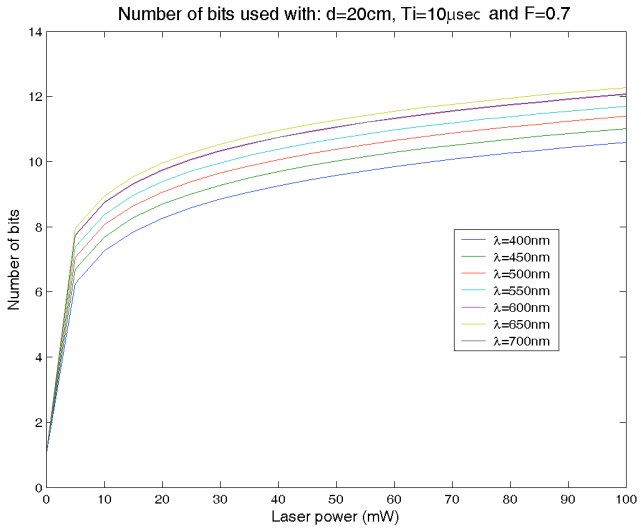

Figure 4-13: Number of bits versus laser power.

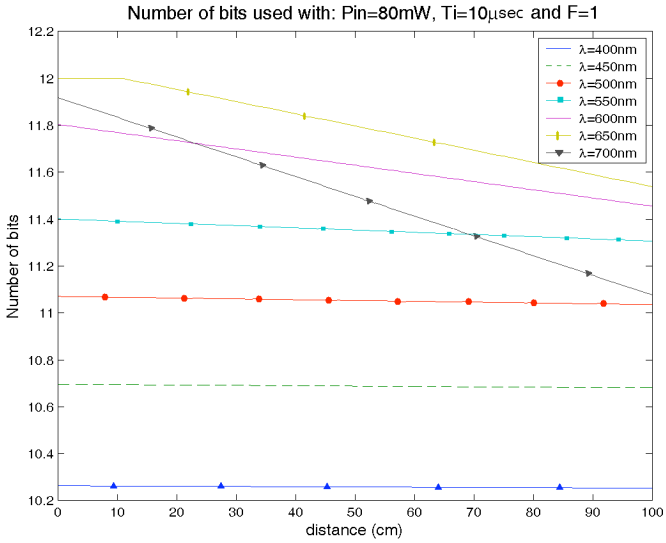

Figure 4-14: Number of bits versus propagation distance.

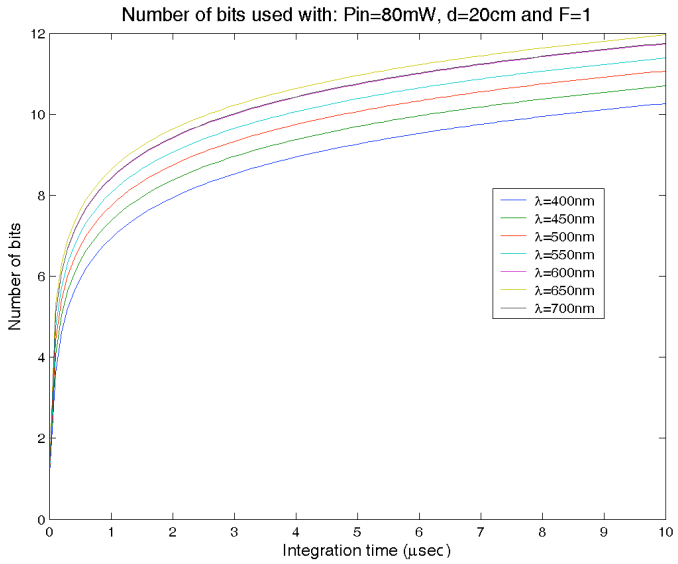

Figure 4-15: Number of bits versus integration time.

Table 4.1: Specifications of the selected diode laser.

Manufacturer	Power Technology, Inc.
Model	PPMT(658-80B)
Wavelength	658nm
Wavelength tolerance	652-662nm
Power	80mW
Mode	Single-cavity mode
Current	120mA
Controls	Thermoelectric control Current control
Optics	Aspherical lens
Modulation Signal	External TTL
Modulation Frequency Range	CW-20MHz
Dimensions	Diameter: 38mm; Length: 144mm
Operating Voltage	12VDC

Overall, this diode laser represents the optimum commercially available laser for an underwater DHI system. Operating at a wavelength that does not disturb plankton, a true behavior can be mapped and the power is also optimized. In addition, the diode laser can be pulsed by means of an external TTL signal. The modulation can be controlled from a continuous operation to single pulses of 50ns. The inboard temperature and current controllers produce a stable output that improves its coherence length. By including an aspherical lens, the elliptical beam that exits the diode laser is converted to the standard circular beam, facilitating the full coverage (after expansion) of the photosensitive area of the CCD. The reduced size of the diode laser allows the fabrication of a compact underwater DHI system that can be carried by an AUV.

4.4 CCD Selection

In digital holography, the selection of the CCD used to record the hologram is a crucial step usually determined by the application type. The selected CCD has to fulfill the requirements imposed by the sampling theorem as discussed in section 3.1. The most important aspects to consider in the selection of a CCD for an underwear application are:

- **High space-bandwidth product.** A large number of pixels and a small pixel size are desired. The numerical reconstruction of holograms requires a pixel number that is a power of 2, such as 4096×4096 and thus pixels arranged in a square grid are advantageous. If the selected CCD pixels are arranged in a rectangular grid, the capture image needs to be zero padded to reach a pixel number equal $2^n \times 2^n$.

- **High sensitivity.** A highly sensitive CCD is needed to reduce the required power of the laser source. The sensitivity is defined as the ratio of the signal to noise ratio (SNR) and the quantum efficiency of the CCD. The sensitivity of a CCD is usually in the range of $10^{-4}\mathrm{J/m^2}$ to $10^{-3}\mathrm{J/m^2}$.

- **Large dynamic range.** As explained in section 4.3.5, it is important to have a large dynamic range to accurately represent the optical field. The dynamic range of the CCDs typically ranges between 8 and 16 bits. The dynamic range is also represented as the log ratio of the saturation signal and the readout noise in decibels.

- **Low noise.** A low level of noise produced by the CCD and the electronic board is desired in order to obtain high quality holograms. The main types of noise in a CCD are: shot noise (produced by the randomness of the photon arrival in the CCD plane also referred to as photon noise), thermal noise (produced by the operation temperature of the CCD also referred to as dark noise or dark signal); and readout noise (produced by the readout electronic circuit board).

The three basic architectures of CCDs are: interline-transfer devices, frame-transfer devices and full-frame transfer devices. The interline-transfer devices are made of light sensitive detectors (photodiodes) arranged in lines spaced by non-sensitive areas that contain storage circuits as shown in Figure 4-16. One disadvantage with these CCDs is they have a reduced fill factor. The fill factor is the active area in one pixel for the conversion of photons. These CCDs can capture images at very high rates; therefore, they are suitable for applications such as particle imaging velocimetry (PIV). The frame-transfer architecture, shown in Figure 4-17, is also composed of different areas for light conversion and for storage. These CCDs shift the capture scene very fast to the storage array, also making them suitable for applications involving

read out the capture scene, especially if the space bandwidth product is high, making it unsuitable for applications such as PIV.

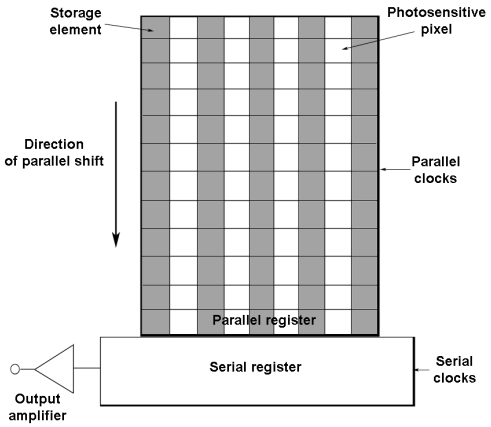

Figure 4-16: Interline-transfer architecture [87].

The CCD selected for our underwater digital holographic camera is the KAF-16801E from Kodak. The specifications of this CCD are listed in table 4.2. The CCD is connected to the Kodak S11 evaluation board. This board has a 12 bits analog/digital converter and an integrated digital shutter. Other parameters, such as optional binning mode, can be selected from the evaluation board. The evaluation board is connected to the frame grabber R3-PCI-DIF from Bitflow. The frame grabber is a PCI digital camera interface that permits the communication between the evaluation board and the computer.

4.5 Motion Analysis

In underwater holographic applications, both the object and the optical system are in motion. The motion may produce undesirable blurring in the recorded holograms, making

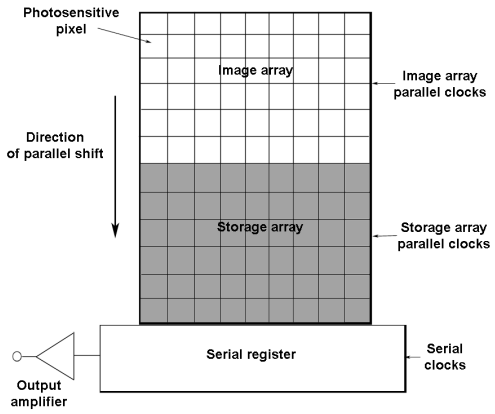

Figure 4-17: Frame-transfer architecture [87].

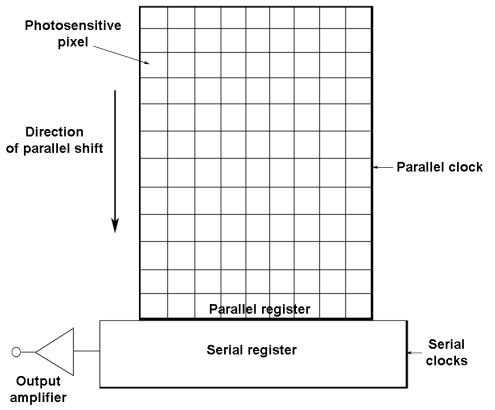

Figure 4-18: Full-frame transfer architecture [87].

Table 4.2: Specification of the Kodak KAF-16801E CCD.

CCD architecture	Full-frame transfer
Vendor	Eastman Kodak Company
Model	KAF-16801E
Number of pixels	4096×4096pixels
Pixel size	9μm
Fill factor	100%
Dynamic range	72dB
Saturation signal	Nominal: 100,000 electrons/pixel
Dark signal	Nominal: 18 electrons/pixel/sec
Noise floor	Nominal: 15 electrons
Output sensitivity	12μV/electron

them unusable to reconstruct the real image. Motion deblurring techniques are difficult to implement since the object is changing shape while swimming and the blurring function is not accurately known [131]. Blind deconvolution algorithms can be implemented to try to estimate the blurring function, however a high quality result is still not achieved. In addition, these techniques take a considerable time to compute, making them unsuitable for in situ detection of underwater species. An experimentally verified criterion proposed by [132] aims to restrict the allowable motion to less than one tenth of the minimum required fringe spacing of the smallest object. For in-line holograms, the motion must be less than one tenth of the object's dimension [42].

One method to avoid motion blur in recoded holograms is to set the integration time of the imaging system to the corresponding value. The integration time is the period in which the CCD is exposed to light before flushing the information to the adjacent register, usually controlled by a mechanical or digital shutter. Pulsed lasers can also be used to set the integration time by controlling the width of the pulse. A digital shutter integrated in the evaluation board controls the integration time of the CCD, where values ranging from 10msec to 10sec can be chosen. However, if the integration time is set too low, the readout noise increases, producing undesirable artifacts in the captured image. In order to minimize these undesirable artifacts, an external device such as a mechanical

shutter or a pulsed diode laser has to be implemented in the experiments to control the integration time of the system. In all experiments presented in this thesis, the digital shutter of the evaluation board was set to 1sec to minimize the artifacts due to the readout noise. In the first set of experiments, a mechanical shutter located behind the laser is synchronized with the camera via a monostable multivibrator circuit to set the integration time to 2msec. In the second set of experiments, the selected diode laser of section 4.3.7 is pulsed to set the integration time to 28.8μsec. The main advantage of using a modulated diode laser instead of a mechanical shutter is that the integration time can be very small, enabling higher levels of motion to be tolerated. In addition, no moving mechanical parts are included that could introduce vibrations in the system.

To estimate the required integration time for experiments in a laboratory, the motion of the object has to be considered. The average swimming velocity of a copepod is 4mm/sec, which corresponds to 444.4 pixels/sec for a pixel size of 9μm [133]. At this velocity, an integration time of 2 msec is sufficient to reduce the motion during exposure to less than 1 pixel. It is usually desirable to set the integration time to a period smaller than 2 msec to avoid motion blur produced by the swimming legs and antennas. However, if the integration time decreases further, the required laser power increases as explained in section 4.3.4. For experiments done with the diode laser modulated with a pulse width of 28.8μ sec, objects moving at a maximum speed of 312.5mm/sec can be recorded without producing motion blur in the holograms. Figures 4-19 and 4-20 show the maximum tolerated velocity as a function of integration time in order to reduce the motion of the system to one pixel (for a pixel size: $\Delta x = 9\mu$m).

For the field experiments, the velocity of the autonomous underwater vehicle (AUV) has to be considered. Typically, AUVs move at an average speed of 2 knots (1m/sec); therefore, requiring an integration time of approximately 10μ sec. The selected modulated diode laser presented in section 4.3.7 can be pulsed to a minimum of 50nsec. Therefore, velocities up to 350knots (180m/sec) can be tolerated. However, if the system were

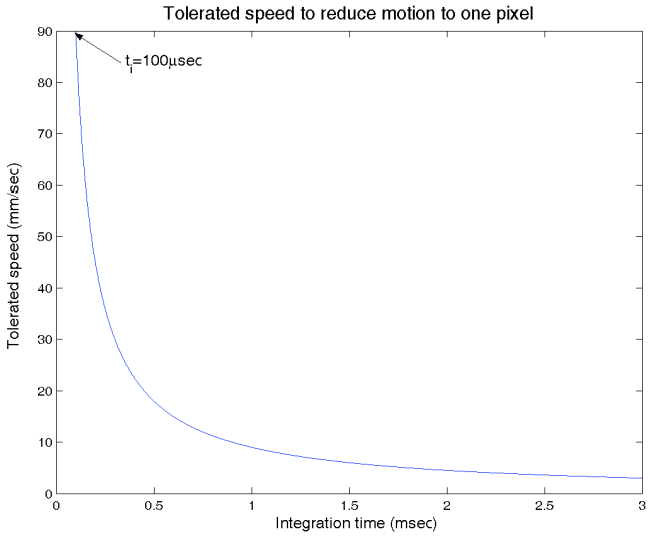

Figure 4-19: Maximum allowable object velocity as function of integration time (T_i): T_i in the range [100μ sec,3msec].

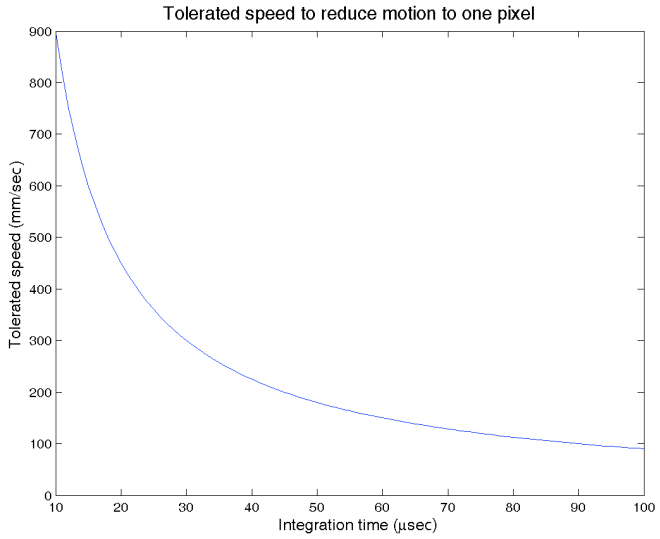

Figure 4-20: Maximum allowable object velocity as function of integration time (T_i): T_i in the range [10μ sec,100μ sec].

operated with this integration time, only 4 bits of the CCD would be used to store the hologram, making the reconstructions very noisy.

4.6 Timing Circuit

A monostable multivibrator circuit was used in the experimental set-up to control the global integration time produced by an external device, such as mechanical shutter or modulated diode laser synchronized with the CCD. This circuit uses the 555 timer to produce accurate time delays. The evaluation board connected to the CCD sends a transistor-transistor logic (TTL) signal that is high during the integration time imposed by the digital shutter. The rise edge of this TTL signal triggers a single pulse produced by the 555 timing circuit when working in monostable mode. A single external resistor and capacitor network controls the pulse width and time delay. The time delay can be calculated from the design equation:

$$\tau = 1.1(R \times C), \tag{4.10}$$

where R is the value of the resistor in Ohms and C is the value of the capacitor in Farads.

The monostable multivibrator circuit used in the experiments is shown in Figure 4-21. Figure 4-22 shows the timing sequence produced by this circuit when synchronized with the CCD. The threshold and trigger levels are normally set to two-thirds of the input voltage. For experiments done with the modulated diode laser, the output signal of the monostable circuit is modified using the inverter circuit SN7404, as the laser operates in a "normally-high mode" and is activated when the signal is low.

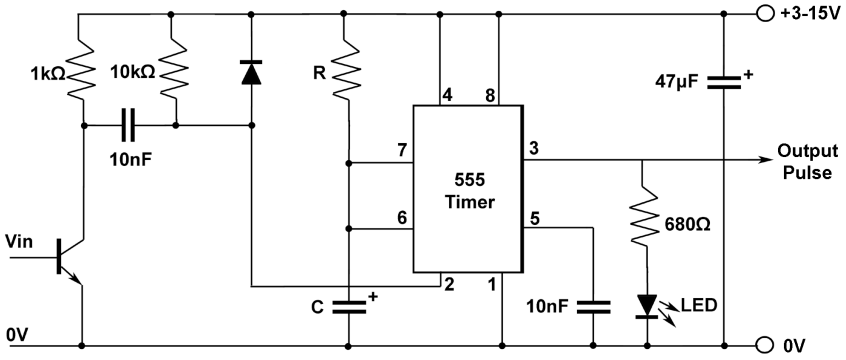

Figure 4-21: Diagram of the monostable multivibrator circuit used in the experimental set-up [134].

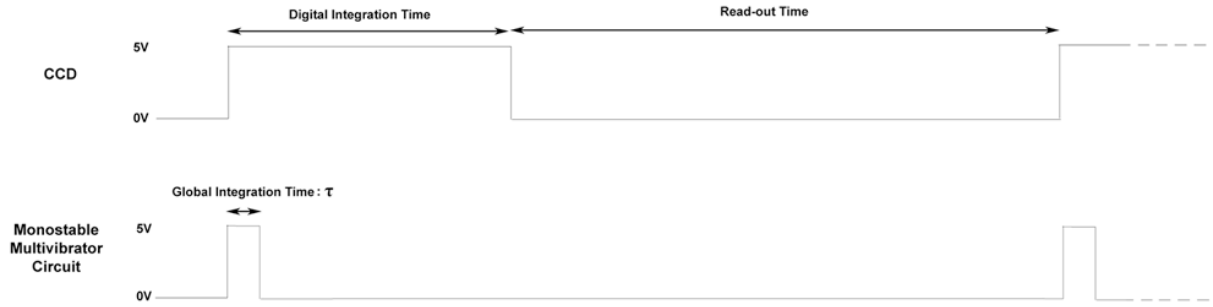

Figure 4-22: Time sequence followed by the CCD and the monostable multivibrator circuit [134].

4.7 Holographic Imaging of Brine Shrimp

In this section, several set-ups used to capture and process digital holograms of brine shrimp will be discussed. Brine shrimp, also known as artemia, are branchiopod crustaceans that live in hypersaline waters. The life cycle of brine shrimp begins from a dormant cyst with a diameter of 200μm that contains an embryo in a suspended state of metabolism. Changes in temperature, water and salinity cause the cyst to rehydrate and open to release the nauplius larva. The nauplius larva remains in this first growth stage for approximately 12 hours depending on the environmental conditions. After this initial growth stage, the lava molts about 15 times before reaching an adult size of about 10mm in length. In a laboratory brine shrimp are kept alive in a tank filled with seawater, made by mixing spring water with a sea salt concentration such as Instant Ocean ®. A hydrometer Coralife Deep Six ® is used to control the levels of salinity in the water. For brine shrimp, the salinity is usually set around 27 to 37 PPT or to a specific gravity ranging from 1.020 to 1.023. The oxygen in the water is supplied by an air pump connected through a thin tube to an air stone positioned one inch away from the bottom-corner of the tank. Brine shrimp are fed periodically (about every three days) with Phyto-Feast Live, which is a concentration of live marine microalgae. Under these conditions, brine shrimp can live up to 3 weeks. Brine shrimp can be purchased commercially throughout the US or via the Internet and are typically used for feeding other fish species.

Figure 4-23 shows the set-up used for the first set of experiments conducted to image brine shrimp. This set-up is similar to the in-line single-beam configuration shown in Figure 2-7 section 2.2.3. The illumination source consists of a 25mW Helium-Neon laser (λ = 632.8nm) with a beam diameter and divergence of 0.98mm and 0.82mrad respectively. Located next to the laser, a LS6 Uniblitz mechanical shutter sets the global integration time to T_i=2msec. A VMM-D4 Uniblitz shutter driver is synchronized with the CCD via a monostable multivibrator circuit as discussed section 4.6. The rotation of the polarizer plate located behind the mechanical shutter controls the brightness of

the illumination. The laser beam is spatially filtered by the combination of a 20X microscope objective and a 15μm pinhole located on a three-axis positioning mount. The point source produced by the pinhole generates a spherical wave that propagates towards a lens where the collimation takes place. The collimating lens is plano-convex and has aperture and focal lengths of 25.4mm and 500mm respectively. The iris located between the spatial filter and the collimating lens blocks the high-spatial frequency components of the spherical wave. However, the lens holder sets the aperture of the system, limiting the diameter of the collimated beam to 19mm. The plane wave produced after collimation illuminates approximately 28.4ml of seawater. Made of borosilicate glass, the tank is coated on both sides by an ARC-B broadband antireflection coating and it is filled with seawater and free-swimming brine shrimp. The second iris blocks stray light, such as the light passing through the screw holes of the lens holder. The CCD KAF-16801E records the hologram produced by the interference between the diffracted and undiffracted light after propagating through the tank. It is important to note that in this set-up only a small portion of the CCD (around 2 Mega pixels) is used to record the hologram. The CCD is connected to an evaluation board, which communicates with a Pentium III personal computer via the frame grabber R3-PCI-DIF, as explained in section 4.4. The R2View software from Bitflow is used to capture the holograms. The holograms are stored in Bitmap (bmp) format. All holograms presented in this thesis are reconstructed using Matlab on a Pentium IV, 3.8GHz, personal computer. A case made of acrylic is used to protect the set-up from additional vibrations, such as those introduced by airflows.

A typical hologram of a brine shrimp recorded by the set-up discussed above is shown in Figure 4-24. As can be seen, the hologram consists of a set of bright and dark fringes.

Figures 4-25, 4-26 and 4-27 show sample reconstructions of brine shrimp using the convolution approach with the paraxial-approximated kernel for different imaging distances.

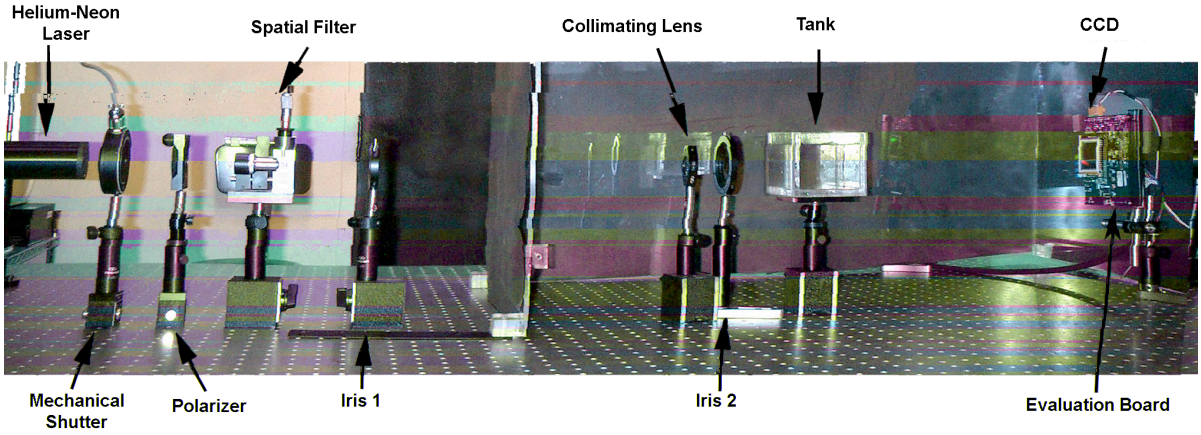

Figure 4-23: In-line single-beam experimental set-up using a Helium-Neon laser.

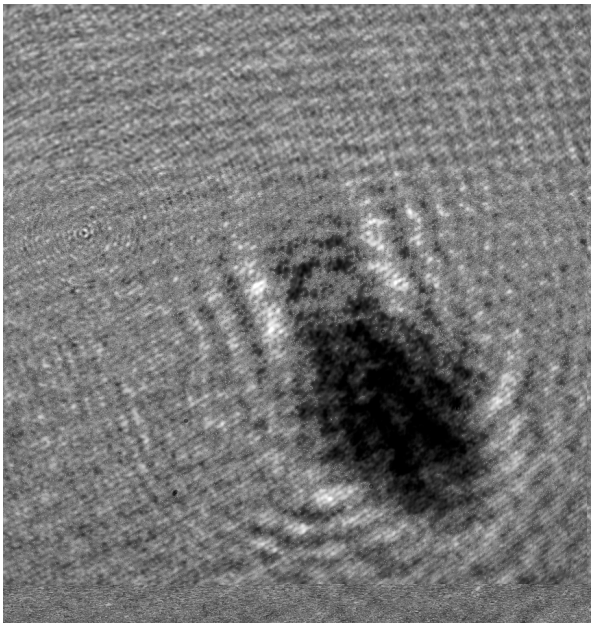

Figure 4-24: Hologram of a brine shrimp recorded using a He-Ne laser in an in-line configuration.

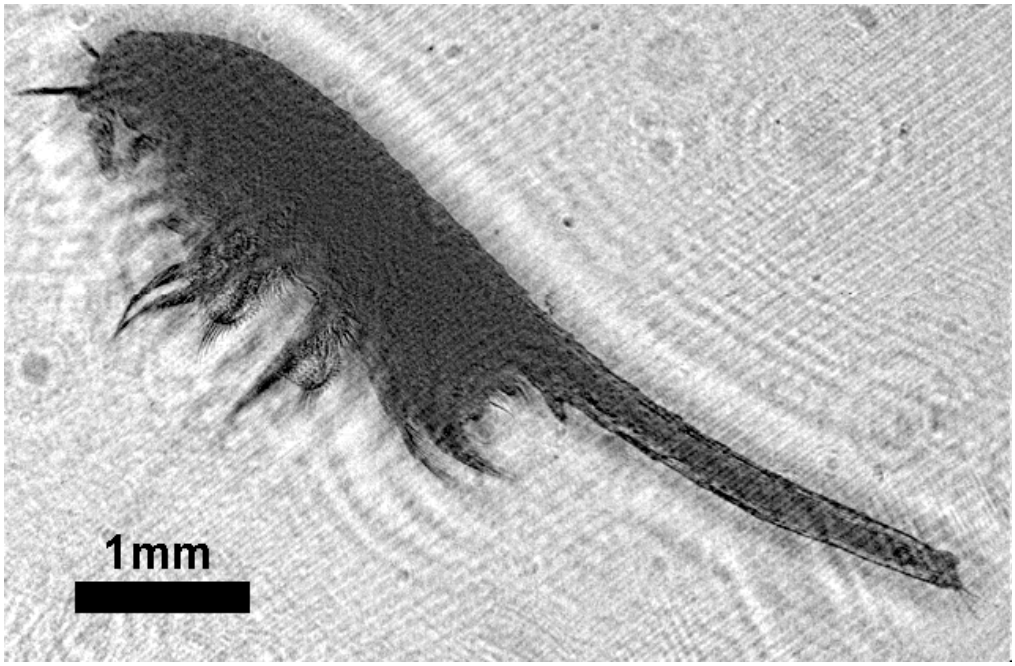

Figure 4-25: Reconstruction of a brine shrimp located 68mm from the CCD.

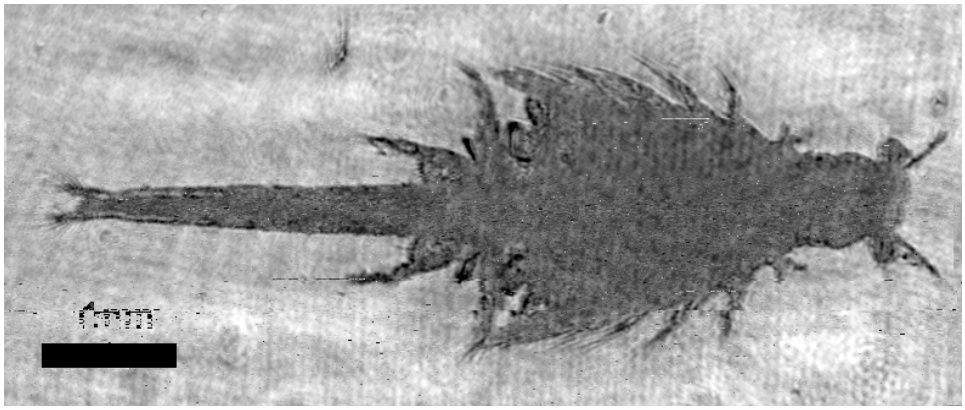

Figure 4-26: Reconstruction of a brine shrimp located 444mm from the CCD.

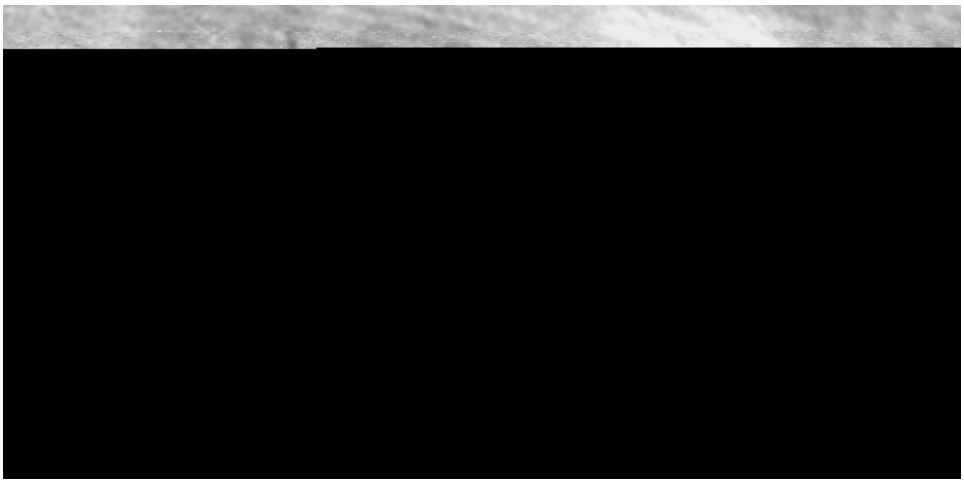

Figure 4-27: Reconstruction of a brine shrimp located 932mm from the CCD.

The brine shrimp in Figure 4-25 was reconstructed with $d = 68$mm, according to equation 2.19 of section 2.2.1. At this relatively short imaging distance, a high level of detail of the brine shrimp is resolved in the reconstruction. Features such as thin hairs of approximately 9 microns in the swimming appendages can be discerned. The ripples in the reconstruction that surround the brine shrimp are mainly due to the diffraction effect at sharp edges produced by the out-of-focus virtual image. Ripples of concentric rings, creating an "Airy pattern", are produced by particles suspended in the medium located at an out-of-focus plane or by dust in the optical elements. The ripples oriented at an angle of about 45 degrees are produced by multiple reflections at the glass-water-glass interface. The halo and the undiffracted portion of the reference wave that contributes to the uniform background introduce additional aberrations. This reconstruction is a raw image and no additional post-processing has been carried out at this point.

The brine shrimp in Figure 4-26 was reconstructed with $d = 444$mm. At this relatively long imaging distance, two major effects occur in the reconstruction. The first effect is that some of the smaller features are no longer resolvable and appear blurred. This is due to a low-pass filtering effect that occurs when the high-spatial frequency components

of the object wave miss the hologram aperture. The second effect during reconstruction is the reduction of aberrations introduced by ripples in the background as the virtual image is highly out-of-focus and only provides a uniform blur.

The reconstruction of Figure 4-27 was done with $d = 932$mm. At this long imaging distance, the brine shrimp presents a uniform blur produced by the same low-pass filtering effect. Even at this distance, sufficient detail remains to permit a clear morphological characterization of the brine shrimp.

The reconstructions shown above have a mild level of motion blur produced by the fast movement of the swimming and feeding appendages. The average swimming speed of an adult brine shrimp is 9.9mm/sec or 1,100pixels/sec [135]. If the integration time is set to 2msec, the motion of the object will only be reduced to 2.2pixels producing a mild level of motion blur in the reconstruction. The level of the motion blur is increased if the global integration time of the system is not set properly, as shown in Figure 4-28.

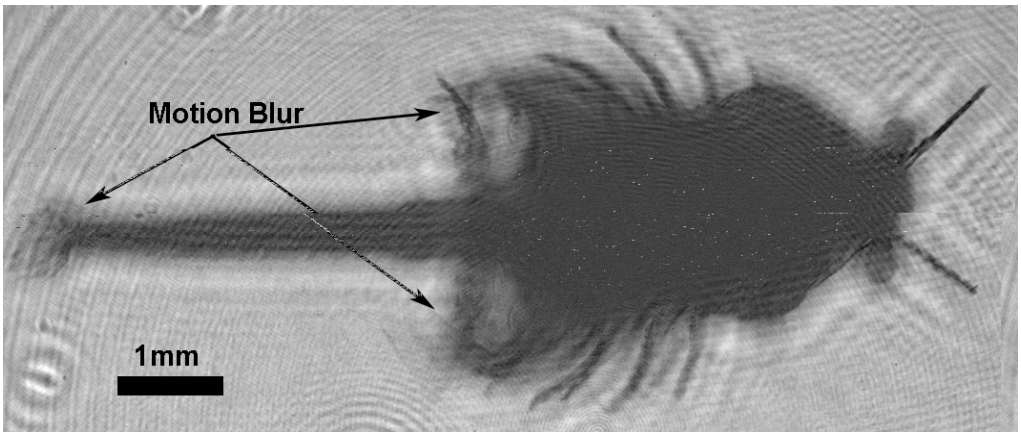

Figure 4-28: Reconstruction of a brine shrimp at d=68.9mm presenting a mild level of motion blur.

The second set of experiments to characterize brine shrimp was conducted using the set-up of Figure 4-29. Two major modifications were introduced in this set-up which

were not present in Figure 4-23. The first modification relates to the spatial filter, which is now composed of a 60X microscope objective and a 5μm pinhole. This spatial filter produces a spherical wave with a higher divergence angle, forming an expanded beam with a larger diameter. The second modification was the introduction of a collimating lens of 75mm in diameter and a focal length of 150mm. The collimated beam illuminates 135.4ml of seawater covering the entire photosensitive area of the CCD.

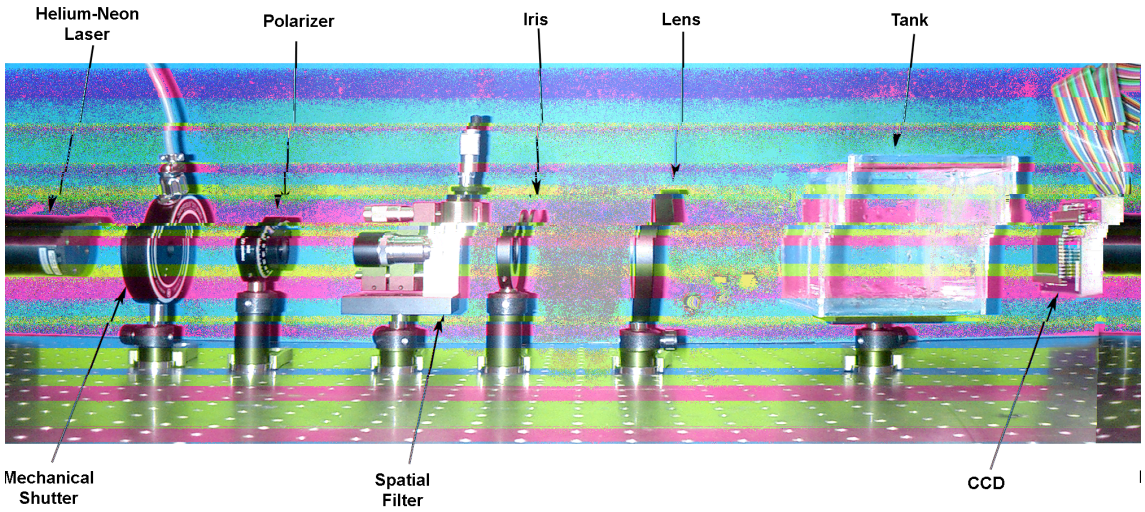

Figure 4-29: In-line single-beam experimental set-up using a Helium-Neon laser: full coverage of the CCD.

Reconstructions of two holograms recorded using the set-up of Figure 4-29 are shown in Figures 4-30 and 4-31. In these reconstructions, small features of the brine shrimp are highly resolvable, such as the tail hair. This is due to the full usage of the photosensitive area of the CCD (16 Mega pixels) capturing high-frequency components of the object wave. Figure 4-32 shows a comparison between the tail of a brine shrimp reconstructed using a limited portion of the CCD (similar to the one used in the set-up of Figure 4-23) and the corresponding reconstruction made using the full CCD. From this figure, it is

clear that when the hologram is reconstructed using a small portion of the CCD, the reconstruction presents a uniform blur produced by the low-pass filtering effect.

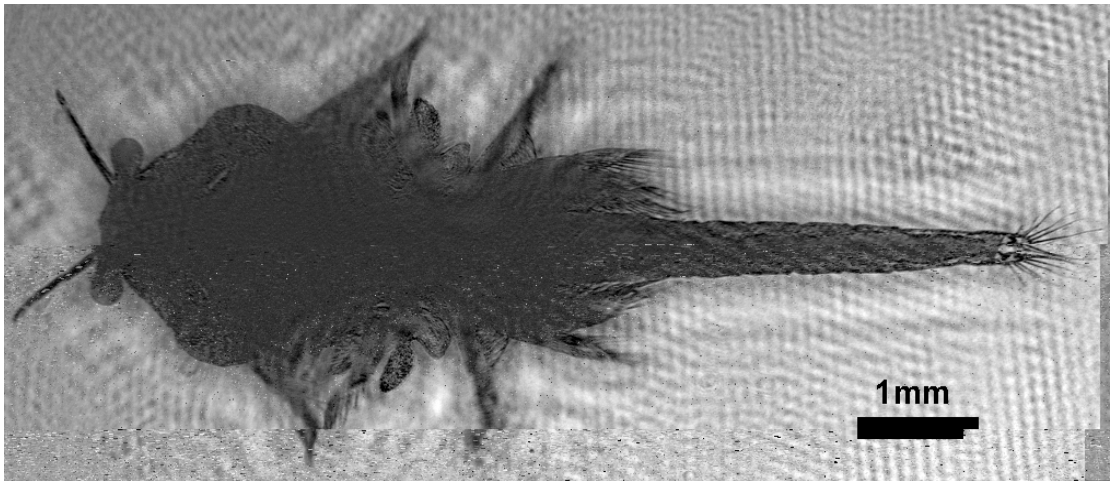

Figure 4-30: Reconstruction of a brine shrimp at d=103.5mm using the entire photosensitive area of the CCD.

The third set of experiments was conducted using the final set-up shown in Figures 4-33 and 4-34. In this set-up, the illumination source consisted of the selected 80mW, 658nm modulated diode laser of section 4.3.7. This diode laser was modulated with a TTL signal generated by the monostable multivibrator circuit in synchronization with the CCD to set the global integration time to 28.8μsec. No mechanical shutter was included in the system as the diode laser was pulsed. For extended integretion periods, the polarizer was required to attenuate the input beam to avoid saturation in the CCD. As the integration time decreases, the effective power received at the CCD decreases and thus the polarizer is no longer needed. The mirror positioned behind the polarizer bent the laser beam 90 degrees to optimize the space occupied by the optical system. Similar to the set-up of Figure 4-29, the spatial filter was composed of a 60X microscope objective and a 5μm pinhole. The collimation lens had a diameter and focal length

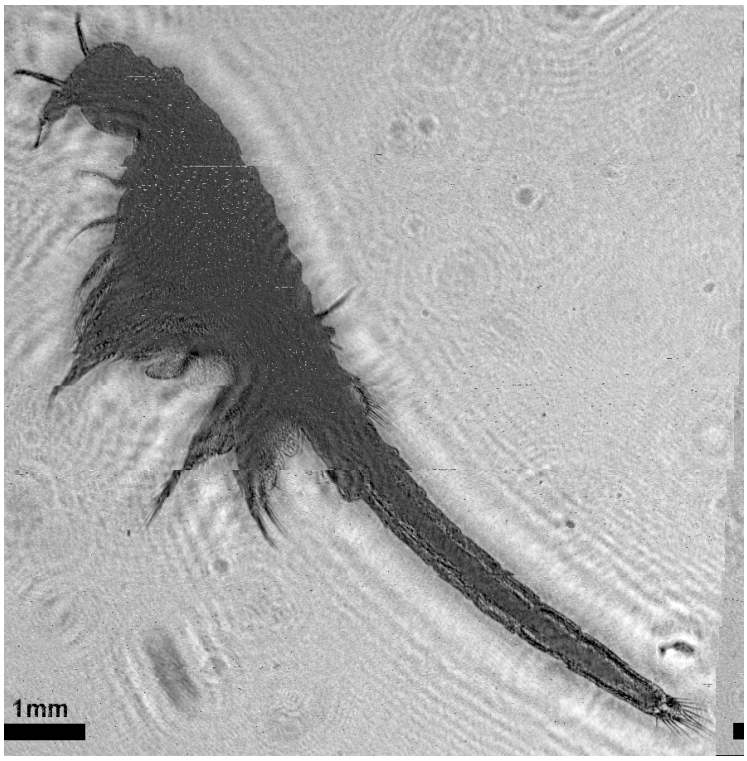

Figure 4-31: Reconstruction of a brine shrimp at d=109mm using the entire photosensitive area of the CCD.

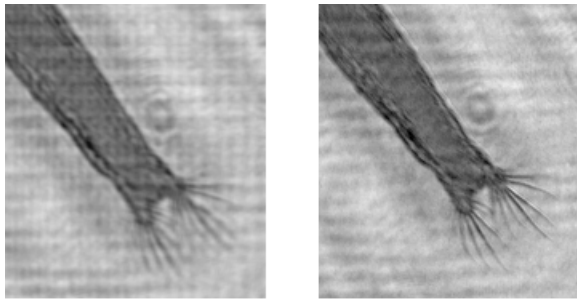

Figure 4-32: Reconstruction of the tail of a brine shrimp at d=162mm: (a) Using a small portion of the CCD to record the hologram; (b) Using the full CCD to record the hologram.

of 75mm and 150mm respectively. The field of view of the system was imposed by the finite size of the CCD (36.86mm × 36.86mm,) allowing 135.4ml of seawater to be sampled. Made of borosilicate glass, the tank was coated on both sides with an ARC-B broadband antireflection coating. The dimensions of the tank were 100×150×100mm. The CCD was connected to the evaluation board, which was then connected to the frame grabber installed on a Pentium III, 1.2GHz mini-computer. The entire holographic imaging system was placed on a 2ft x 1ft breadboard. An umbilical cable that came out of the board was connected to the external power supplies.

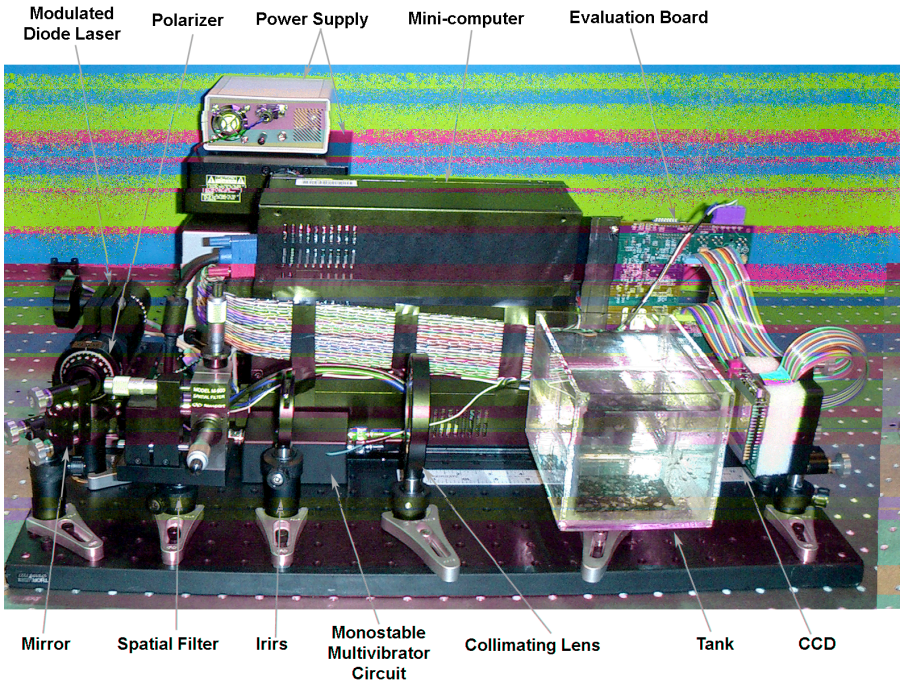

Figure 4-33: Final in-line single-beam experimental set-up using a modulated diode laser.

Figures 4-35 and 4-36 show images of a brine shrimp reconstructed from holograms recorded with the set-up of Figure 4-33. The quality of the reconstructions is very high and small features of the brine shrimp can be resolved, such as thin hairs in the

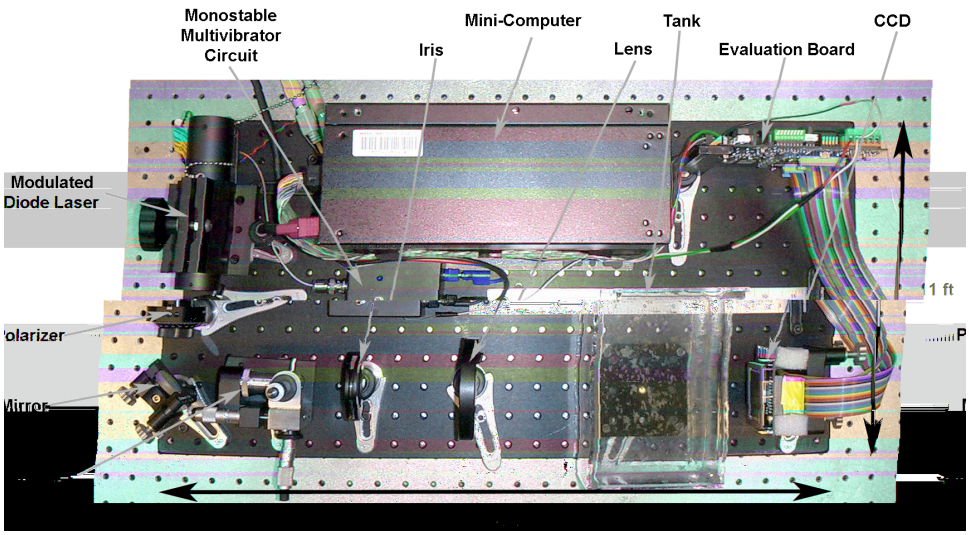

Figure 4-34: Final in-line single-beam experimental set-up using a modulated diode laser: Top view.

swimming and feeding appendages and tail. No motion blur is present in the picture as the integration time of the system is set too low, tolerating objects speeds up to 312.5mm/sec. The change in brightness in the object represents different levels of absorption of the illuminating beam while propagating through the object.

From Figures 4-35 and 4-36, it is evident that some thin hairs of the brine shrimp present a mild level of uniform blur. This blur is produced by a misfocus in the reconstruction and not by the motion of the brine shrimp or vibrations in the system. However, with DHI it is possible to digitally scan or make focus adjustments in the reconstruction. Figure 4-37 shows a brine shrimp reconstructed at d =149mm. Some portions of this brine shrimp are magnified and reconstructed at the distance where they appear to be in focus. This analysis leads to the implementation of a Laplacian-based algorithm to auto-focus the object, discussed in Chapter 5.

The fourth set of experiments was conducted using an in-line Mach-Zehnder setup

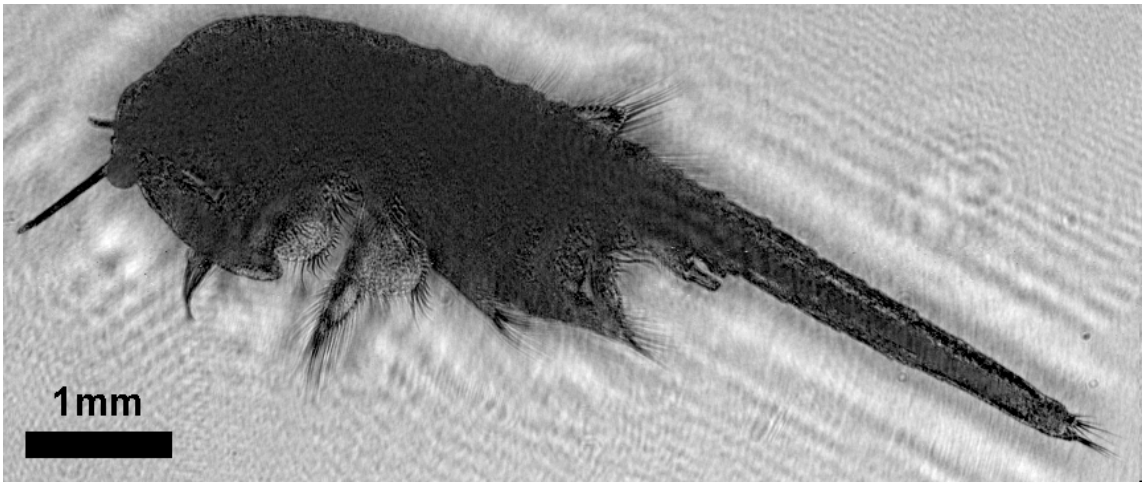

Figure 4-35: Reconstruction of a brine shrimp at d=102mm using the final in-line single-beam experim

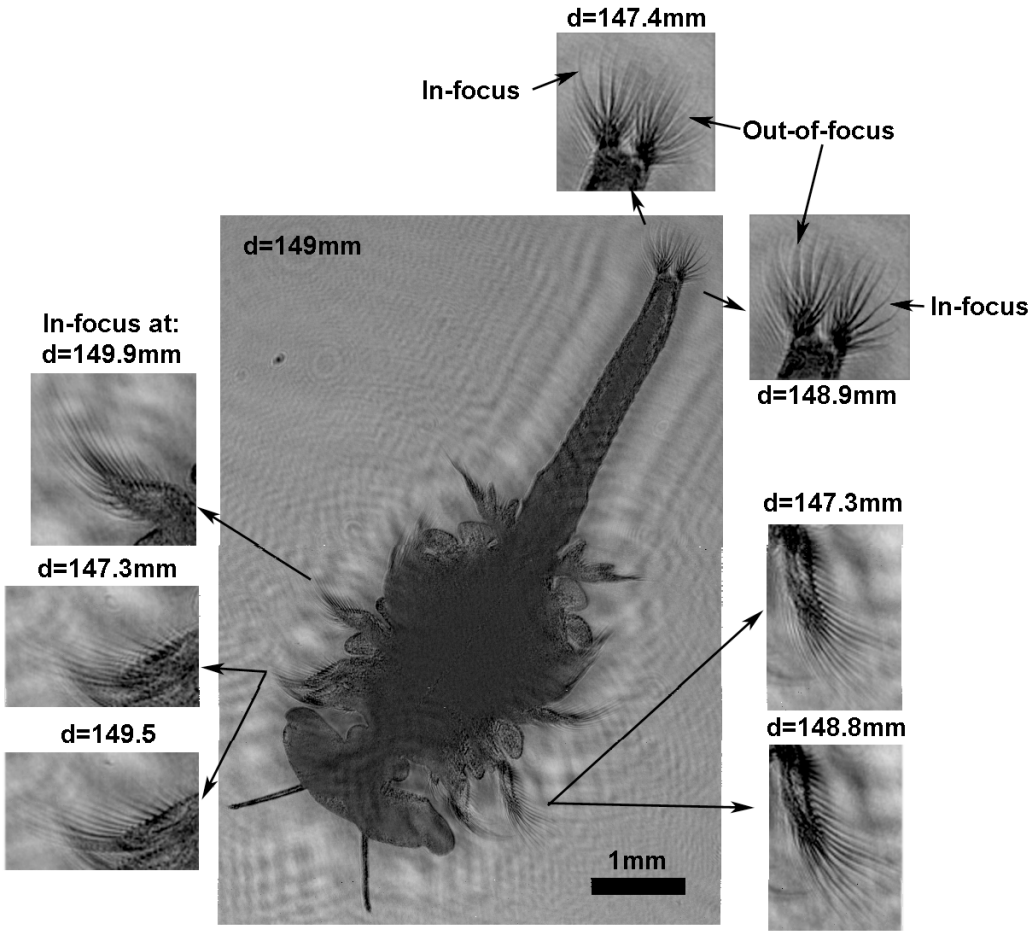

Figure 4-37: Reconstruction of a brine shrimp at d=149mm. Portions of the animal are in-focus at different imaging distances.

shown in Figure 2-8 of section 2.3.2. A brine shrimp reconstructed from a hologram recorded using this set-up with d = 266mm is shown in Figure 4-38. Although the hologram was recorded with a clean reference beam, the quality of the reconstruction is very low due to the additional aberrations introduced by the beam-splitters and mirrors. In addition, the hologram was recorded using just a small portion of the CCD presenting similar resolution degradation. If a full photosensitive area is required, larger beam-splitters and mirrors must be used, resulting in increased optical aberrations. The modified in-line Mach-Zehnder set-up with variable attenuation of Figure 2-10 in section 2.3.2 was used in this set of experiments, but additional aberrations were introduced by the $\lambda/2$ waveplates and no noteworthy results were obtained.

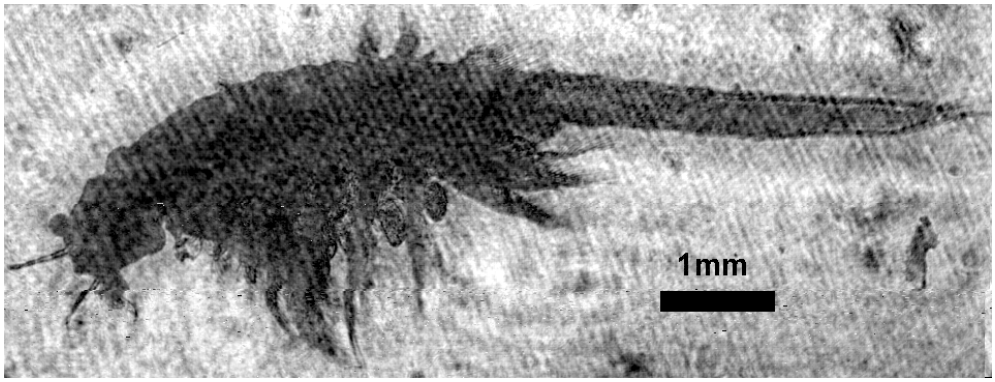

Figure 4-38: Reconstruction of a brine shrimp at d=266mm using the in-line Mach-Zehnder set-up.

The fifth set of experiments was conducted using the modified in-line Mach-Zehnder set-up with high-pass Fourier filter as shown in Figure 2-9 of section 2.3.2. In order to make the high-pass Fourier filter the following process was adopted. Firstly, an array of dots with diameters ranging from 10μm to 4mm was drawn in Autocad. This pattern was then printed on a transparency with a resolution of 10μm and finally, the pattern was moved from the transparency to chromium on Soda Lime glass plate with a thickness of 0.03 inches using photolithography. The high-pass Fourier filter was made by Anthony J.

Nichol at the NanoStructures Laboratory at MIT. An example of reconstructions made from a hologram recorded using this set-up is shown in Figure 4-39. The quality of the reconstruction is again low due to the aberrations introduced by the additional lenses and the high-pass Fourier filter.

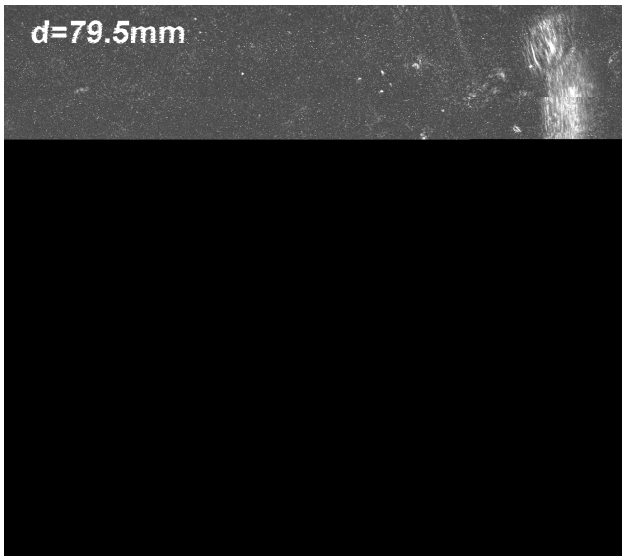

Figure 4-39: Reconstruction of a brine shrimp at d=79.5mm using the modified in-line Mach-Zehnder set-up with high-pass Fourier filter.

From the experiments presented in this section, it can be concluded that the reconstructions of highest quality were achieved by the final in-line single-beam experimental set-up shown in Figure 4-33. Additional images of reconstructions of brine shrimp are included in Appendix A.

4.8 Holographic Imaging of Copepods

In this section, the experimental results obtained from imaging live copepods are analyzed. The first set of experiments were carried out using the in-line single-beam con-

figuration shown in Figure 4-23 of section 4.7. The second set of experiments was done using the final in-line single-beam set-up shown in Figure 4-33 of the same section. The holograms were reconstructed with the convolution approach as discussed in section 2.3.2.

The copepods used in the experiments were cultured inside a tank filled with seawater. The seawater was prepared from a mix of spring water and a sea salt concentration, such as Instant Ocean ®, where the levels of salinity were kept in the range of 28 to 34 PPT (specific gravity of 1.020-1.025). When preparing the culture for the first time, ideally the seawater is let to sit for at least 24 hours before introducing the copepods to prevent the "new tank syndrome". Another method to prevent this syndrome is to add a small portion of Saltwater Biozyme ®. This product is composed of a concentration of living beneficial bacteria that become activated upon introduction to water, to convert lethal ammonia and nitrite to less harmful nitrite, activating the nitrogen cycle in the aquarium. The oxygen in the water is provided by an air pump connected through a thin tube to an air stone submerged inside the tank. It is recommended to include a pile of live rocks in one corner of the tank, as shown in Figure 4-40 to serve as a refuge for the copepods allowing them to hide and/or reproduce. Live rocks are removed from the vicinity of a tropical coral reef with all life still intact. Once the aquarium is ready, the copepods are introduced close to the pile of live rocks. The copepods are fed periodically (about every three days) with small portions of Phyto-Feast Live in order to prevent harmful bacteria growth. To obtain maximal survival of the copepods, 10-20% of the water should be changed every 2 weeks. Sold in 4oz bottles, copepods can be purchased from specialized stores, and are aquacultured by Seapods ®. Copepods used for experimental purposes are collected from the culture tank with a pipette, once a light is shone on one side of the container to attract them.

Figure 4-41 shows a typical digital hologram from an experiment with copepods. The original hologram is much larger and for display purposes only a small portion is shown.

Figure 4-42, 4-43 and 4-44 show reconstructions made for the first set of experiments

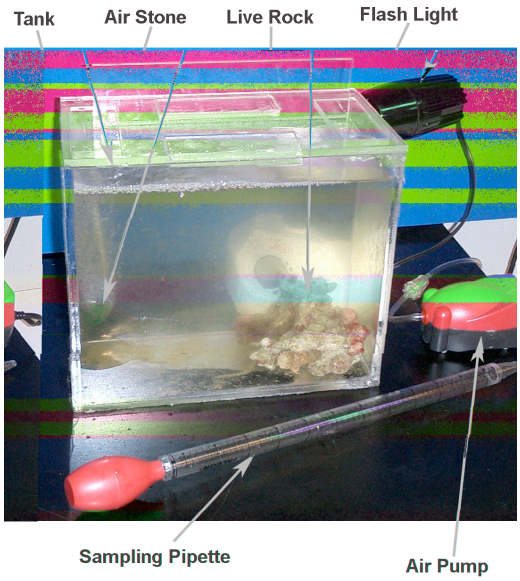

Figure 4-40: Culturing tank for copepods.

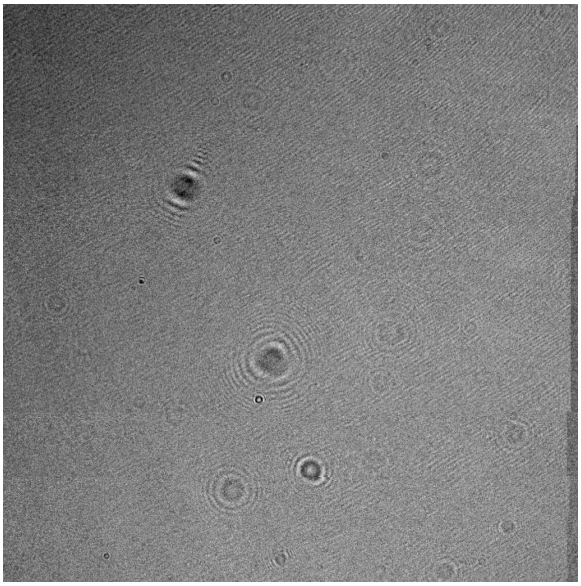

Figure 4-41: Digital hologram of free-swimming copepods.

using the set-up of Figure 4-23. It is clear from these images that small features of the copepods can be resolved, such as the antennas, feeding and swimming appendages and tail. This information is generally sufficient to develop a taxonomical classification of the specimen. As explained in Chapter 2, the out-of-focus virtual image only contributes to a uniform blur and does not considerably affect the reconstructions.

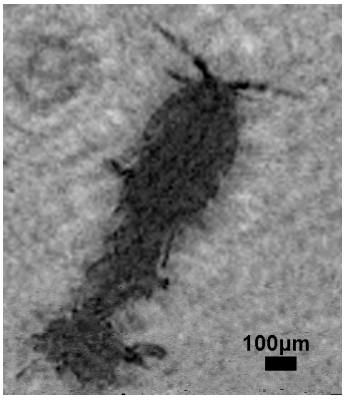

Figure 4-42: Reconstruction of a copepod using the in-line single-beam set-up with a He-Ne laser and d = 13.4mm.

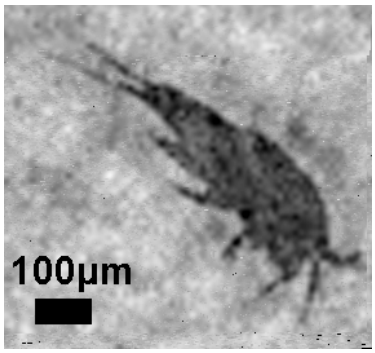

Figure 4-43: Reconstruction of a copepod using the in-line single-beam set-up with a He-Ne laser and d = 17.4mm.

The reconstructions made using the final set-up of Figure 4-33 for the second set of experiments are shown in Figures 4-45, 4-46 and 4-47. The reconstructed copepod in

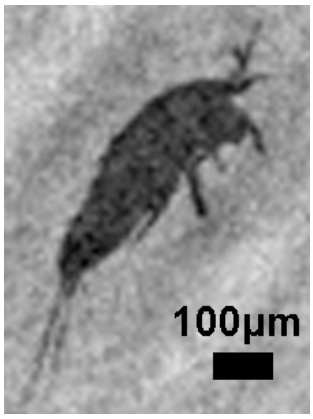

Figure 4-44: Reconstruction of a copepod using the in-line single-beam set-up with a He-Ne laser and d = 39.2mm.

Figure 4-45 is a Calanus finmarchicus. This copepod was captured using a plankton net from the Cape Cod canal with a sandwich boat basin in an expedition on August 2, 2005 at 11:30pm. These reconstructions show an increase in quality as the integration time of the system is set to a shorter period. Figure 4-46 was reconstructed using the exact kernel of the convolution approach as indicated by equation 2.11 of section 2.2.1. The ripples present in this reconstruction result from the aberrations introduced by the virtual image. Additional reconstructions of free-swimming copepods are included in Appendix B.

The experimental set-up with spherical reference wave, as shown in Figure 2-11 of section 2.2.3, presents a promising configuration that without any lenses magnifies the recorded field resolving finer details of the copepod. With this configuration, the computer-generated reference wave used in the reconstruction algorithm is given by

$$r_d(x_h, y_h) = \exp\left[-i\frac{2\pi}{\lambda}\sqrt{d_r^2 + (x_h - x_r)^2 + (y_h - y_r)^2}\right], \tag{4.11}$$

where, (x_r, y_r, d_r) are the coordinates of the reference source point.

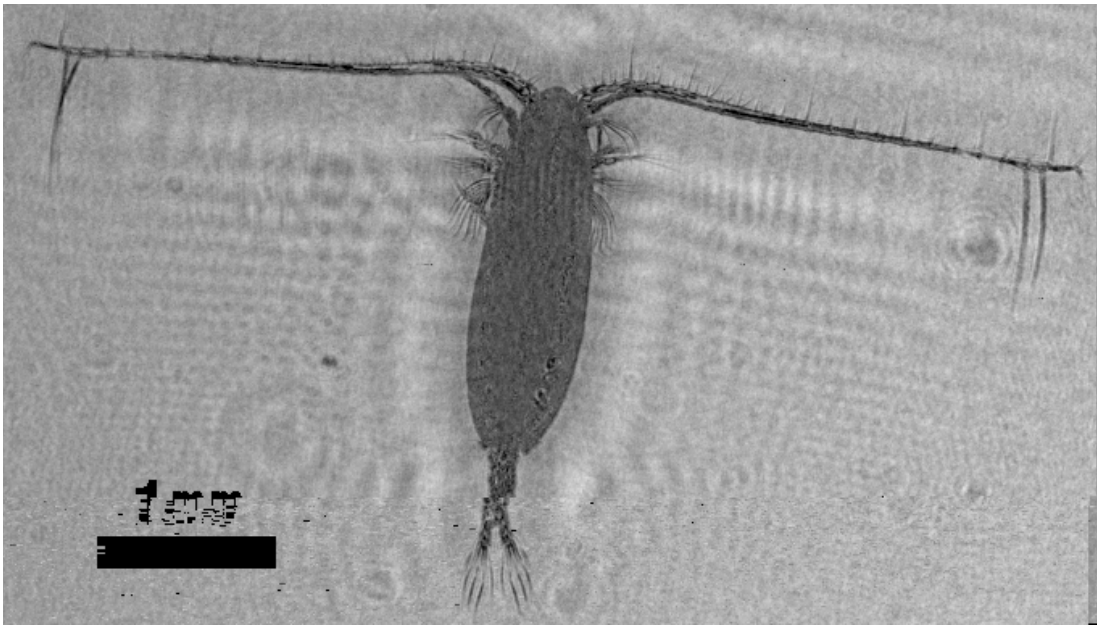

Figure 4-45: Reconstruction of a copepod (Calanus finmarchicus) using the final in-line single-beam experimental set-up with a modulated diode laser and d = 101mm.

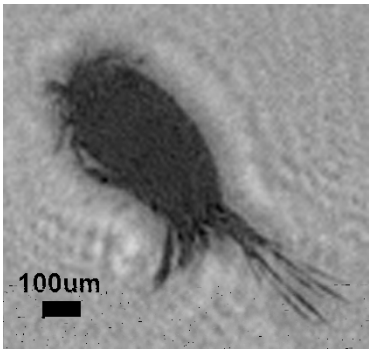

Figure 4-46: Reconstruction of a copepod using the final in-line single-beam experimental set-up with a modulated diode laser and d = 7.7mm.

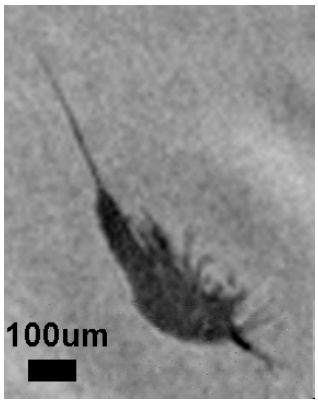

Figure 4-47: Reconstruction of a copepod using the final in-line single-beam experimental set-up with a modulated diode laser and d = 66mm.

Figure 4-48 shows the last three groups of a 1951 USAF resolution target reconstructed from a hologram recorded using this set-up. From the magnified reconstruction it is possible to resolve the smallest set of lines of the fourth group that have the following dimension: 10.96μm$\times$2.19μm spaced every 2.19μm.

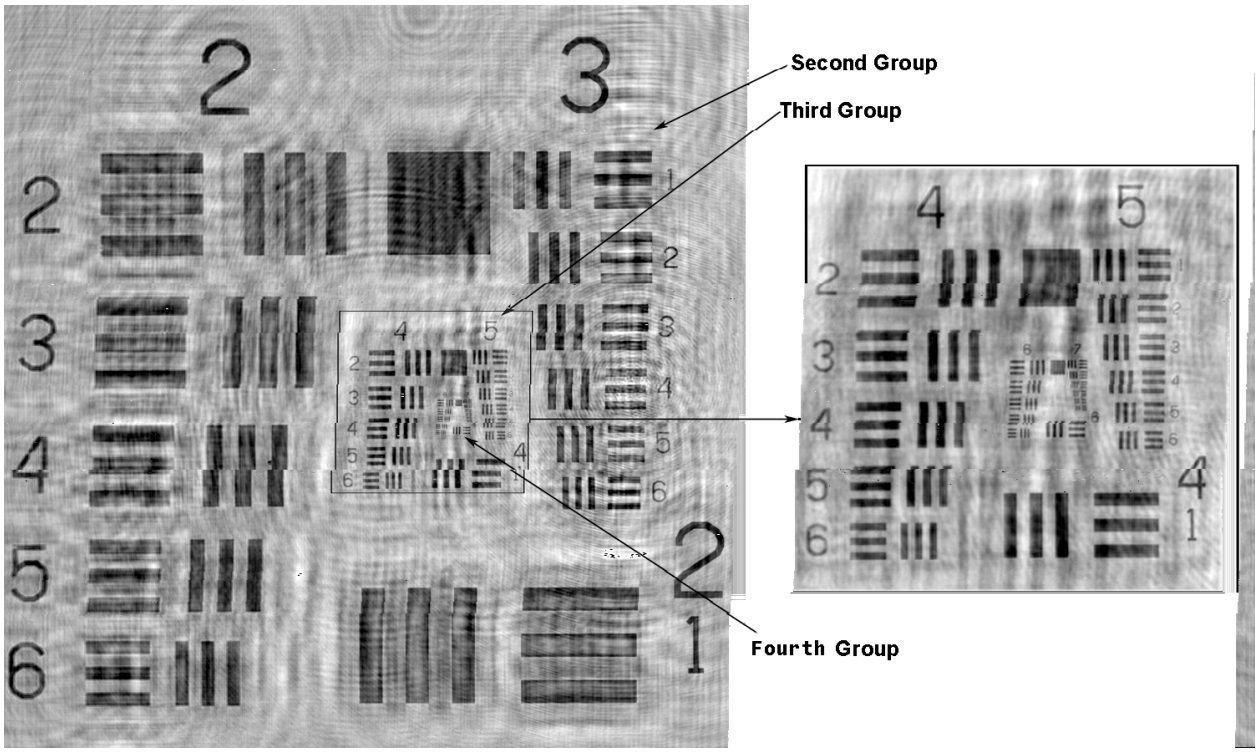

Figure 4-48: Reconstruction of a 1951 USAF resolution target using the experimental set-up with a spherical reference wave.

Chapter 5

Image Post-Processing Algorithms

In this chapter several image post-processing algorithms applied for underwater digital holography are discussed. Some of these techniques, such as the DC term suppression algorithm, are intended to produce a global enhancement in the reconstructed image. Optimization in the reconstructions is made possible by the implementation of procedures such as the reconstruction of large holograms or auto-scan techniques. The algorithm to produce and reconstruct binary holograms allows the characterization of the imaging system when operating with low powered laser light.

5.1 Reconstruction of Large Holograms

The large holograms captured by our CCD, require special reconstruction algorithms in order to avoid memory problems and long computational times. All the reconstructions conducted in this thesis used Matlab 6.5 on a Pentium IV 3.8GHz personal computer. The reconstruction by the convolution approach, as shown in Figure 2-18 of section 2.3.2, initially requires loading the hologram to form a 4096×4096 matrix. This matrix is then Fourier transformed by means of the 2D fast Fourier transform algorithms (2D FFT) to form the spectrum of the hologram in a matrix of similar size. When using the paraxial

approximations, the diffraction kernel is computed forming another 4096×4096 matrix. This matrix is then pointwise multiplied to the spectrum of the hologram to obtain the spectrum of the reconstructed image. The final step in the reconstruction algorithm is to compute the 2D inverse FFT of the spectrum of the reconstructed image. Two main issues arise when performing the reconstruction of large holograms in Matlab. Firstly, the program is extremely time consuming due to the large number of operations involved (less than $N\log_2(N)$ for the FFTs and N^2 for the pointwise multiplication, where $N = 4096$). Secondly, the program exceeds available memory when storing the large variables. This can sometimes be overcome by increasing the computer's virtual memory and/or by running Matlab without the visual interface. Unfortunately, these two solutions are not sufficient when reconstructing large holograms.

Three algorithms were developed to solve the issue of reconstructing large holograms. The first algorithm achieves the reconstruction by optimizing the computations without storing any variables on the hard drive. The schematic of this algorithm is depicted in Figure 5-1. As shown in Figure 5-1, the first two steps involve loading the hologram and computing its Fourier transform. In order to optimize the memory usage in the third step, the kernel is formed in blocks. In the fourth step, the first two blocks of the spectrum and kernel matrices are pointwise multiplied and stored in a new variable. These blocks are then set to zero in the fifth step generating sparse matrices. In the sixth step, a sparse matrix optimization algorithm is run to reduce the size of the matrices. The remaining blocks are pointwise multiplied in the seventh step. The results from the fourth and seventh steps are collected in the eighth step to create a new matrix that forms the spectrum of the reconstructed image. In the final step, an inverse Fourier transform is performed to compute the reconstructed image. For reconstruction of several planes, the algorithm is looped from steps III-IX.

The second algorithm to reconstruct large holograms involves storing one variable to the hard drive. As shown in Figure 5-2, the main difference from the first algorithm is

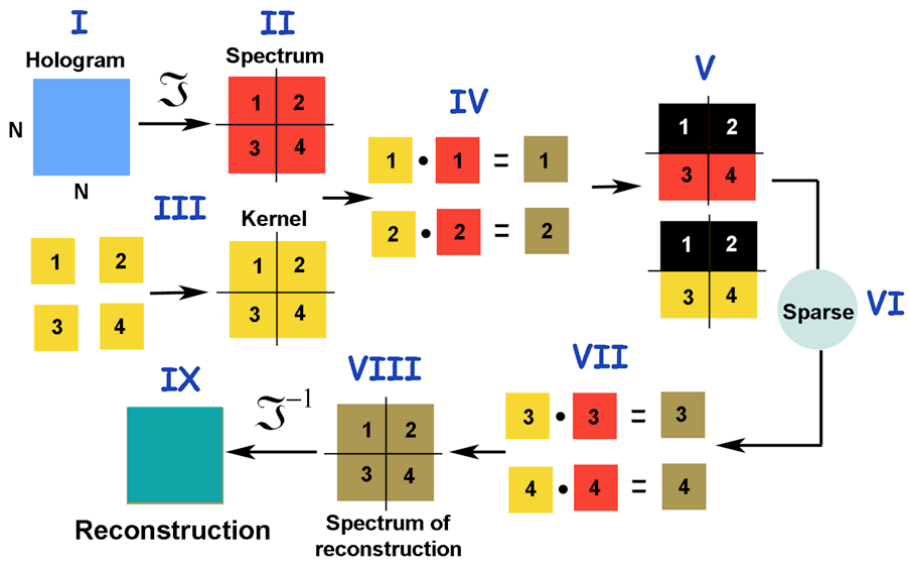

Figure 5-1: Schema of the algorithm for the reconstruction of large holograms with no storage of variables to the hard drive.

that the spectrum of the hologram is stored to the hard drive in the first step. Also, there is no need to set the first two blocks of the spectrum and kernel matrices to zero or to use the sparse algorithm. The memory is optimized by not having the spectrum of the hologram present when forming the kernel. Once the kernel is formed, the spectrum matrix is loaded and used to compute the reconstructed image. Steps II-IV are repeated for all reconstruction planes.

An improved algorithm is depicted in Figure 5-3 where the kernel matrix is also read from the hard drive. This involves the usage of additional disk space, as the kernels have to previously be generated for all reconstruction planes. However, the memory used by the program is considerably smaller and the computational time is shorter than that of the other two algorithms as shown in Figures 5-4 and 5-5.

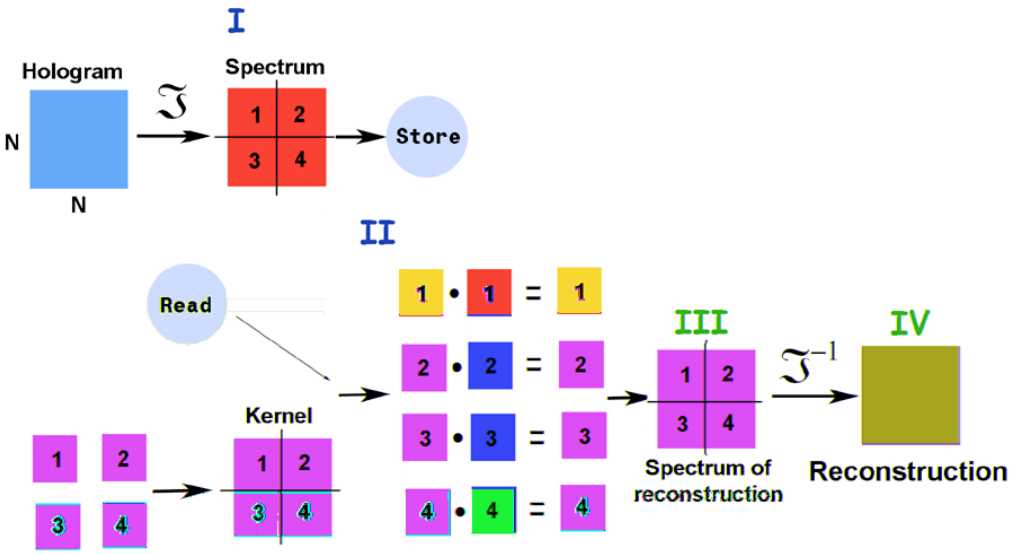

Figure 5-2: Schema of the algorithm for the reconstruction of large holograms after storing the spectrum of the hologram to the hard drive.

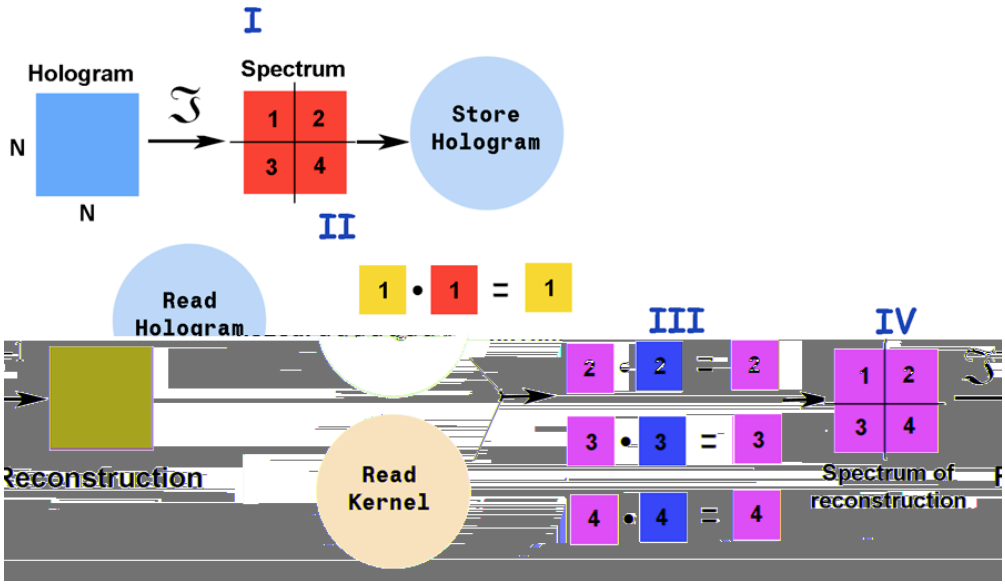

Figure 5-3: Schema of the algorithm for the reconstruction of large holograms after storing the spectrum of the hologram and reading the kernel from the hard drive.

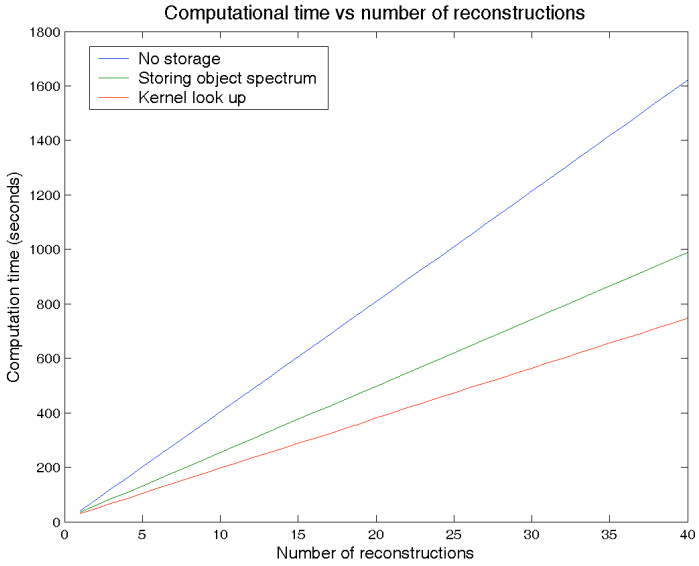

Figure 5-4: Comparison of the required computational time as a function of the number of reconstructions for the three algorithms.

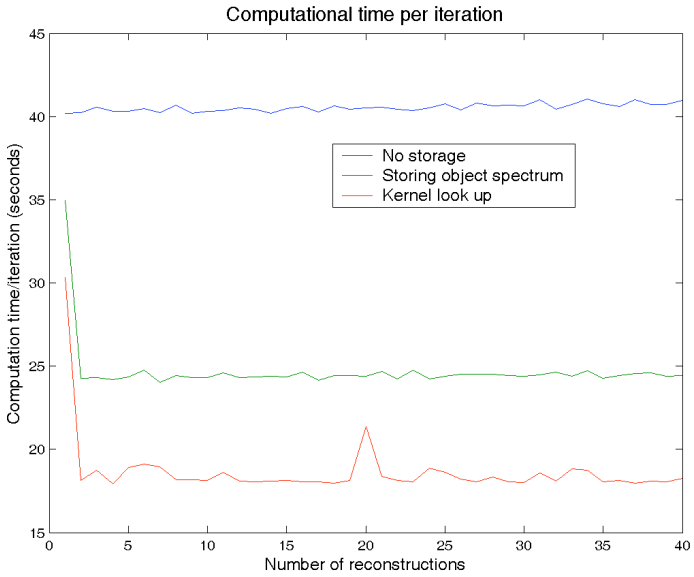

Figure 5-5: Comparison of the computational time for each iteration in reconstructing several planes for the three algorithms.

5.2 Reconstruction of Binary Holograms

The generation and reconstruction of binary holograms enables the prediction of the quality of the reconstructions when the received power is very low. As discussed in section 4.3.5, when the power of the laser source used to record the hologram is reduced, the effective usage of the dynamic range of the CCD is also reduced. In the worst case, the hologram is encoded using just one bit of precision. In order to emulate this effect, a recorded hologram is converted into a binary image by computing its histogram and imposing a threshold on intensity levels. Pixels with levels of intensity larger than the threshold are set to one, while the remaining pixels are set to zero. A comparison between the original copepod hologram and the two binary holograms generated for different threshold values is shown in Figure 5-6. The histogram of the original hologram is shown in Figure 5-7.

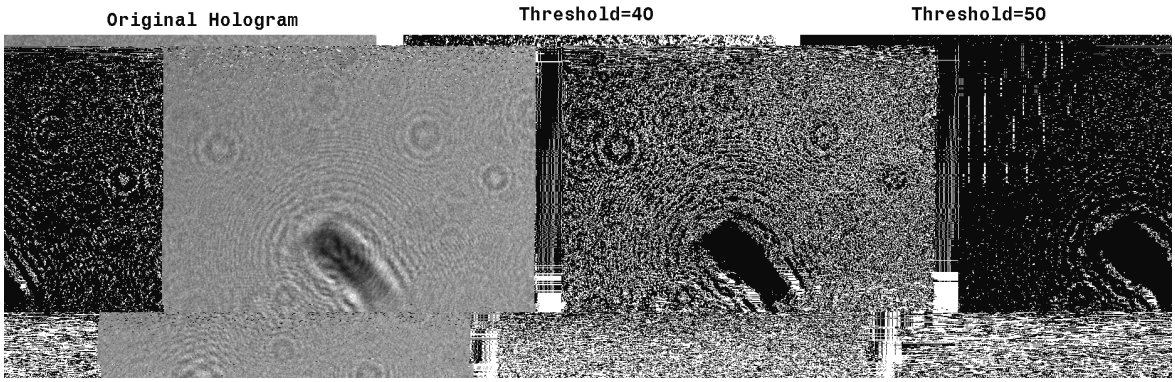

Figure 5-6: Comparison between the original copepod hologram and two binary holograms with threshold = 40 and threshold = 50.

Figure 5-8 shows the comparison of the reconstructions conducted for the holograms presented in Figure 5-6 with $d = 114.4$m. As seen in Figure 5-8, the original hologram achieves the highest quality reconstruction. However, the reconstructions performed from

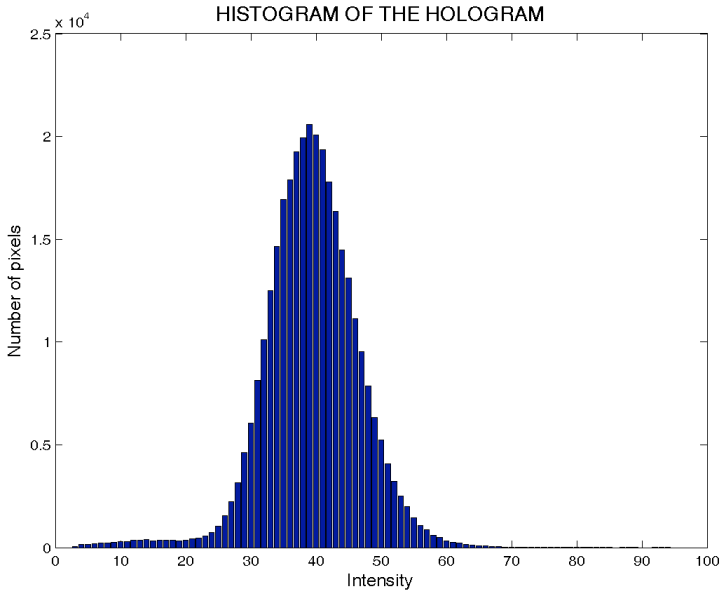

Figure 5-7: Histogram of the original copepod hologram.

the binary holograms also depict significant detail, making taxonomical classification possible. The possibility to reconstruct images from binary holograms is due to the large amounts of information contained in a single hologram.

Another interesting property of holograms is that they encode information from a single portion of the object space in the entire photosensitive area. In order to experimentally explore this, a portion of the hologram is set to zero forming the letters "MIT". The modified hologram is then reconstructed at d=114.4mm as shown in Figure 5-9. As can be seen from this figure, the image of the copepod is still reconstructed, even if it is corrupted by the aberrations introduced by the out-of-focus image produced by the "MIT" pattern.

Figure 5-8: Comparison between the original copepod hologram reconstruction and the reconstructions from the two binary holograms at d=114.4mm.

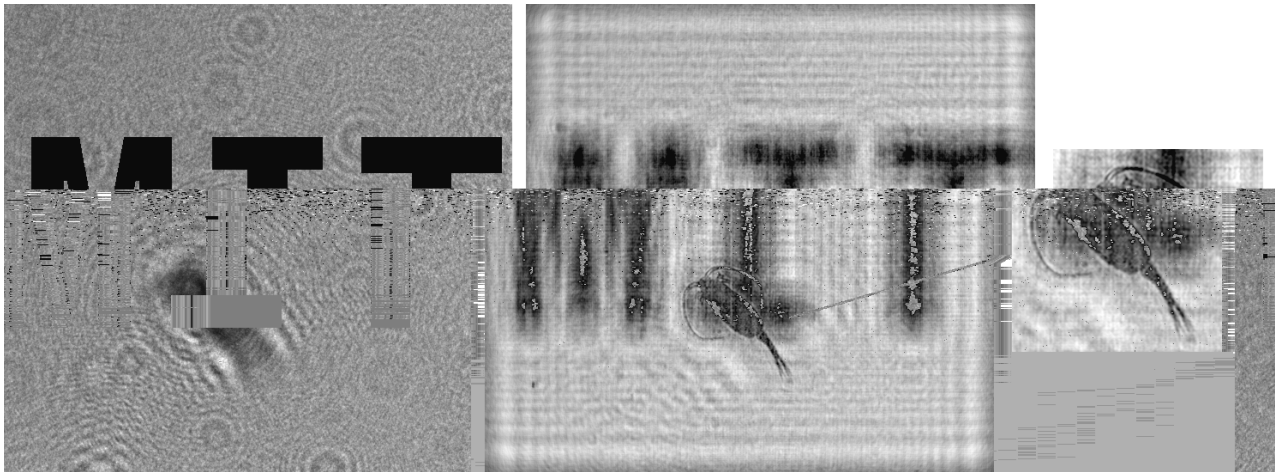

Figure 5-9: To the right: a hologram of a copepod modified by setting a portion to zero forming the letters "MIT". To the left: Reconstruction of the modified hologram at d=114.4mm.

5.3 Auto-scan Reconstruction Algorithm

The vast amount of information contained in a single hologram requires the development of auto-scan reconstruction algorithms. These algorithms are intended to avoid the tedious and time-consuming manual scanning of holograms where an observer determines when the image is in focus. The type of auto-scan algorithm to be implemented is a function of the specific application. Based on different criteria, several algorithms to find the in-focus image from the reconstruction of holograms have been reported. A reconstruction algorithm based on the image's self-entropy for measuring the focus was proposed in [136]. The measurement of the phase shift of the hologram fringes to track the axial displacement in real time was reported in [137]. Liebling and Unser proposed an autofocus algorithm based on the Fresnelet-sparsity criterion [138]. Auto-scan algorithms for holograms recorded in film were reported in [42] and [102]. Some automated focusing systems were developed for the location of bubbles and droplets [139], [140], [141], [142].

In this section an auto-scan reconstruction algorithm developed for holographic imaging of aquatic species is presented. This algorithm allows the reconstruction of several objects recorded at different imaging distances from a single hologram. Figure 5-10 shows the block diagram for the proposed algorithm. As shown in Figure 5-10, the input of the auto-scan reconstruction algorithm is the hologram captured using an in-line single-beam configuration as discussed in Chapter 4. The hologram varies in intensity along the incidence plane according to the profile of the illumination beam used in the recording step. This variation is not desirable as it reduces the contrast and thus is not accounted in the derivations presented in Chapter 2 for the reconstruction algorithm, where uniform background was assumed. For this reason, the second step in the auto-scan reconstruction algorithm is the block averaging section, which to some degree modifies the hologram by correcting these variations. The third step is the instant-volume reconstruction section, which retrieves all the objects contained in the sampled volume from a modified reconstruction kernel. The output image contains a collection of "blobs" that represent

the objects present in the volume of water. In order to determine the regions of interest (ROI), this image is passed through the thresholding section and analyzed. In this context, the ROI are defined as regions that contain the object of interest, which will be processed by the auto-focus algorithm. The auto-focus algorithm is a Laplacian-based method designed to estimate the in-focus image for each ROI. The steps involved in this auto-scan reconstruction will be covered in more detail the following subsections.

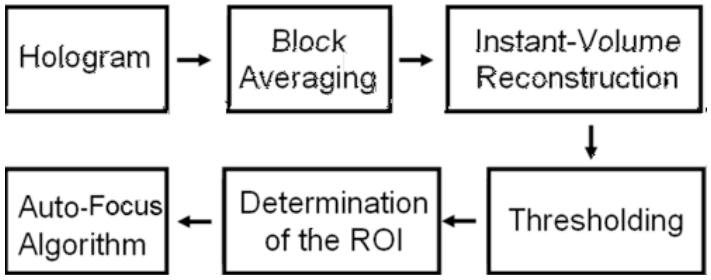

Figure 5-10: Auto-scan reconstruction algorithm.

5.3.1 Block-averaging Algorithm

The block-averaging algorithm is used to correct the variations in intensity present in the hologram. These variations are produced by the profile of the light beam used to record the hologram. For the experiments shown in Chapter 4, the recording beam had a Gaussian profile. The highest intensity was aligned to be approximately at the center of the CCD with the intensity decreasing to the outer part.

Figure 5-11 shows a schematic of the block-averaging algorithm. In this algorithm, the first step is to compute the average intensity of a block of m×m pixels and then subtract it to each pixel in the block. Next, the block is shifted and the first step is repeated. This is done until the entire hologram has been processed.

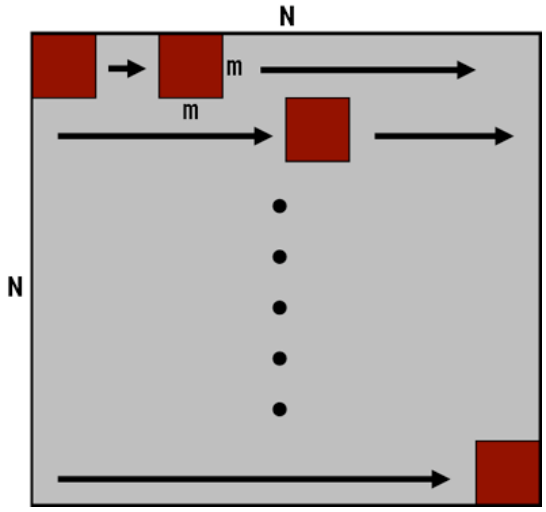

Figure 5-11: Schematic of the block-averaging algorithm.

In order to show this algorithm, we use the 2048×2048 pixels hologram shown in Figure 5-12 as an input which was captured using an in-line single-beam configuration. This is a hologram of copepods collected in the Boston's Harbor on November 17th., 2005 at 1p.m. Figure 5-13 shows the modified hologram after the implementation of the block-averaging algorithm with a block size of 128×128 pixels. Although the modified hologram is used as the input to efficiently determine the ROI, the original hologram is used for the final reconstructions. The modified hologram of Figure 5-13 took 0.494sec to compute on a Pentium IV at 3.8GHz personal computer using Matlab 7.0.

5.3.2 Instant-volume Reconstruction Algorithm

The main goal of the instant-volume reconstruction algorithm is to reconstruct all the objects contained in a sampled volume in a single pass. This was initially introduced by Jerome H. Milgram [143] in the context of determining micro-organism population densities using holography. In Chapter 2, the derivation of the kernel used to reconstruct

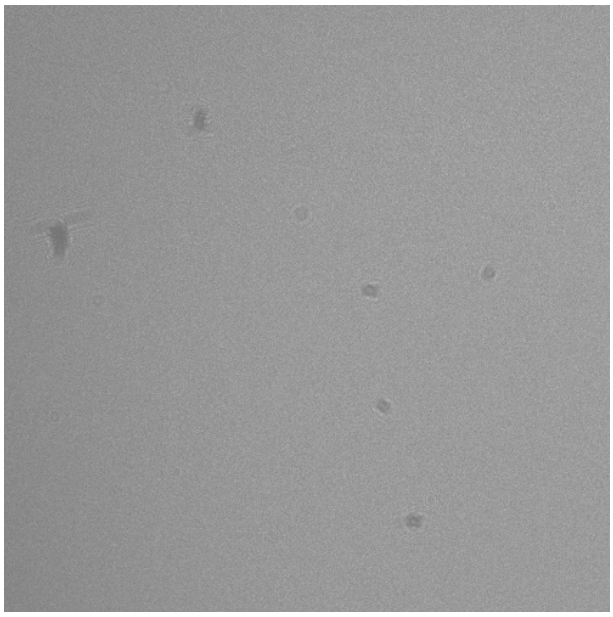

Figure 5-12: Hologram of copepods collected in the Boston's Harbor on November 17th, 2005 at 1p.m.

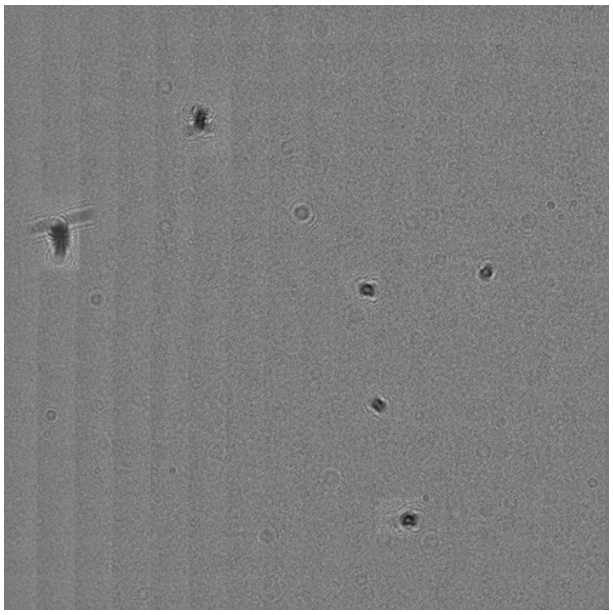

Figure 5-13: Modified hologram after the implementation of the block-averaging algorithm with a block size of 128×128 pixels.

a single plane at a fixed distance from the CCD was presented. Figure 5-14 shows a schematic of this type of reconstruction, in which there is a tank with two copepods located at different imaging distances from the CCD. The red plane represents the reconstruction that focuses on the second copepod. In a similar way, the instant-volume reconstruction algorithm can be thought of as several reconstruction planes separated by a small amount covering the entire sampled volume as shown in Figure 5-15. The intensities of the reconstructed planes are added up. The sampled objects are in-focus in more than one plane and out-of-focus in other planes. The resulting image contains bright regions on the locations of objects against a dark background. This image is processed in the next section to find the ROI.

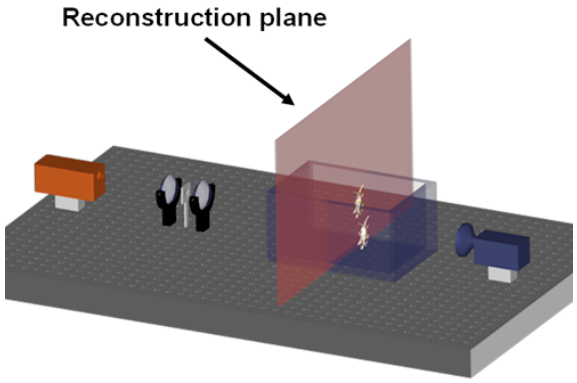

Figure 5-14: Schematic of a reconstruction of a single plane.

The implementation of the instant-volume reconstruction algorithm is the same as the reconstruction algorithm discussed in Chapter 2. The only modification is in the kernel, which can be generated by the summation of individual exact kernels (either in spatial or frequency domains) generated at different imaging distances

$$h_{iv}(x, y, d) = \sum_{m=1}^{M} h(x, y, m\Delta d); \tag{5.1}$$

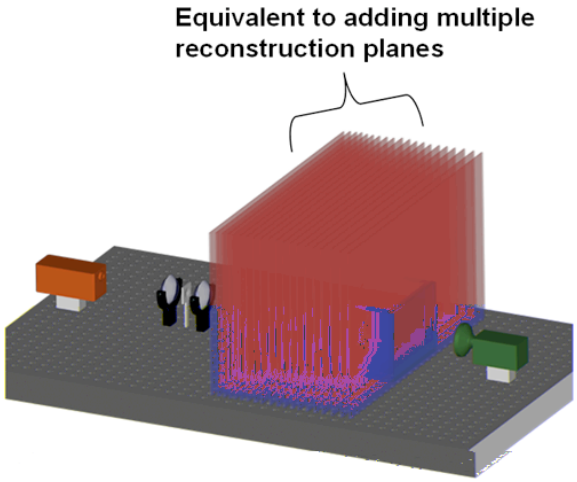

Figure 5-15: Schematic of the instant-volume reconstruction algorithm.

$$H_{iv}(x,y,d) = \sum_{m=1}^{M} H(x,y,m\Delta d), \tag{5.2}$$

for

$$d = \Delta d, 2\Delta d, ...M\Delta d.$$

For the case of the paraxial approximated kernel in frequency domain, it is possible to compute the instant-volume kernel analytically by, [143],

$$H_{iv} = \frac{i2\pi}{k} \sum_{m=1}^{M} \exp\left[-i\frac{2\pi^2 m\Delta d}{k}(f_x^2 + f_y^2)\right] = \begin{cases} \frac{i2\pi}{k}\frac{Q-Q^{M+1}}{1-Q} & Q \neq 1 \\ \frac{i2\pi}{k}M & Q = 1 \end{cases} \tag{5.3}$$

where

$$Q = \exp\left[-i\frac{2\pi^2 m\Delta d}{k}(f_x^2 + f_y^2)\right] \tag{5.4}$$

Figure 5-16 shows the output of the instant-volume reconstruction algorithm for the modified hologram of section 5.3.1. This image took 3.92sec to compute.

Figure 5-16: Reconstruction performed by the instant-volume reconstruction algorithm from the modified hologram of section 5.3.1.

5.3.3 Thresholding, Analysis and Determination of the ROI Algorithms

The block diagram of this algorithm is shown in Figure 5-17. From the image reconstructed by the instant-volume reconstruction algorithm, the first step involved thresholding to produce a binary image such as the one shown in Figure 5-18, which took 1.703sec to compute. In the second step and third steps, all the binary objects are labeled and analyzed to obtain values for their area, centroid and tight bounding box. For these experiments, the steps were performed using various functions available in the Image Processing Toolbox of Matlab [144]. In the fourth step, an area test is conducted in which only objects with an area larger than a specified threshold are processed. This test is designed to avoid reconstructing small objects such as dust particles that are not of interest. The properties of the extended bounding box of the objects that pass the

area test is saved into an array and is then passed onto the next algorithm. The extended bounding box is computed by increasing the size of the tight bounding box, which encloses a single binary object. The offset introduced in the extended bounding box serves to keep some of the high frequency information of the object mapped in the hologram in order to efficiently find the in-focus image. In the final stage of this algorithm, the bounding boxes are drawn and displayed in order to give a visual output of the identified objects. Figure 5-19 is an example of such an output. This image took 0.267sec to compute.

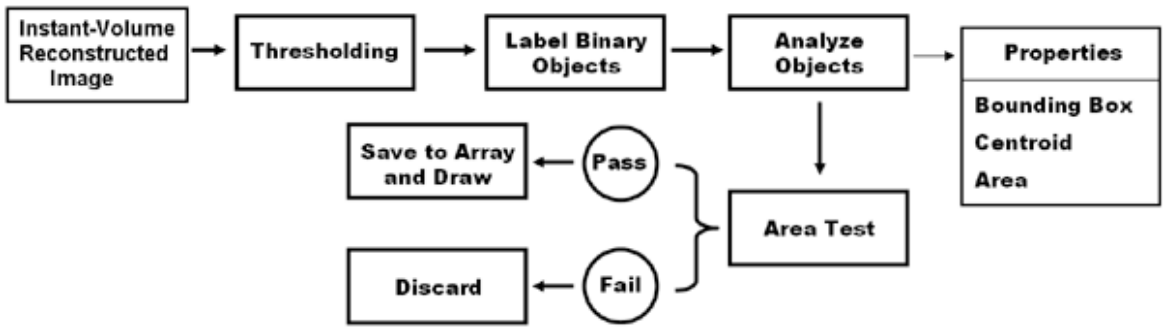

Figure 5-17: Block diagram of the thresholding and analysis algorithm.

5.3.4 Auto-focus Algorithm

The final section is the auto-focus algorithm. The block diagram of this algorithm is shown in figure 5-20. For each ROI, a coarse scan is performed to estimate the possible axial coordinate of the object. The selection of the scanning range is a function of the configuration used in recording the hologram and affects the required computational time.

In the in-line single beam configuration, the forward scatter light from the object contributes to the hologram formation and thus, the reconstructed image is the contour

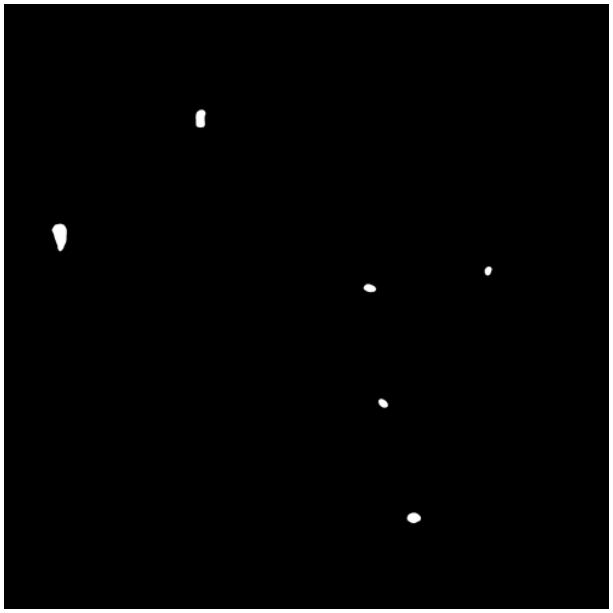

Figure 5-18: Binary image after thresholding.

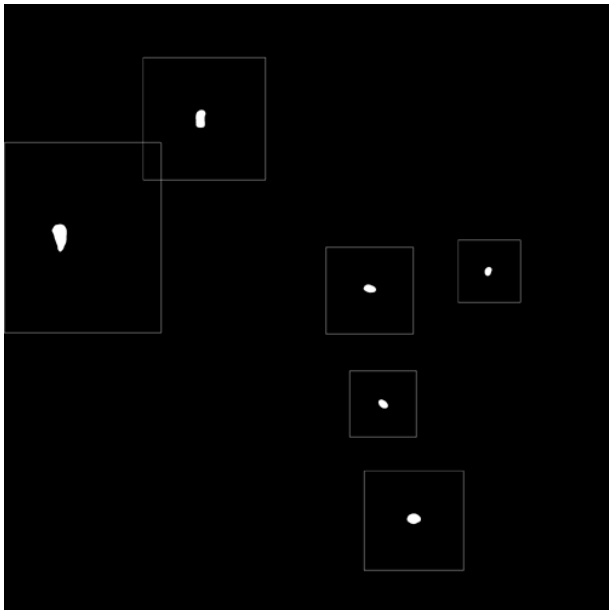

Figure 5-19: Identified ROI from the binary image.

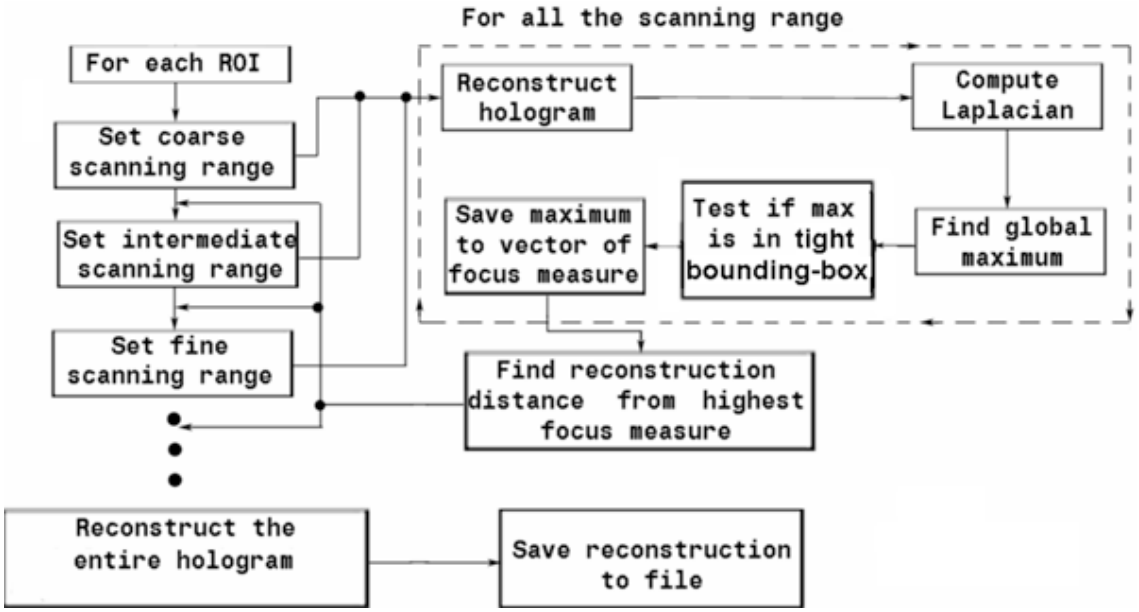

Figure 5-20: Block diagram of the auto-focus algorithm.

or shadow of the object. For an in-focus image, sharp edges in the perimeter of the object a

verifies if this value lies inside the tight bounding box of the object. If the maximum value is inside the tight bounding box, it is added to the focus measure vector; otherwise it is set to zero. This test is performed to avoid the detection of undesirable particles in the vicinity of the object inside the extended bounding box. If this test is not included, these undesirable objects may produce a focus measure of large magnitude that causes the algorithm to stop when they are in-focus.

The coarse axial position of the object is estimated from the location of the highest focus measure as shown in Figure 5-21. This figure was generated from the reconstruction of one of the six identified objects of the hologram discussed above.

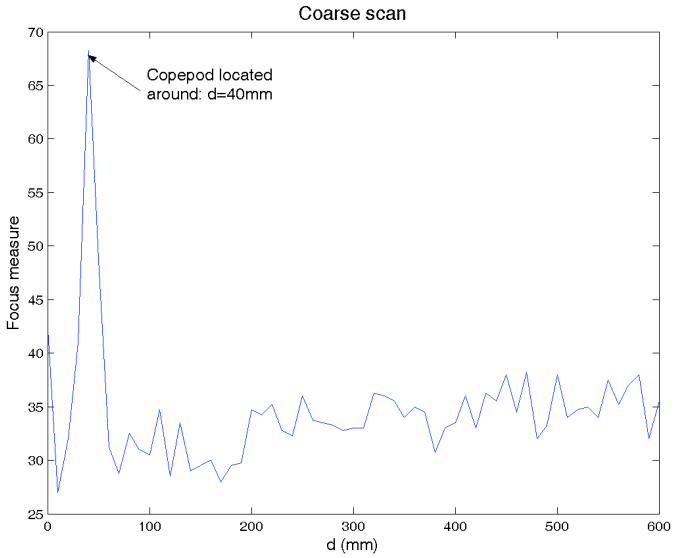

Figure 5-21: Detection of the object's axial position from a coarse scan.

The axial coordinate found by the coarse scan is used to generate an intermediate scan, which covers a smaller and denser range of reconstruction planes. Figure 5-22 shows the magnitude of the focus measure as a function of distance of an intermediate scan for the example described above.

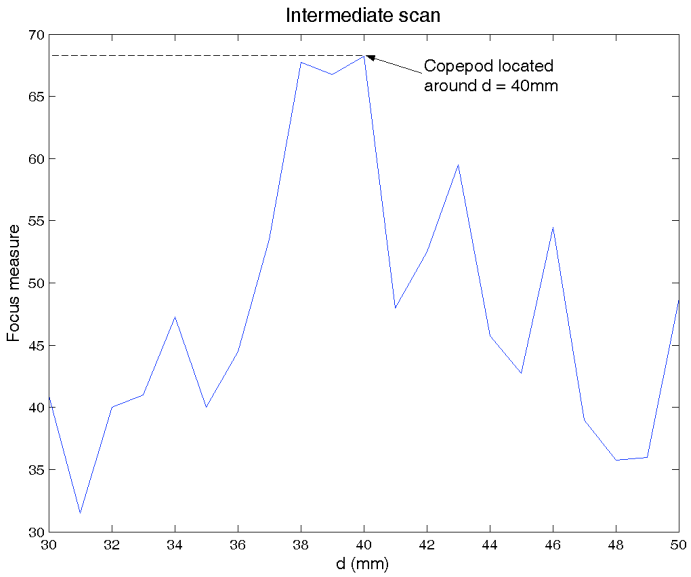

Figure 5-22: Detection of the object's axial position from an intermediate scan.

A fine scan is necessary to obtain the exact location of the target. This scan is tuned according to the desired resolution taking into account the depth of focus or the axial resolution of the system. An example of a fine scan in the range [39.5,40.5] with steps of 0.1mm is shown in Figure 5-23. Figure 5-24 shows an additional scan made in the range [40,40.4] with steps of 0.01mm. The final object location is d=40.25mm.

The in-focus reconstructed image for this object is shown in Figure 5-25. Figures 5-26 and 5-27 show the in-focus images for the additional objects identified in the sample hologram. The reconstruction of the six identified objects using the auto-focus algorithm took 106.57sec to complete.

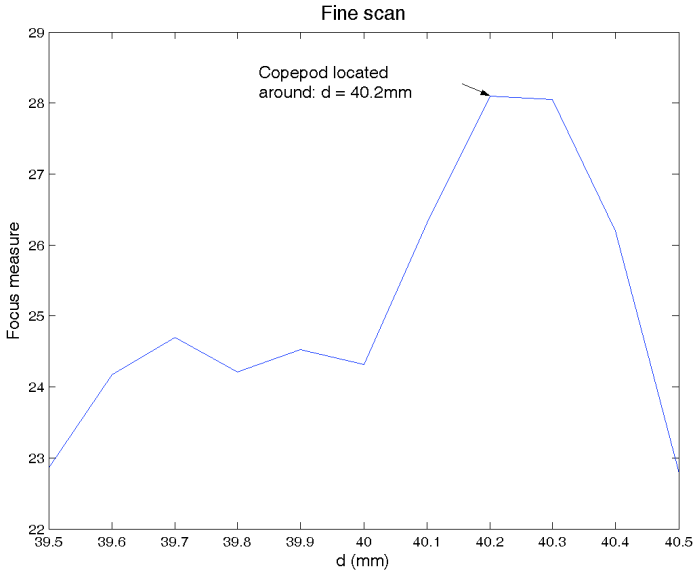

Figure 5-23: Detection of the object's axial position from a fine scan: step size = 0.1mm.

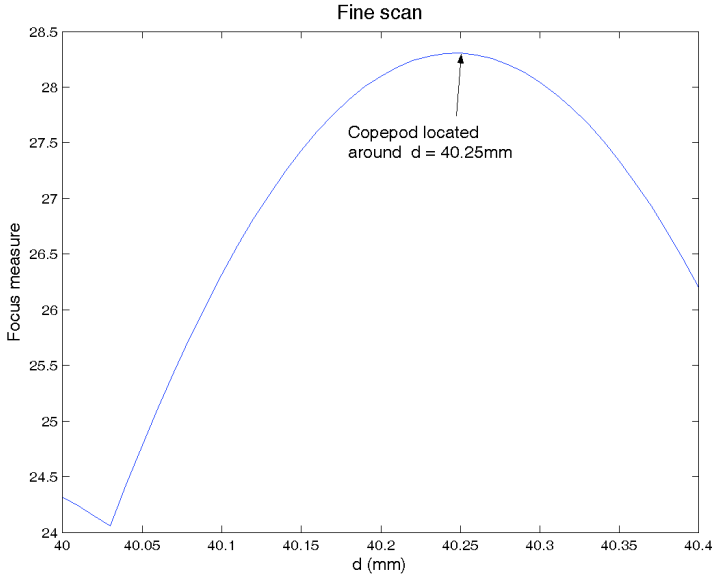

Figure 5-24: Detection of the object's axial position from a fine scan: step size = 0.01mm.

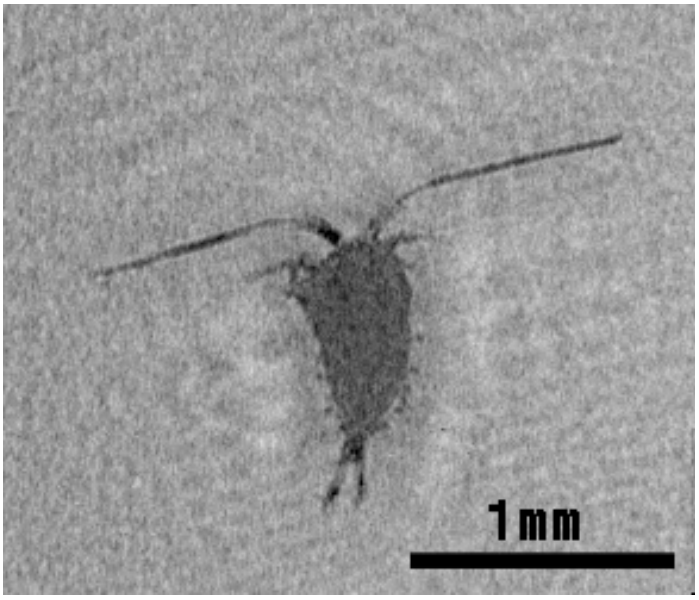

Figure 5-25: In-focus reconstructed image of a copepod at d = 40.25mm.

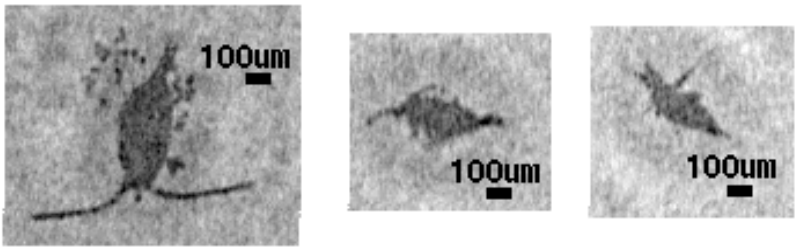

Figure 5-26: In-focus reconstructed images of copepods. From left to right, imaging distances: d= 62.5mm, d= 75mm and d = 69.5mm.

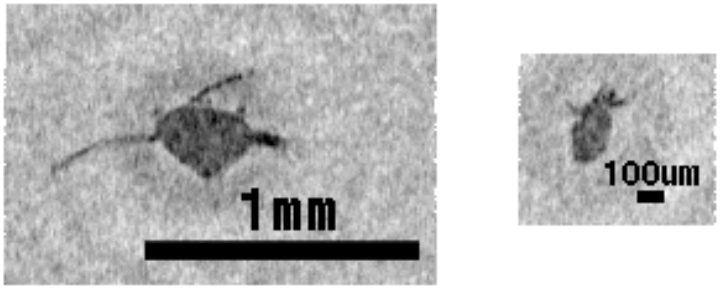

Figure 5-27: In-focus reconstructed images of copepods. From left to right, imaging distances: d= 73mm and d = 77mm.

5.4 Analysis of Reconstructed Images

The analysis of reconstructed images is a fundamental task in underwater DHI, providing the estimation of the object's location, size and orientation. This information may serve as an input to other algorithms, s

erosion to be identified by the measuring algorithm. The final step is to compute several measurements from the label binary object such as: area; maximum and minimum lateral extends; orientation and coordinates of the centroid. Figure 5-29 shows the output image produced by the analysis algorithm.

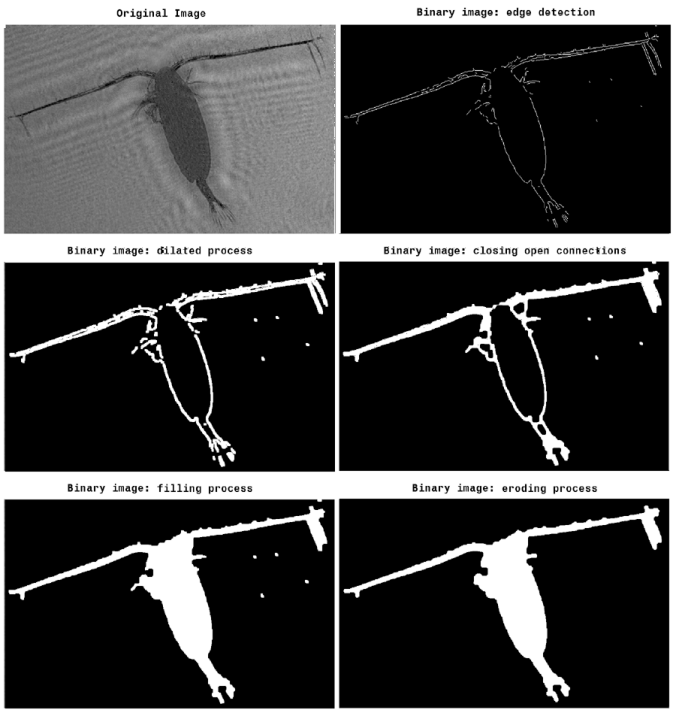

Figure 5-28: Image processing sequence produced by the analysis algorithm.

5.5 Suppression of the DC term

In this section, four algorithms designed to remove the DC term from the reconstructed images are discussed. These algorithms are developed to produce a global enhancement in the reconstruction. As explained in section 2.2.2, the DC term is composed of the first two terms of equation 2.5. When present in the reconstruction, the DC term reduces

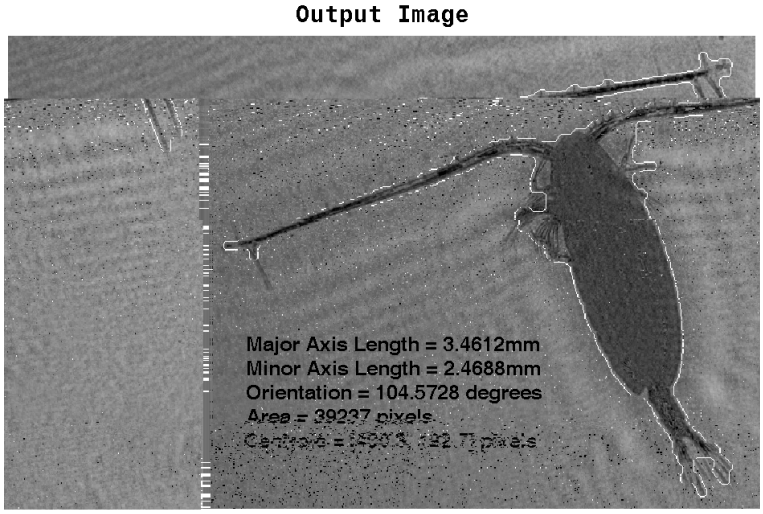

Figure 5-29: Output Image from the analysis algorithm.

the contrast and resolution of the image. From the two terms that constitute the DC term, the undiffracted reference wave is more prominent, causing a shift in the average intensity of the hologram. The contribution of the reference wave to the DC term is the basis of the first suppression algorithm where the hologram is modified by subtracting the average intensity from each pixel [145]:

$$\hat{I}(k\Delta x, l\Delta y) = I(k\Delta x, l\Delta y) - I_m, \tag{5.6}$$

for

$$k = 0, ..., N-1 \quad \text{and} \quad l = 0, ..., M-1,$$

where: $\hat{I}$ is the modified hologram, I is the original hologram and I_m is the average intensity given by

$$I_m = \frac{1}{NM} \sum_{k=0}^{N-1} \sum_{l=0}^{M-1} I(k\Delta x, l\Delta y). \tag{5.7}$$

Figure 5-30 shows the original hologram of a copepod and the modified hologram produced using equation 5.6. Figure 5-31 shows the reconstructions conducted for these

holograms using $d = 66.1$mm. As shown in Figure 5-31 where the DC term is suppressed, the reconstructed field from the hologram has a better contrast. In addition, the ripples introduced at the edges of the hologram when zero padding its Fourier transform disappear. This is produced by the effective cancellation of the center spike in the spectrum of the hologram. The suppression of the DC term which occurs in the phase of the reconstructed field produces a significant improvement as it reveals information that was previously covered by the phase distribution of the DC term as shown in Figure 5-32.

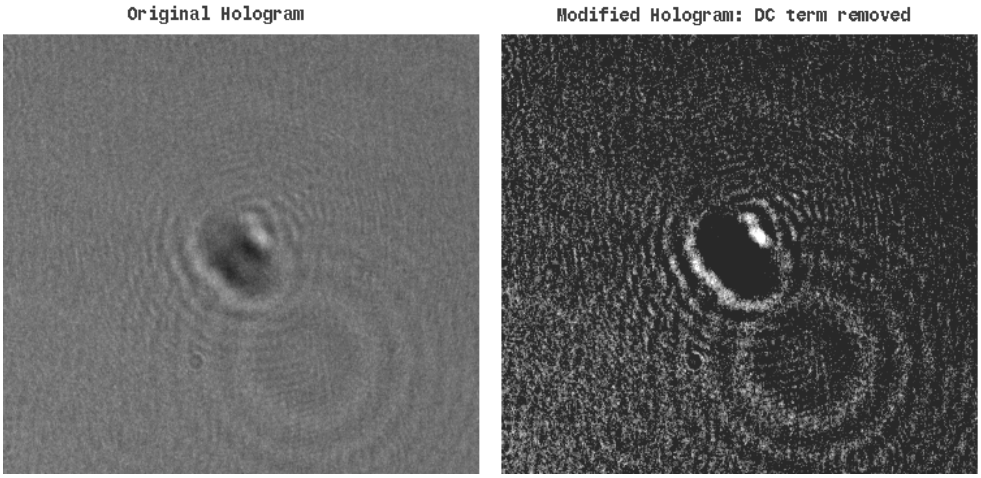

Figure 5-30: To the left: original hologram of a copepod. To the right: modified hologram with the DC term removed from equation 5.6.

The algorithm discussed above is equivalent to a high-pass filter with a low cutoff frequency. Other algorithms based on high-pass filters can be implemented to suppress the DC term, such as the nine pixels average filter given by

$$\begin{aligned} \hat{I}(k,l) &= I(k,l) - \frac{1}{9}[I(k-1,l-1) + I(k-1,l) + I(k-1,l+1) \\ &\quad + I(k,l-1) + I(k,l) + I(k,l+1) + I(k+1,l-1) \\ &\quad + I(k+1,l) + I(k+1,l+1)], \end{aligned} \tag{5.8}$$

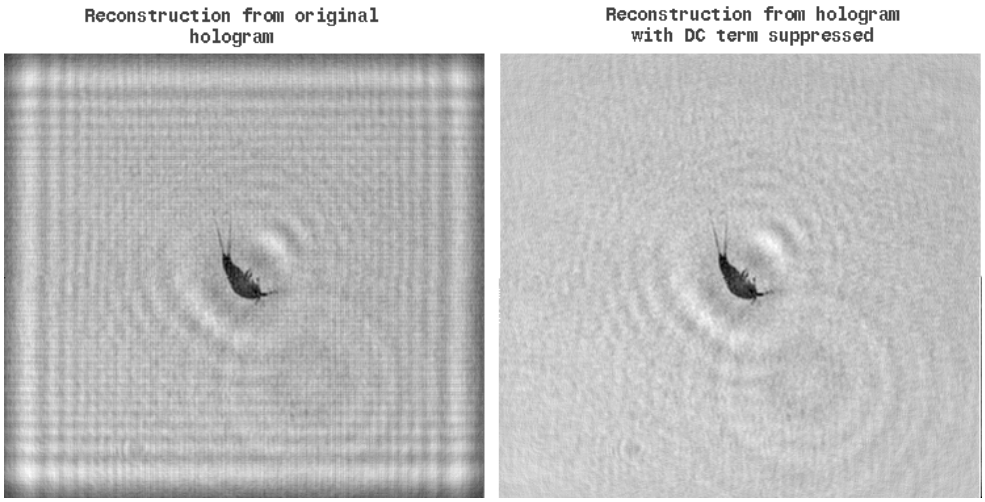

Figure 5-31: To the left: reconstruction from original hologram. To the right: reconstruction from hologram with DC term removed.

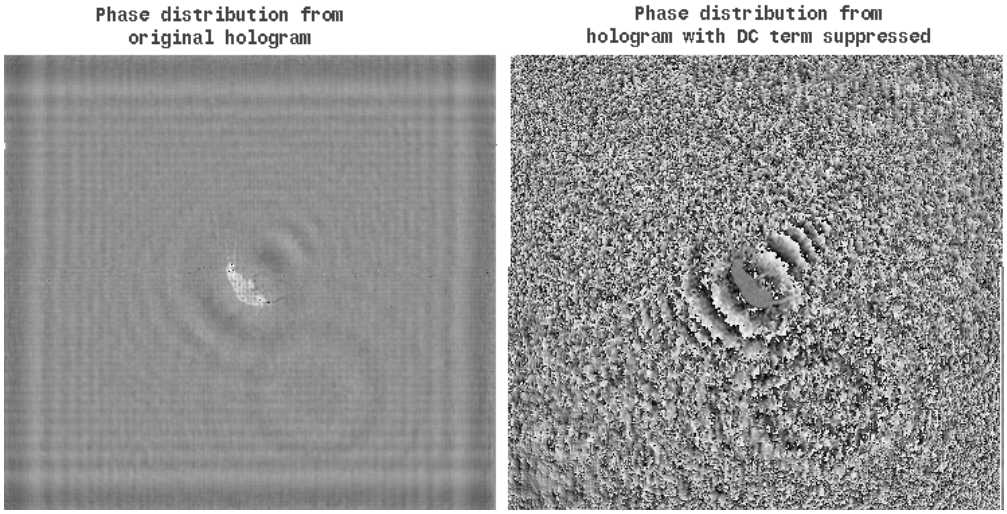

Figure 5-32: To the left: phase distribution of the field reconstructed from original hologram. To the right: phase distribution of the field reconstructed from hologram with DC term removed.

for

$$k = 1, ..., N-2, \quad \text{and} \quad l = 1, ..., M-2.$$

Figure 5-33 shows the modified hologram according to equation 5.8 and its corresponding reconstruction. In this figure, the edges of the reconstructed object are accentuated and the interior is suppressed as it maps to low frequencies in the spectrum. This also occurs for some of the background ripples that are filtered out in this algorithm.

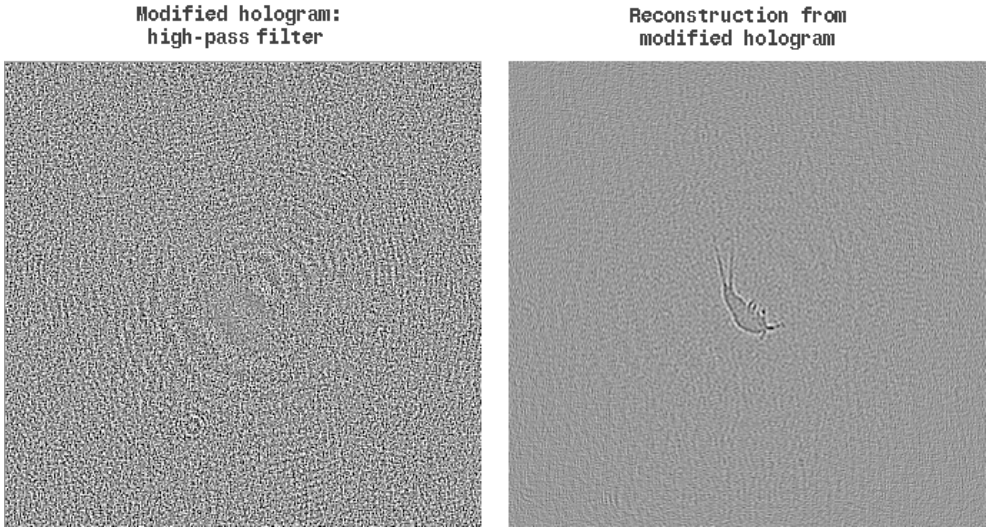

Figure 5-33: To the left: modified hologram obtained from equation 5.8. To the right: reconstruction from the modified hologram.

A similar result is obtained when the reconstruction is performed from the negative Laplacian of the original hologram as given by [146]:

$$\begin{aligned} \hat{I}(x,y) &= -\nabla^2 I(x,y) = -\left(\frac{\partial^2 I(x,y)}{\partial x} + \frac{\partial^2 I(x,y)}{\partial y}\right) \\ &\approx -\frac{1}{\Delta x \Delta y}[I(x+\Delta x, y) + I(x-\Delta x, y) \\ &\quad + I(x, y+\Delta y) + I(x, y-\Delta y) - 4I(x,y)]. \end{aligned} \tag{5.9}$$

Figure 5-34 shows the modified hologram according to equation 5.9 and its corresponding reconstruction. In the reconstruction shown in Figure 5-34, some sections of the contour of the object are lost reducing the quality of the image.

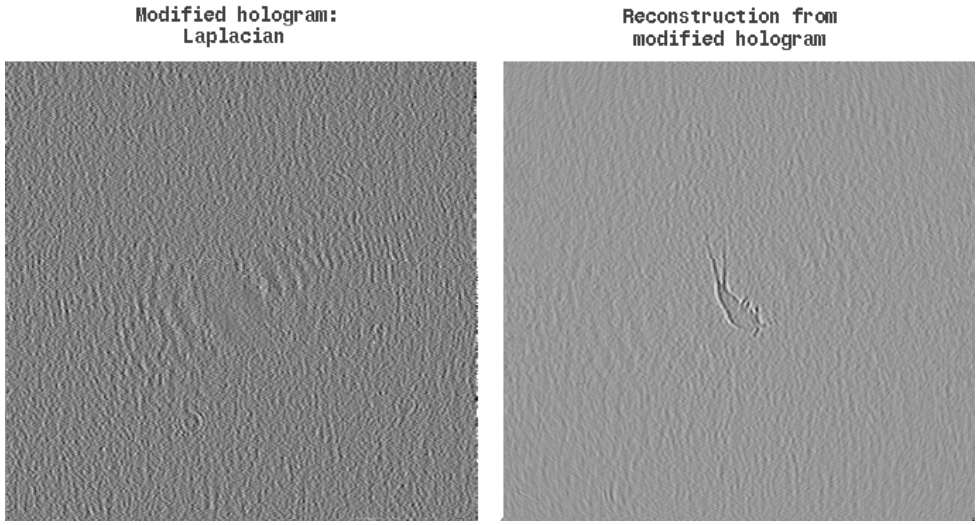

Figure 5-34: To the left: modified hologram obtained from equation 5.9. To the right: reconstruction from the modified hologram.

Another method for suppressing the DC term from the reconstructions involves using a band-pass filter in the spectrum of the hologram. This filter is extremely effective as it eliminates the low frequency spike in the spectrum, similar to equation 5.6, and some high-frequency noise that may be present in the hologram. The band-pass filter can be implemented directly in the Fourier domain by the pointwise multiplication of the spectrum and the filter matrices. The filter matrix contains a ring made of 1s that is surrounded by 0s. After multiplying the two matrices, all frequency components are blocked except for those that were located within the band-pass ring. The interior and exterior radii of the ring can be tuned according the requirements of the experiment. Figure 5-35 shows this filter implemented in the spectrum hologram of a copepod using different values for the interior and exterior radiuses of the band-pass ring.

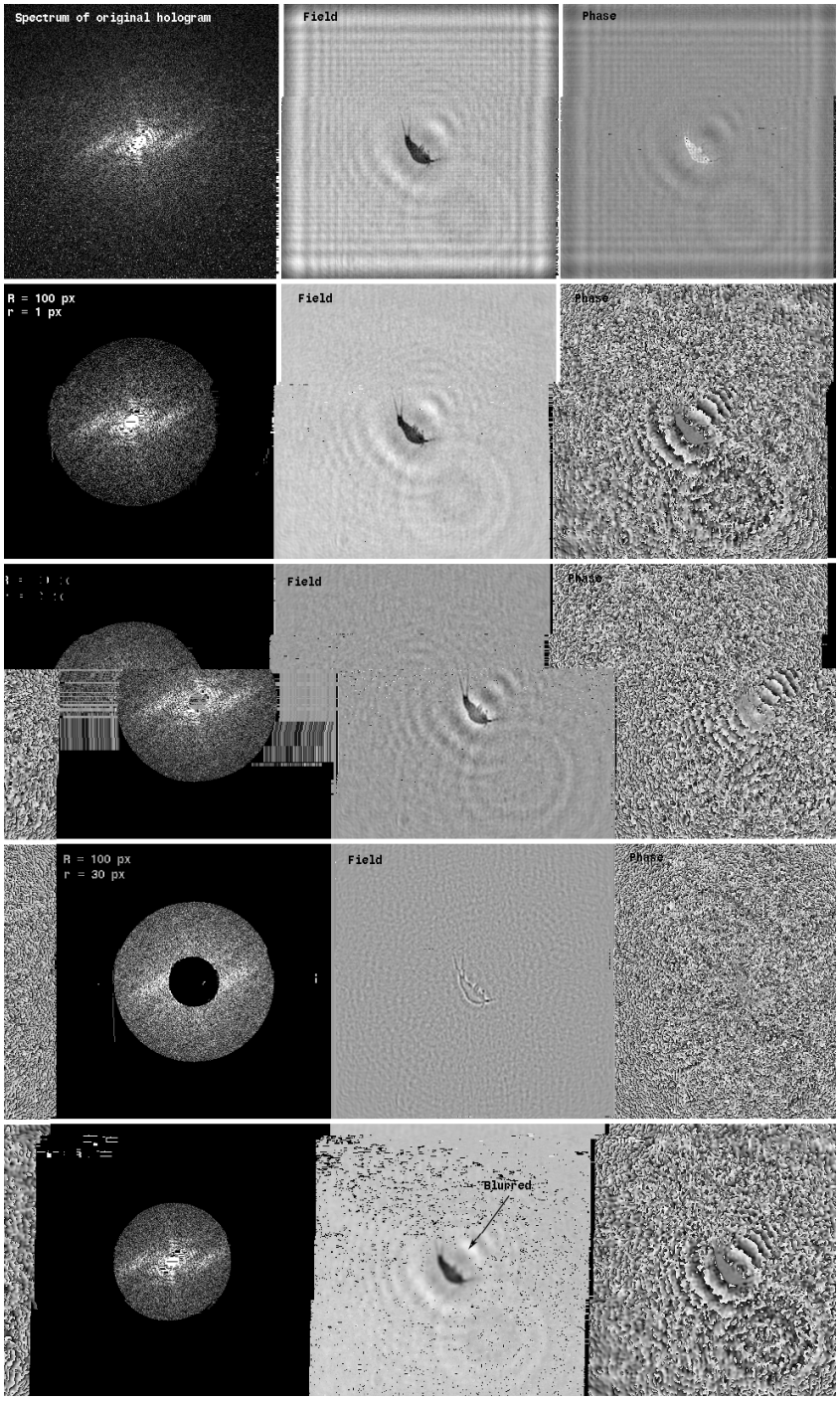

Figure 5-35: Band-pass filter algorithm used to remove the suppression of the DC term in the reconstructed images.

Chapter 6

Conclusions and Future Directions

Through an overview of the current technologies available to study plankton it became evident that further research and development is required to better understand aquatic ecosystems and their impact on the environment. This thesis explores the design and development of a DHI system for aquatic species starting by an analysis of conventional optical holographic systems and the mathematical formulation of the recording and the reconstruction of digital holograms. The implementation of digital holography is shown through the description of several recording set-ups that were later experimentally tested to determine the optimum configuration for underwater imaging applications. The resolution of the system is analyzed by considering the theoretical resolution limit in relation to the sampling requirements of the system. An experimental measurement of the resolution is presented for an in-line configuration with both planar and spherical reference waves. Criteria for designing an in-line holographic configuration for aquatic species was analyzed taking into consideration optical aberrations produced by imaging underwater objects, power analysis to determine the illumination source, detector selection and the implications of the motion of the object. This imaging system is tested on brine shrimp and copepods cultured in a laboratory. Several image post-processing algorithms are developed to enhance and analyze the reconstructed images, such as the DC term suppression, the reconstruction of binary holograms and the image analysis algorithms.

The numerical reconstruction is optimized by the development of an auto-scan algorithm that automatically determines the in-focus image from a reconstructed hologram and an algorithm designed to reconstruct large holograms in Matlab.

From the results uncovered during the design, development and implementation stages, it is found that digital holographic imaging is a promising technology that successfully enables the characterization of aquatic species with the final in-line single-beam experimental set-up providing the optimum configuration. This set-up maximizes the fringe spacing produced at the hologram plane permitting large volumes to be mapped to obtain biomass information from a certain aquatic organism. The images reconstructed for brine shrimp and copepods depict their minute features which enables taxonomical classification. Additional information, such as the life stage and behavior of these aquatic species can also be determined as the system operates in a non-intrusive mode by illuminating the sample with a low-powered light at a wavelength where plankton have shown to have a low response. The developed system has small dimensions and is extremely robust, as no moving parts are included. In addition, it tolerates external vibrations and large object motion due to the short integration time used to record each hologram. The quality of the reconstructed image is very high and not only allows a morphological classification of the aquatic species, but also permits an estimation of its 3D location. Undesired effects produced by the virtual image that can occur during reconstruction are minimal when imaging small, sparse objects such as plankton. In addition, artifacts introduced by the DC term in the reconstructed image can be effectively removed through DC term suppression algorithms. Experimental set-ups with a spherical reference wave achieve a resolution similar to conventional optical microscopy at larger working distances without using any magnifying lenses.

Despite the findings discussed above, possibilities exist to further improve this characterization including developing a submersible device capable of conducting in situ exploration based on components described in this thesis. The fabrication of such a device

would need to be water tight and capable of resisting high pressures without damaging the optical and electrical components. In addition, an alternative computational engine such as a digital signal processing (DSP) board could be included to increase the reconstruction speed.

Through additional improvements, there exists the possibility of instantaneously reconstructing a hologram and locating the 3D spatial location of the aquatic object which is sent to another imaging technology, such as volume holographic imaging (VHI), [70],for further characterization. Additional image post-processing algorithms could be integrated to enhance the quality of the reconstructions or recent developments in digital holography, such as the single-exposure phase shifting techniques [77], [147], [78], to completely remove the virtual image and the DC term from the reconstruction.

Bibliography

[1] J. S. Jaffe, "Sensing Plankton: Acoustics and Optical Imaging," (book chapter), *!"#$%&'( ) $#*+,$% $(- '#./"0 102'0 30$$.+*, (to appear) 2005.

[2] J. T. Turner, G. J. Doucette, C. L. Powell, D. M. Kulis, B. A. Keafer, D. M. Anderson, "Accumulation of red tide toxins in larger size fractions of zooplankton assemblages from Massachusetts Bay," *4'#5(& !6$0$27 8#$2#&++ 9&#5&+ :;<*, 2000.

[3] E. J. Buskey, H. Deyoe, F. J. Jochem, T. A. Villareal, "Effects of mesozooplankton removal an ammonium addition on planktonic trophic structure during a bloom of the Texas 'brown tide': a mesocosm study," *=> 80'(*?$(@&+&'#6,*, 25(2), 2003.

[4] Internet access: KC-Denmark, http://www.kc denmark.dk/public_html/p26.htm, 06/23/2005.

[5] Internet access: C.E. Lee, http://life.bio.sunysb.edu/marinebio/plankton.html, 06/23/2005.

[6] G. Griffiths, S. Fielding, H. S. J. Roe, "Biological-physical-acoustical Interactions," *A,& 9&'B C,'%?&# DDB =$,( ) 50&7 E 9$(+*, New York, 2002.

[7] K. F. Foote, T. K. Stanton, "Acoustical Methods," In R. P. Harris, P. H. Wiebe, J. Lenz, H. R. Skjodal, & M. Huntley (Eds.), *FC!9 G$$%0'(*?$(4&?,$H$0$27 4'("'0*, London: Academic Press, 2000.

[8] D. N. MacLennan, E. J. Simmonds, "Fisheries Acoustics," *C,'%.'(E -'00B I5+, '(H I5+,&#5&+ 9&#5&+*, 1992.

[9] H. Medwin, C. S. Clay, "Fundamentals of Acoustical Oceanography," Boston, *16'J H&.56 8#&++*, 1998.

[10] R. J. Urick, "Principles of Underwater Sound," *46K#'LJ-500 3$$* C$.%'(7*, 1983.

[11] G. S. Kino, "Acoustic Waves, Devices, Imaging and Analog Signal Processing," *8#&(?56&J-'00 952('0 8#$6&++5(2 9&#5&+*, A. V. Oppenheim, Ed., 1987.

[12] P. H. Wiebe, T.K. Stanton, M.C. Benfield, D.G. Mountain, C.H. Greene, "High-frequency acoustic volume backscatter in the Georges Bank coastal region and its interpretation using scattering models," *F!!! =$"#('0 $/ M6&'(56 !(25(&&#5(2*, 22(3), 445-464, 1997.

[13] P.H. Wiebe, T.K. Stanton, C.H. Greene, M.C. Benfield, H.M. Sosik, T.C. Austin, J.D. Warren, T. Hammer, "BIOMAPER-II: An integrated instrument platform for coupled biological and physical measurements in coastal and oceanic regimes," *F!!! =$"#('0 $/ M6&'(56 !(25(&&#5(2*, 27(3), 2002.

[14] D.A. Demer, M.A. Soule, R.P. Hewitt, "A multiple-frequency method for potentially improving the accuracy and precision of in situ target strength measurements," *=> 16$"+> 9$6> 1.>*, 105(4), 1999.

[15] P.H. Wiebe, C.H. Greene, "The use of high-frequency acoustics in the study of zooplankton spatial and temporal patterns," *8#$6&&H5(2+ $/ ?,& NF8@ 97.%$+5".$(8$0'# 35$0$27*, 7, 1994.

[16] D.V. Holliday, R.E. Pieper, "Determination of zooplankton size and distribution with multifrequency acoustic technology," *=$"#('0 H" C$(+5&0O C$(+&50 F(?&#('J ?5$(' 8$"# 0P!Q%0'#'?5$(H& 0' 4&#*, 46, 1989.

[17] G. Griffiths, A.J.K. Harris, R. Mansfield, M.L. Somers, N.A. Crisp, H.S., J. Roe, B.V. Smith, "A multi frequency echo sounder for use within a towed undulating vehicle to study oceanic zooplankton abundance," *F(8#$6&&H5(2+ $/ ?,& R?, F(J ?&#('?5$('0 C$(/&#&(6& $(!0&6?#$(56 !(25(&&#5(2 5(M6&'($2#'%,7*, Southampton, Hampshire, England, Institution of Electrical Engineers, London, 1997.

[18] K.G. Foote, "Broadband acoustic scattering signatures of fish and zooplankton (BASS)," *8#$6&&H5(2+ $/ ?,& <#H !"#$%&'(4 '#5(& 965&(6& '(H A&6,($0$27 C$(/&#J &(6&*, Lisbon, May 23-27, 1998.

[19] J.S. Jaffe, E. Reuss, D. Mcgehee, G. Chandran, "FTV- A sonar for tracking macro-zooplankton in three dimensions," *S&&%J9&' @&+&'#6, 8'#? FJM6&'($2#'%,56 @&J +&'#6, 8'%&#+*, 42(8), 1995.

[20] C.N. Flagg, S.L. Smith, "On the use of the Acoustic Doppler current profiler to measure zooplankton abundance," *S&&% 9&' @&+>*, 36, 1989.

[21] Internet access: U.S. Geological Survey, http://ms.water.usgs.gov/NWMD/adcp.html, 06/23/2005.

[22] J.E. Ehrenberg, "A Comparative Analysis of In Situ Methods for Directly Measuring the Acoustic Target Strength of Individual Fish," *F! ! ! => $/ M6&'(56 !(25J (&&#5(2*, Vol. OE-4, No. 4, 1979.

[23] D.V. Holliday, P.L. Donaghay, C.F. Greenlaw, D.E. McGehee, M.M. McManus, J.M. Sullivan, J.L. Miksis, "Advances in Defining Fine- and Micro-scale Pattern in Marine Plankton," *FC!9*, 2003.

[24] P.H. Wiebe, M.C. Benfield, "From the Hensen net toward four-dimensional biological oceanography," *8#$2#&++ 5(M6&'($2#'%,7*, 56 (1), 2003.

[25] Internet access: http://zooplankton.lsu.edu/survey_system.htm, 06/24/2005.

[26] D.Z. Chu, T.K. Stanton, "Application of pulse compression techniques to broadband acoustic scattering by live individual zooplankton," => 16$"+> 9$6> 1 . , 104(1), 1998.

[27] Internet access: Scientific Fisheries Systems Inc., http://www.scifish.com/, 06/24/2005.

[28] C.S. Davis, S.M. Gallager, AR. Solow, "Microaggregations of Oceanic Plankton Observed by Towed Video Microscopy," 965&(6& 257, 1992.

[29] C.S. Davis, S.M. Gallager, M.S. Berman, L.R. Houry, J.R. Strickler, "The Video Plankton Recorder (VPR): Design and initial results," 1#6,> -7H#$T5$0> 3&5,>, 36, 67-81, 1992.

[30] X.O. Tang, W.K. Stewart, L. Vincent, H. Huang, M. Marra, S.M. Gallager, C.S. Davis, "Automatic plankton image recognition," 1#?5U65'0 F(?&0052&(6& @&V5&L, 12(1-3), 1998.

[31] C.S. Davis, S.M. Gallager, M. Marra, W.K. Stewart, "Rapid visualization of plankton abundance and taxonomic composition using the video plankton recorder," S&&%J9&' @&+&'#6, 8'#? FFJA$%56'0 9?"H5&+ 5(M6&'($2#'%,7, 43, 7-8, 1996.

[32] G. Gorsky, C. Aldorf, M. Kage, M. Picheral, Y. Garcia, J. Favole, "Vertical distribution of suspended aggregates determined by a new underwater video profiler," 1(('0&+ H& 0 F(+?5?"? M6&'($2#'%,5W"&, 68, 1-2, 1992.

[33] T. Baussant, B. Gasser, G. Gorsky, A. Kantidakis, "Mesopelagic micronekton and macrozooplankton observed by echosounding, multiple-net sampling and video profiling across the Almeria-oran front (W. Mediterranean sea)," 1(('0&+ H& 0 F(+?5?"? M6&'($2#'%,5W"&, 69(1), 1993.

[34] G. Gorsky, M. Picheral, L. Stemmann, "Use of the Underwater Video Profiler for the study of aggregate dynamics in the North Mediterranean," *!+?"'#5(& C$'+?'0 E 9,&0/ 965&(6&*, 50(1), 2000.

[35] G. Gorsky, L. Prieur, I Taupier-Letage, L. Stemmann, M. Picheral, "Large particulate matter in the Western Mediterranean I. LPM distribution related to mesoscale hydrodynamics," *=$"#('0 $/ 4'#5(& 97+?&.+*, 33, 2002.

[36] Internet access: Census of Marine Life, http://www.coml.org/edu/tech/count/unvidpro.htm, 06/24/2005.

[37] M.C. Benfield, C.J. Schwehm, S.F. Keenan, "ZOOVIS: a high resolution digital camera system for quantifying zooplankton abundance and environmental data," *1.&#56'(9$65&?7 $/ X5.($0$27 '(H M6&'($2#'%,7B 1W"'?56 965&(6&+ 4&&?5(2*, Alburquerque, NM, February, 12-17, 2001.

[38] Internet access: http://zooplankton.lsu.edu/vector2002_web/zoovis2002.htm, 06/24/2005.

[39] J.R. Strickler, J.S. Hwang, "Matched Spatial Filters in Long Working Distance Microscopy of Phase Objects," In: Cheng, P.C., Hwang, P.P., Wu, J.L., Wang, G. and Kim H. [Eds.], *I$6"+$(4$H&#(456#$+6$%7>)$#0H 965&(?5U6 8"T05+,5(2 F(6.*, River Edge, N.J., 2000.

[40] A.W. Palowitch, J.S. Jaffe, "Three-dimensional ocean chlorophyll distributions from underwater serial-sectioned fluorescence images," *1%%05&H M%?56+*, 33(14), 1993.

[41] A.W. Palowitch, J.S. Jaffe, "Optical Serial Sectioned Chlorophyl-a Microstructure," *=>$/ K&$%,7+56'0 @&+&'#6,*, 10

[43] J.D. Warren, T.K. Stanton, M.C. Benfield, P.H. Wiebe, D. Chu, M. Sutor, "In situ measurements of acoustic targets strengths of gas-bearing siphonophores," *FC!9 =$"#('0 $/ 4'#5(& 965&(6&*, 58 (4), 2001.

[44] J.S. Jaffe, M.D. Ohman, A. De Robertis, "OASIS in the sea: measurement of the acoustic reflectivity of zooplankton with concurrent optical imaging," *S&&%J9&' @&+&'#6, 8'#? FFJA$%56'0 9?"H5&+ 5(M6&'($2#'%,7*, 45 (7), 1998.

[45] D. Gabor, "A New Microscopic Principle," *N'?"#&*, 161, 777-778, 1948.

[46] D. Gabor, "Microscopy by reconstructed wavefronts," *8#$6> @$7> 9$6> 1*,197, 454-487, 1949.

[47] D. Gabor, "Microscopy by reconstructed wavefronts: II," *8#$6> 8,7+> 9$6.*, B378, 449-468, 1951.

[48] D. Gabor, W.P. Goss, "Interference microscope with total wavefront reconstruction," *=> M%?> 1 .>*, 56-849, 1966.

[49] K. Creath, "Phase-shifting holographic Interferometry," *F(Y -$0$2#'%,56 F(?&#/&#J $.&?#7B 9%5(2&# 9&#5&+ 5(M%?56'0 965&(6&+*, 68, 109-150, 1994.

[50] E.N. Leith, J. Upatnieks, "Reconstructed wavefronts and communication theory," *=> M%?> 9$6> 1 .>*, 52, 1123-1130, 1962.

[51] E.N. Leith, J. Upatnieks, "Wavefront reconstruction with diffused illumination and threedimensional objects," *=> M%?> 1 .>*, 54, 1295-1301,1964.

[52] J.W. Goodman, "Introduction to Fourier Optics," *46K#'LJ-500B N&L Z$#*B +&6$(H &H5?5$(*, 1996.

[53] Y.N. Denisyuk, "Photographic reconstruction of the optical properties of an object in its own scattered radiation field," *9$V> 8,7+>J S$*0>*, 7-543, 1962.

[54] R.L. Powell, K.A. Stetson, "Interferometric Vibration Analysis by Wavefront reconstructions," => M%?> 9$6> 1 . >, 55, 1593-1598, 1965.

[55] K.A. Stetson, R.L. Powell, "Interferometric hologram evaluation and real-time vibration analysis of diffuse objects," => M%?> 9$6> 1 . >, 55, 1694-1695, 1965.

[56] W.H. Lee, "Computer-generated Holograms: Techniques and Applications," 8#$2#&++ 5(M%?56+, 16, 120-232, 1978.

[57] O. Bryngdahl, F. Wyrowsky, "Digital Holography – computer generated holograms," 8#$2#&++ 5(M%?56+B 28, 1-86, 1990.

[58] D. Schreier, "Synthetische Holografie," [C-B)&5(,&5. , 1984.

[59] J.W. Goodman, R.W. Lawrence, "Digital image formation from electronically detected holograms," 1%%0> 8,7+> X&??>, 11, 77-79, 1967.

[60] M.A. Kronrod, N.S. Merzlyakov, L.P. Yaroslavski, "Reconstruction of holograms with a computer," 9$V> 8,7+JA&6, 8,7+, 17(2), 333-334, 1972.

[61] L. Onural, P.D. Scott, "Digital decoding of in-line holograms," M%?> !(2>, 26, 1124-1132, 1987.

[62] G. Liu, P.D. Scott, "Phase retrieval and twin-image elimination for in-line Fresnel holograms," => M%?> 9$6> 1 . > 1, 4(1), 159-165, 1987.

[63] L. Onural, M.T. Özgen, "Extraction of three-dimensional object-location information directly from in-line holograms using Wigner analysis," => M%?> 9$6> 1 . > 1, 9(2), 252-260, 1992.

[64] L. Onural, "Digital Decoding of In-line Holograms," S$6?$#'0P+ ?,&+5+B 9?'?& \(5J V&#+5?7 $/ N&L Z$#* '? 3"]'0$B 1985.

[65] McCrickerd, N. George, "Holographic stereogram from sequential component photographs," 1%%0> 8,7+> X&??>, 12, 10-12, 1968.

[66] D.J. De Bitteto, "Holographic panoramic stereograms synthesized from white light recordings," *1%%0> M%?>*, 8, 1740-1741, 1970.

[67] S.A. Benton, "On a method for reducing the information content of holograms," => *M%?> 9$6> 1 . .*, 59, 1545, 1969.

[68] L. Cross, "Multiplex holography," *8#&+&(?&H '? ?,& 9>8>F>!> 9&.5('# $(A,#&& S5.&(+5$('0 F.'25(2B T"? "(%"T05+,&H*, August 1977.

[69] G. Saxby, "Practical Holography," *8#&(?56&J-'00*, Englewood Cliffs, Nj, 1988.

[70] G. Barbastathis, D.J. Brady, "Multidimensional tomographic imaging using volume holography," *8#$6> F!!!>*, 87(12), 2098-2120, 1999.

[71] W.Li, "Computational Reconstruction of Images From Optical Holograms," *4'+J ?&#P+ ?,&+5+*, Department of Ocean Engineering and Department of Electrical Engineering and Computer Science, Massachusetts Institute of Technology, Cambridge, MA, 2002.

[72] D.R. Kitchin, "Astrophysical Techniques," (4rd edition), *F(+?5?"?& $/ 8,7+56+*, 2003.

[73] J.H. Milgram, W. Li, "Computational reconstruction of images from holograms," *1%%0> M%?>*, 41(5), 853-864, 2002.

[74] P. Hariharan, "Optical Holography: Principles, Techniques, and Applications," *C'.T#5H2& \> 8#&++B C'.T#5H2&B !(20'(H*, 1996.

[75] I. Yamaguchi, T. Zhang, "Phase-shifting digital holography," *M%?> X&??.*, 22(16), 1268-1270, 1997.

[76] L. Songcan, B. King, M.A. Neifeld, "Wavefront reconstruction by means of phase-shifting digital in-line holography", *M%?> C$. .>*, 173, 155-160, 2000.

[77] Y. Awatsuji, A. Fujii, T. Onchi, T. Kubota, O. Matoba, "Parallel three-step-phase-shifting digital holography," *A,& U#+? M91 A$%56'0 . &&?5(2 $(F(/$#. '?5$(8,$J ?$(56+ ^F8:;;_`B =) 3a*, Charlotte, U.S.A., 2005.

[78] B. Javidi, D. Kim, "Three-dimensional-object recognition by use of single-exposure on-axis digital holography," *M%?> X&??>*, 30(3), 236-238, 2005.

[79] M.V. Klein, T.E. Furtak, "Optics," *:(H &H) 50&7B N&L Z$#*B* 1986.

[80] U. Schnars, W. Jüptner, "Direct recording of holograms by a CCD target and numerical reconstruction," *1%%> M%?>B* 33(2), 179-181, 1994.

[81] U. Schnars, "Direct phase determination in hologram interferometry with use of digitally recorded holograms," *=> M%?> 9$6> 1 .> 1*, 11(7), 2011-2015, 1997.

[82] W. Haddad, D. Cullen, J. Solem, J. Longworth, A. McPherson, K. Boyer, K. Rhodes, "Fourier-transform holographic microscope," *1%%0> M%?>*, 31(24), 4973-4978, 1992.

[83] H.J. Kreuzer, R.A. Pawlitzek, "Numerical Reconstruction for in-line Holography in Reflection and under Glancing Incidence," *F(Y =b%?(&#)> M+?&( ) ^&H+` 8#$6 <#H F(?&#('?5$('0) $#*+,$% $(1"?$. '?56 8#$6&++5(2 $/ I#5(2& 8'??&#(+B* Akademie, Berlin, 364-367,1997.

[84] V. Kebbel, H.J. Hartmann, W. Jüptner, "Application of digital holographic microscopy for inspection of micro-optical components," *F(Y 8#$6 98F!*, 4398, 189-198, 2001.

[85] E. Cuche, P. Marquet, C. Depeursinge, "Simultaneous amplitude-contrast and quantitative phase-contrast microscopy by numerical reconstruction of Fresnel off-axis holograms," *1%%> M%?>*, 38(34), 6994-7001, 1999.

[86] U. Schnars, "Digitale Aufzeichnung und mathematishe Rekonstruktion von Hologrammen in der Interferometrie," *[SFJI$#?+,#5??J3&#56,?& +&#5&+*, 8(378), VDI, Düsseldorf, 1994.

[87] U. Schnars, W. Jueptner, "Digital Holography," *9%#5(2&#B K&#. '(7*, 2005.

[88] T.H. Demetrakopoulos, R. Mittra, "Digital and optical reconstruction of images from suboptical diffraction patterns," *1%%0> M%?>*, 13(3), 665-670, 1974.

[89] T. Kreis, Jüptner W., "Principles of digital holography," *F(Y =b%?(&#) B M+?&( ) ^&H+` 8#$6 <#H F(?&#('?5$('0) $#*+,$% $(1"?$. '?56 8#$6&++5(2 $/ I#5(2& 8'??&#(+*, Akademie, Berlin, 353-363, 1997.

[90] T.M. Kreis, "Frequency analysis of digital holography," *M%?> !(2>B* 41(4), 771-778, 2002.

[91] L. Xu, J. Miao, A. Asundi, "Properties of digital holography based on in-line configuration," *M%?> !(2>*, 39(12), 3214-3219, 2000.

[92] C. Knox, "Holographic microscopy as a technique for recording dynamic microscopic subjects," *965&(6&*, 153, 989-990, 1966.

[93] C. Knox, R.E. Brooks, *8#$6> @> 9$6> 3*, 174, 115, 1969.

[94] G.L. Stewart, J.R. Beers, C. Knox, "Application of holographic techniques to the study of marine plankton in the field and in the laboratory," *S&V&0$%.&(?+ 5(X'+&# A&6,($0$27JFFB 8#$6> 9$6> 8,$?$JM%?> F(+?#".> !(2> ^9'(S5&2$B C1`*, 41, 193, 1973.

[95] L.O. Heflinger, G.L. Stewart, C.R. Booth, "Holographic motion pictures of microscopic plankton," *1%%0> M%?>*, 17, 951-954, 1978.

[96] K.L. Carder, "Holographic microvelocimeter for use in studying ocean particle dynamics," *M%?56'0 !(25(&&#5(2*, 18, 1979.

[97] K.L. Carder, R.G. Steward, P.R. Betzer, "In situ holographic measurements of the sizes and settling of oceanic particulates," => K&$%,7+> @&+>B 87, 5681-5685, 1982.

[98] T.J. O'Hern, L. D'Agostino, A.J. Acosta, "Comparison of holographic and Coulter counter measurements of cavitation nuclei in the ocean," => I0"5H+ !(2>, 110, 200-207, 1988.

[99] J. Katz, T.J. O'Hern, A.J. Acosta, "An underwater holographic camera system for detection of microparticulates," 8#$6> 194! C'V5?'?5$('(H 4"0?5%,'+& I0$L I$#". ^N&L M#0&'(+B X1`, 1984.

[100] J. Katz, P.L. Donaghay, J. Zhang, S. King, K. Russell, "Submersible holocamera for detection of particle characteristics and motions in the ocean," S&&% 9&' @&+>B 1, 46, 1999.

[101] E. Malkiel, O. Alquaddoomi, J. Katz, "Measurements of plankton distribution in the ocean using submersible holography," 4&'+"#&.&(? 965&(6& E A&6,($0$27. 10(2), 1999.

[102] E. Malkiel, J.N. Abras, J. Katz, "Automated scanning and measurements of particle distributions within a holographic reconstructed volume," 4&'+> 965> A&6,($0>B 15 601-612, 2004.

[103] J. Watson, S. Alexander, V. Chalvidan, G. Craig, A. Diard, G.L. Foresti, S. Gentili, D.C. Hendry, P.R. Hobson, R.S. Lampitt, H. Nareid, J.J. Nebrensky, A. Pescetto, G.G. Pieroni, M.A. Player, K. Saw, S. Serpico, K. Tipping, A. Trucco, "A holographic system for subsea recording and analysis of plankton and other marine particles (HOLOMAR)," MC!1N9 :;;<> 8#$6&&H5(2+, 2, 22-26, 2003.

[104] J. Watson, S. Alexander, G. Craig, D.C. Hendry, P.R. Hobson, R.S. Lampitt, M.M. Marteau, H. Naried, M.A. Player, K. Saw, K. Tipping, "Simultaneous in-line and off-axis subsea holographic recording of plankton and other marine particles," 4&'+> 965> A&6,($0>, 12, 2001.

[105] G. Craig, H. Nareid, J. Watson, "Underwater holography in the field," *F! ! !B 9'V$7 80'6&B X$(H$( ) C:@ M3XB \ c>*, 10/1-10/4.

[106] Y. Pu, X. Song, H. Meng, "Holographic PIV for diagnosing particulate flows," *!Q%&#5 . &(?+ 5(I0"5H+B* 29(7), 117-128, 2000.

[107] G. Pan, H. Meng, "Digital In-line Holographic PIV for 3D Particulate Flow Diagnostics," *A,& I$"#?, F(?&#('?5$('0 97 . %$+5" . $(8'#?560& F . '2& [&0$65 . &?#7 ^8F[`B D;;d*, Göttingen, Germany, 17-19, 2001.

[108] J.J. Nebrensky, G. Craig, G.L. Foresti, S. Gentili, P.R. Hobson, H. Nareid, G.G. Pieroni, J. Watson, "A Particle Imaging and Analysis System for Underwater Holograms," *F(M%?56'0 4&?,$H+ '(H S'?' 8#$6&++5(2 5(-&'? '(H I0"5H I0$LB 4&6,! C$(/&#&(6& A#'(+'6?5$(+ ^DeedJ:` M%?56'0 4&?,$H+ '(H S'?' 8#$6&++5(2 5(-&'? '(H I0"5H I0$LB 8'%&# C_aDO;_f0ed*, London, 1998, 121-134.

[109] C.S. Vikram, "Particle Field Holography," *C' . T#5H2& \ (5V&#+5?7 8#&++*, 1992.

[110] E. Malkiel, J. Sheng, J. Katz , J. R. Strickle, "The three-dimensional flow field generated by a feeding calanoid copepod measured using digital holography," *A,& =$"#('0 $/ !Q%&#5 . &(?'0 35$0$27*, 206, 3657-3666, 2003.

[111] R.B. Owen, A.A. Zozulya, "In-line digital holographic sensor for monitoring and characterizing marine particulates," *M%?56'0 !(25(&&#5(2B* 39(8), 2000.

[112] X. Quan, E.S. Fry, "Empirical equation for the index of refraction of seawater," *1%%0> M%?>*, 34(18), 3477-3480, 1995.

[113] J.M. Kilpatrick, Watson J., "Underwater hologrammetry: aberrations in the real image of an underwater object when replayed in air," *1%%0> 8,7+>B* 21, 1701-1705, 1988.

[114] J.M. Kilpatrick, J. Watson, "Precision replay of underwater holograms," *4&'+> 965> A&6,($0>*, 5, 716-725, 1994.

[115] J.M. Kilpatrick, J. Watson, "Underwater hologrammetry: reduction of aberrations by index compensation," *1%%0> 8,7+*, 26, 177-182, 1993.

[116] H. Meng, W.L. Anderson, F. Hussain, D.D. Liu, "Intrinsic speckle noise in in-line particle holography," *=> M%?> 9$6> 1 . > 1*, 10(9), 2046-2058, 1993.

[117] Y. Pu, Y. Meng, "Intrinsic speckle noise in off-axis particle holography," *=> M%?> 9$6> 1 .>1*, 21(7), 2004.

[118] R.M. Pope, "Optical absorption of pure water and seawater using the integrating cavity absorption meter," *A&Q'+ 1E4 \(5V&#+5?7*, 1993.

[119] R.B. Forward, "Diel vertical migration: Zooplankton photobiology and behaviour," *M6&'($2#'%,7 '(H 4 '#5(& 35$0$27J 1(1(("'0 @&V5&L*, 26, 361-393, 1988.

[120] E.J. Buskey, K.S. Barker, R.C. Smith, E. Swift, "Photosensitivity of the oceanic copepods Pleuromamma gracilis and Pleuromamma xiphias and its relationship to light penetration and daytime depth distribution," *4 '#> !6$0> 8#$2> 9&#>*, 55, 207-216, 1989.

[121] J.H. Cohen, R.B. Forward, "Spectral Sensitivity of Vertically Migrating Marine Copepods," *35$0B 3"00>*, 203, 307-314, 2002.

[122] E.P. Zege, A.P. Ivanov, I.L. Katsev, "Image Transfer Through a Scattering Medium," *9%#5(2&# [&#0'2*, New York, 1991.

[123] T.J. Petzold, "Volume Scattering Function of Selected Ocean Waters," *96#5%%+ F(+?5?"?5$($/ M6&'($2#'%,7B X' =$00'B C1*, 1972.

[124] L.E. Mertens, F.S. Replogle Jr., "Use of Point Spread and Beam Spread Functions for Analysis of Imaging Systems in Water," *=>M%?> 9$6> 1 . >*, 67 (1), 1977.

[125] K.J. Voss, "Variation of the Point Spread Function in the Sargasso Sea," *98F!B* 1537, Underwater Imaging, Photography, and Visibility, 1991.

[126] K.J. Voss, "Simple Empirical Model of the Oceanic Point Spread Function," *1%%> M%?>*, 30, 18, 1991.

[127] J.W. McLean, K.J. Voss, "Point Spread Function in Ocean Water: Comparison Between Theory and Experiment," *1%%> M%?>*, 30(15), 1991.

[128] B.J. McGlamery, "A computer model for underwater camera systems," *M%?> !(2>*, 14(4), 1975.

[129] J.S. Jaffe, "Computer modeling and the design of optimal underwater Imaging Systems," *F!!!B => M6&'(56 !(2>*, 15(2), 1990.

[130] E. Hecht, "Optics," Fourth Edition, *8&'#+$(!H"6'?5$(*, 2002.

[131] S.J. Lim, "Two-Dimensional Signal and Image Processing," *8#&(?56& -'00B !(20&J L$$H C05]+*, New Jersey, 1990.

[132] S.L. Cartwright, P. Dunn, B.J. Thompson, "Particle sizing using far-field holography: new developments," *M%?> !(2>*, 19, 727-733, 1980.

[133] H. Jiang, T.R. Osborn, C. Meneveau, "Chemoreception and the deformation of the active space in freely swimming copepods: a numerical study," *=$"#('0 $/ 80'(*?$(@&+&'#6,*, 24(5), 495-510, 2002.

[134] Internet access: http://home.cogeco.ca/~rpaisley4/LM555.html, 06/02/2005.

[135] T.A. Williams, "A Model of Rowing Propulsion and the Ontogeny of Locomotion in Artemia Larvae," *35$0> 3"00>*, 187, 164-173, 1994.

[136] J. Gillespie, R.A. King, "The use of self-entropy as a focus measure in digital holography," *8'??&#(@&6$2(> X&??>*, 9, 19-25, 1989.

[137] P. Ferraro, G. Coppola, S. De Nicola, A. Finizio, G. Pierattini, "Digital holographic microscope with automatic focus tracking by detecting sample displacement in real time," *M%?> X&??>*, 28, 1257-1259, 2003.

[138] M. Liebling, M. Unser, "Autofocus for digital Fresnel holograms by use of a Fresnelet-sparsity criterion," => M%?> 9$6> 1 . > 1, 21(12), 2424-2430, 2004.

[139] A. Chavez, F. Mayinger, "Evaluation of pulsed laser holograms of spray droplets by applying digital image processing," 8#$6> e?, F(?> C$(/> $(-&'? A#'(+/&# &H K -&?+#$(5 ^=&#"+'0& . Y -& . 5+%,&#&`, 187-192, 1990.

[140] S.I. Green, Z.J. Zhao, "Reconstructed double-pulsed holograms – a system for efficient automated-analysis," 1%%0> M%?>, 33, 761-767, 1994.

[141] G. Haussmann, W. Lauterborn, "Determination of size and position of fast moving gas-bubbles in liquids by digital 3D image-processing of hologram reconstructions," 1%%0> M%?>, 19, 3529-3535, 1980.

[142] A.C. Stanton, H.J. Caulfield, G.W. Stewart, "An approach for automated-analysis of particle holograms," M%?> !(2>, 23, 577-582, 1984.

[143] J.H. Milgram, "Computational Holographic Image Reconstruction," 8#$6&&H5(2+ $/ 98F!, 4659(12), 2002.

[144] The Math Works, Inc., 3 Apple Hill Drive, Natick, MA 01760-2098. F. '2& 8#$6&++J 5(2 A$$0T$Q I$# \+& L5?, 4'?0'T, 2005.

[145] T.M. Kreis, W.P.O. Jüptner, "Suppression of the DC term in digital holography," M%?> !(2>, 36(8), 2357-2360, 1997.

[146] C. Liu, Y. Li, X. Cheng, Z. Liu, F. Bo, J. Zhu, "Elimination of zero-order diffraction in digital holography," M%?> !(2>, 41(10), 2434-2437, 2002.

[147] D. Kim, B. Javidi, "Distortion-tolerant 3-D object recognition by using single exposure on-axis digital holography," M%?56+ !Q%#&++, 12(22), 2004.

Appendix A

Reconstructions of Brine Shrimp

This appendix presents three reconstructions conducted for the experiments with brine shrimp. The holograms were recorded using the in-line single-beam configuration discussed in Chapter 4.

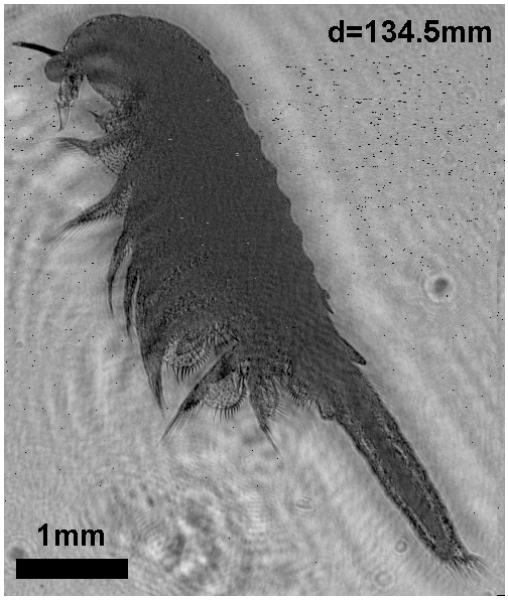

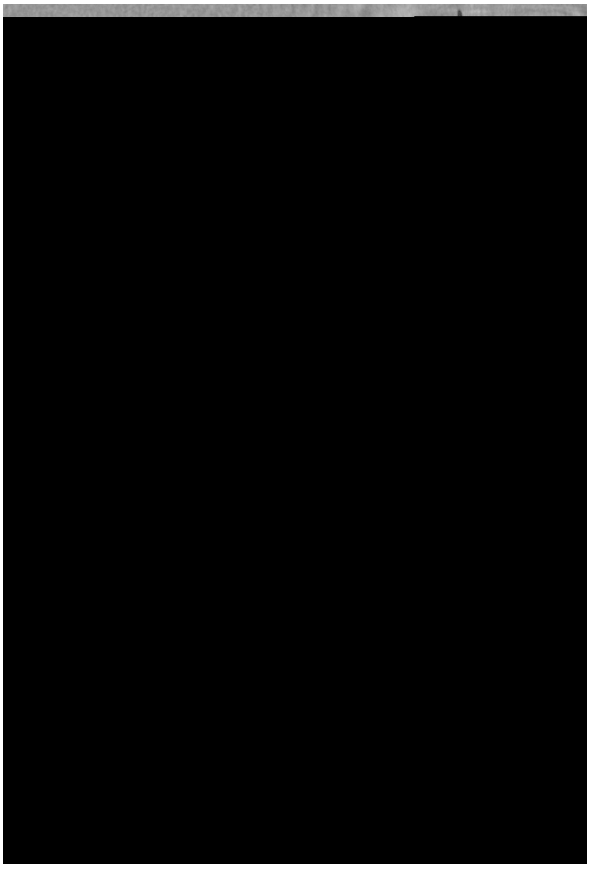

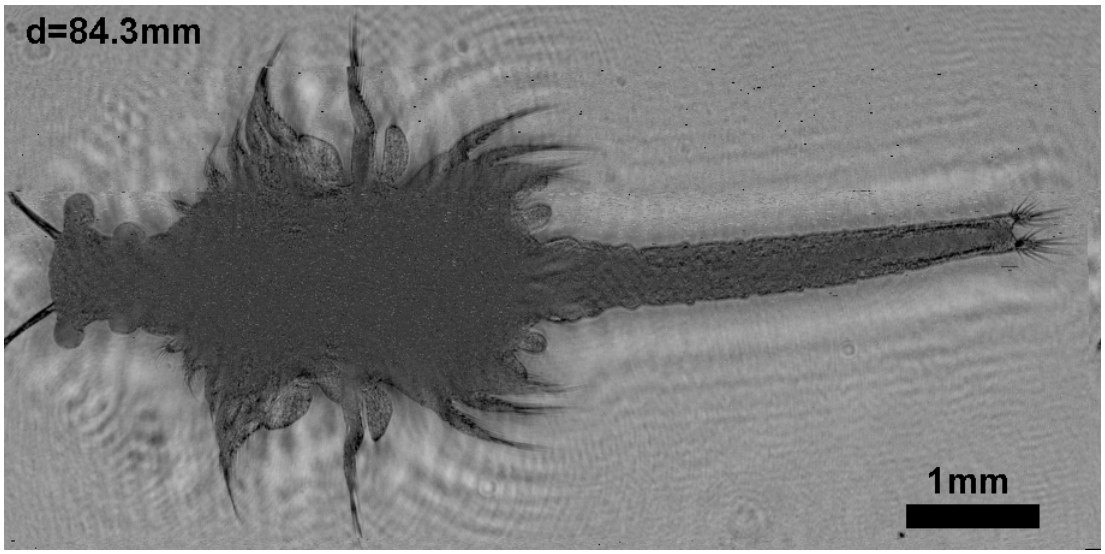
d=84.3mm
1mm

Appendix B

Reconstructions of Copepods

In this appendix, several reconstructions conducted for the experiments with copepods are presented. The holograms were recorded using the in-line single-beam configuration discussed in Chapter 4.

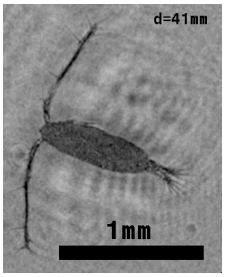

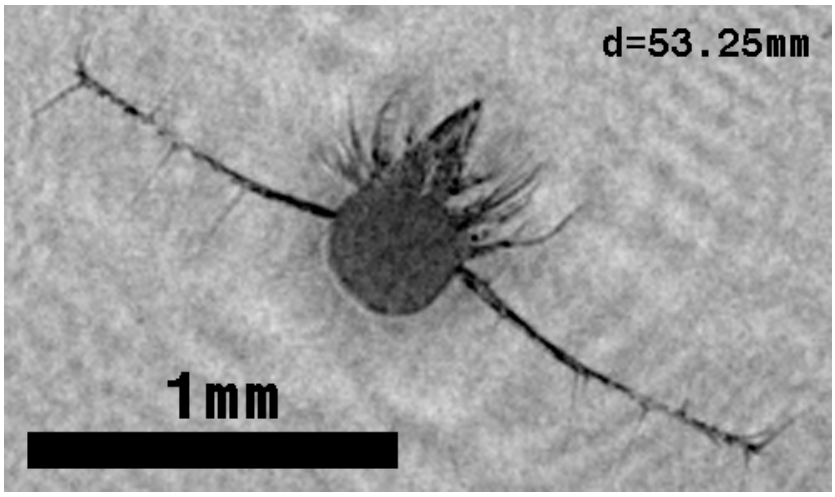
d=53.25mm
1mm

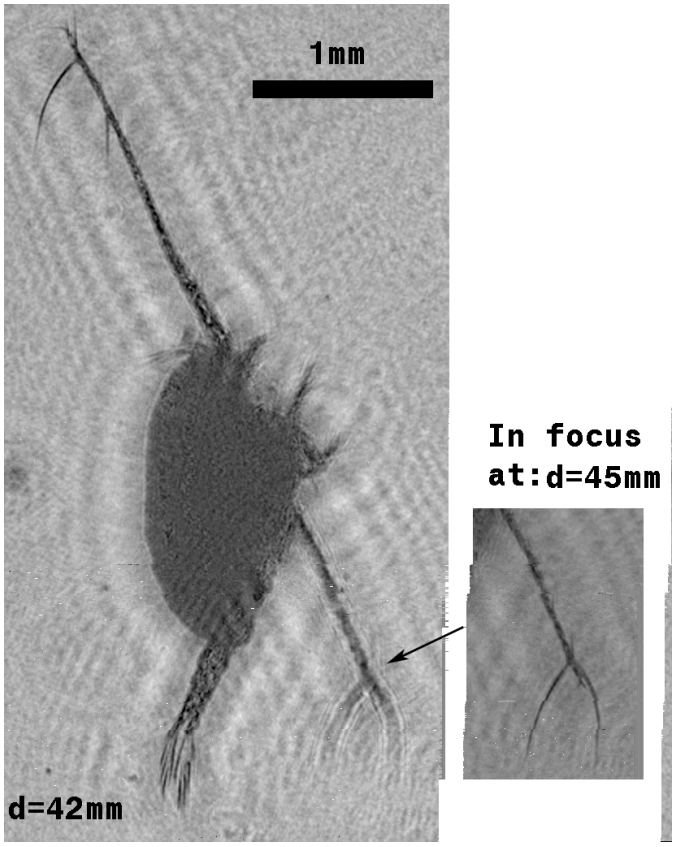
1mm
In focus
at:d=45mm
d=42mm

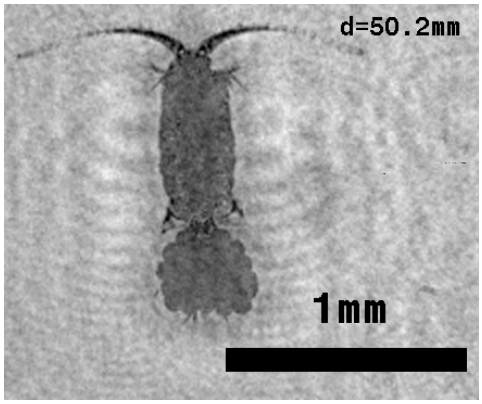
d=50.2mm
1mm

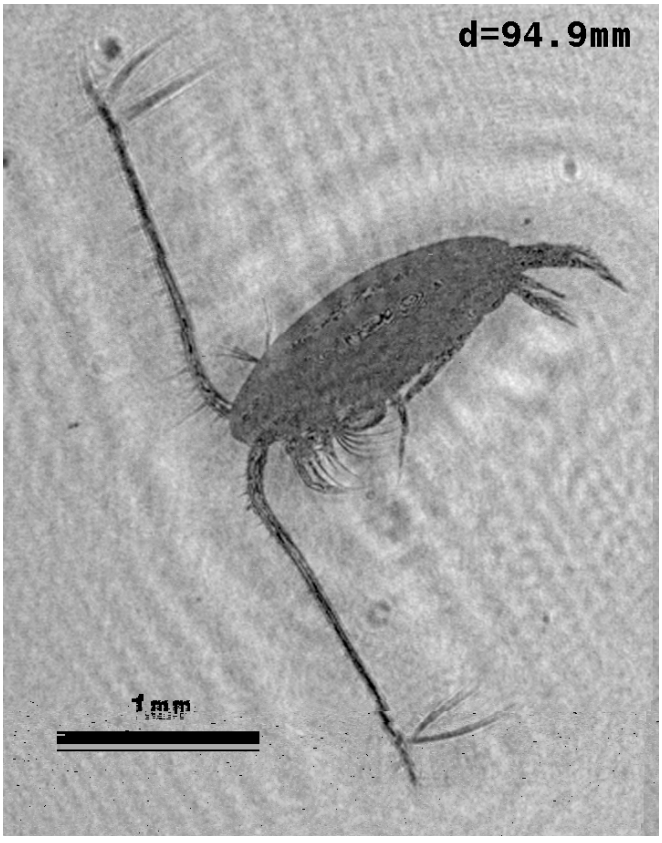
d=94.9mm
1mm

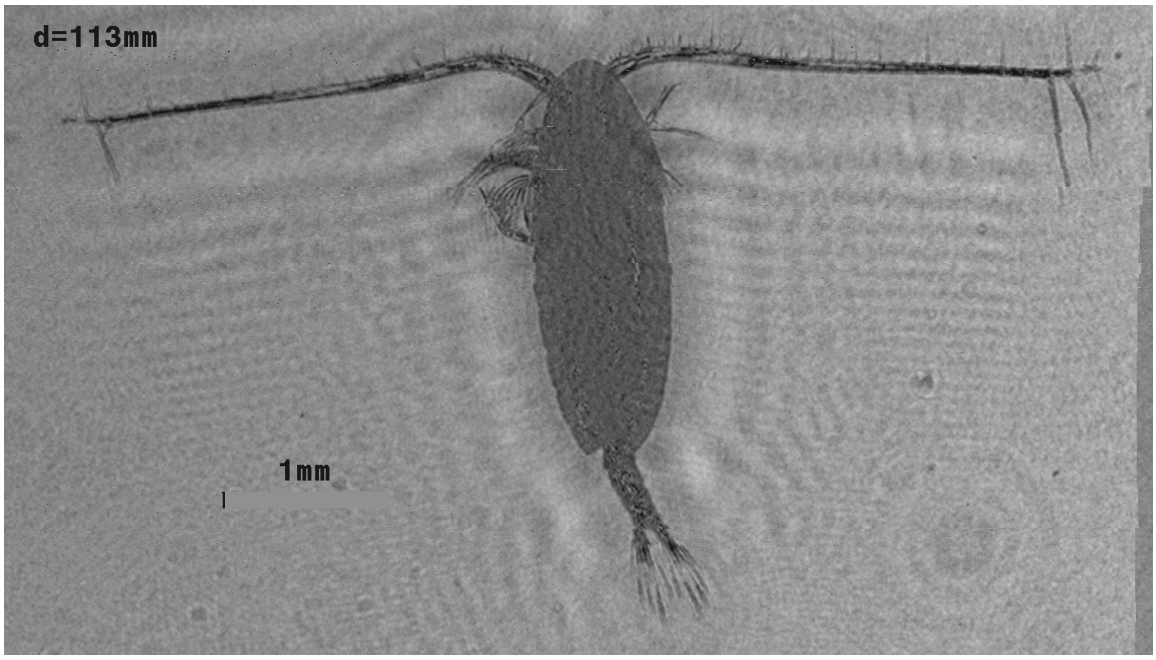
d=113mm
1mm

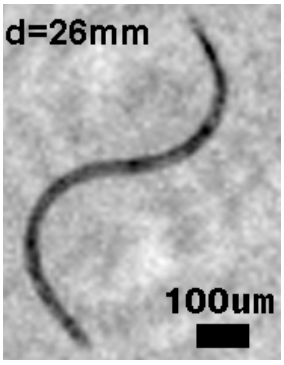
d=26mm
100um

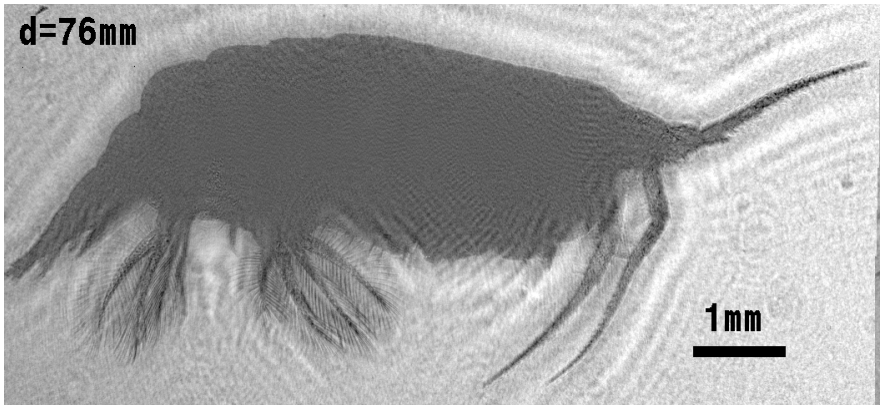
d=76mm
1mm

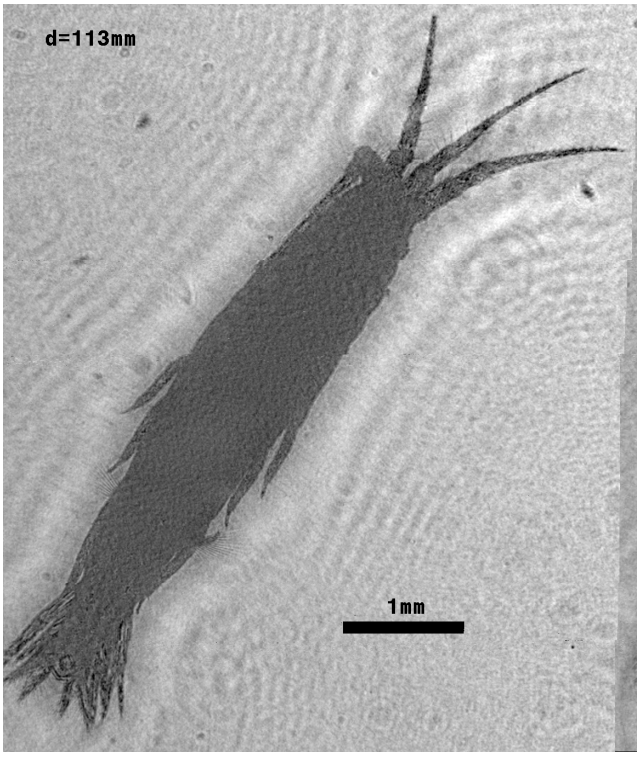
d=113mm
1mm

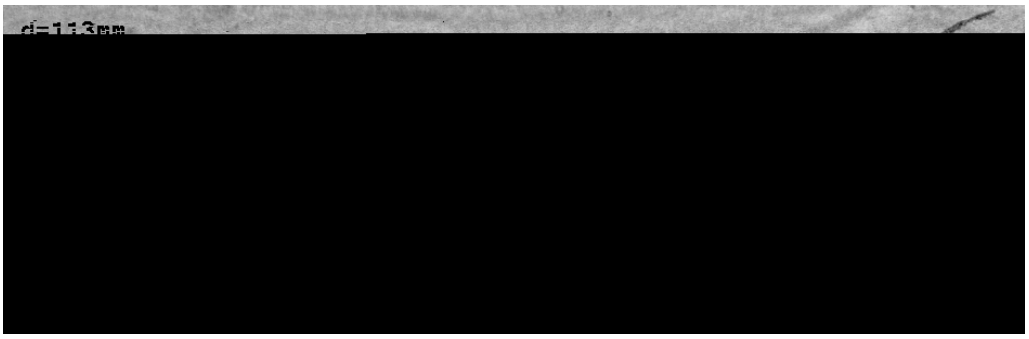

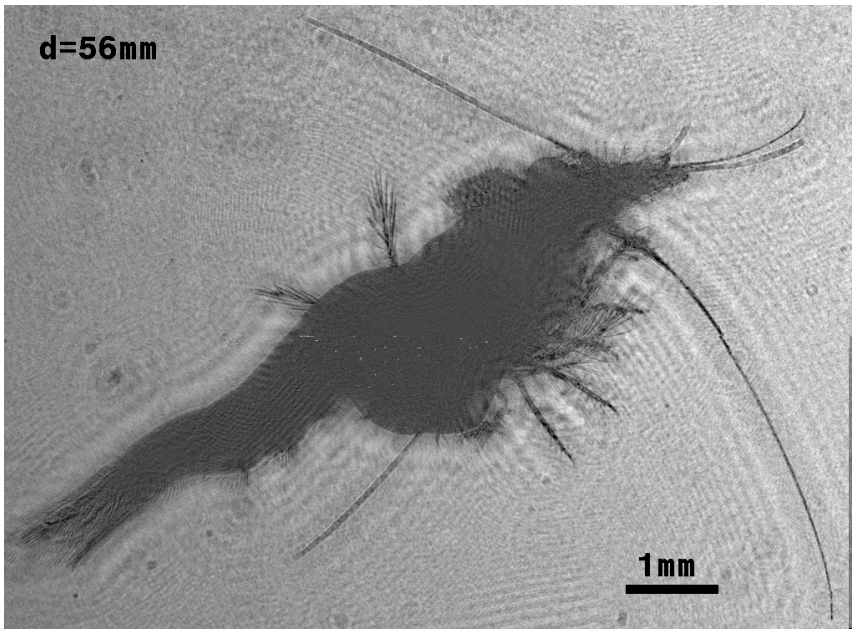
d=56mm
1mm